Few-cycle optical waveforms for transient molecular fingerprinting

Enrico Ridente

München 2021

Few-cycle optical waveforms for transient molecular fingerprinting

Enrico Ridente

Dissertation
an der Fakultät für Physik
der Ludwig–Maximilians–Universität
München

vorgelegt von
Enrico Ridente
aus Enna, Italien

München, den 31.05.2021

Erstgutachter: Prof. Dr. Ferenc Krausz
Zweitgutachter: Prof. Dr. Regina de Vivie-Riedle
Tag der mündlichen Prüfung: 20.07.2021

Contents

Abstract

The majority of the physical phenomena happening around us can be described in terms of energy-matter interaction. Photons can efficiently transfer energy to a system, thus enabling the investigation of matter under different energetic regimes. In the form of light pulses, photons can trigger ultrafast events on an illuminated target. Three essential components are required to induce and capture those events: a light source that can produce ultrashort pulses, a sample and a robust detection scheme able to resolve the dynamics induced by the light pulses on the sample. In this work, each of these three components are thoroughly investigated to introduce new tools for the analysis of ultrafast dynamics in molecules. Moreover, new methodologies are demonstrated for the analysis of ultrafast dynamics in different materials (atomic and molecular gases and crystals).

The results presented here are achieved using two different systems. The first is a titanium-sapphire-based laser that produces 4 fs (10^{-15} s) pulses at 800 nm. The system is employed to study argon and ammonia in the gas phase. The experiments aim at proving that field-sensitive events can be initiated, controlled and detected using few-cycle pulses. The system produces such ultrashort electric fields with a field strength comparable with the atomic binding energy. Because of these unique features, it is possible to impulsively ionize the gas samples and induce highly excited Rydberg states dynamics, as presented in this dissertation for argon, or inject vibrational wavepackets, here observed for ammonia cations. Once excited or ionized, the radiation emitted by the samples is field-resolved via electro-optic sampling (EOS) which allows for background-free detection. In contrast with other pump-probe techniques that rely on the measurement of XUV radiation [1], ions [2] or electrons [3], in these proof-of-principle experiments, here, only radiation up to the visible is employed. Specifically, a THz field is detected using IR-visible frequencies.

The combination of EOS and intense single-cycle pulses implemented in this work allows, for the first time to the author's knowledge, for the direct detection of the field emitted by Rydberg states beating and electron wavepacket in cations. These observations pave the way for the study of more complex systems and can reveal dynamics that were not accessible before.

The results call for the development of laser sources that can allow for a higher degree of tunability. The waveform synthesizer developed here gives this control over the field. The two-channel synthesizer employed in this dissertation is fed with a 2 μm optical parametric amplifier and provides 3.8 fs-long pulses at 1.7 μm. This platform enables shaping arbitrary electric fields with multi-octave bandwidth spanning from the visible to the IR,

with the electric field characterized via EOS. The field characterization of oscillations in the visible spectral range is usually achieved employing techniques based on highly nonlinear processes, like attosecond streaking or petahertz optical oscilloscopes. In this work, EOS is applied to reconstruct frequencies in the visible spectral range, up to 450 THz, despite being just a second-order nonlinear technique. Furthermore, EOS allows us to resolve arbitrary shapes of synthesized electric fields, while providing a high sensitivity and dynamic range. As a proof-of-principle, the synthesized pulses are applied to inject an electron wavepacket in a thin quartz sample, demonstrating that the injection can be confined in a time window of around 0.5 fs.

As a natural next step, the pulses out of the synthesizer can be applied to the study of cationic dynamics of molecules in the gas phase. The high degree of control offered by the synthesized pulses can be potentially exploited to optimise the desired output with a feedback loop and to coherently control ionized and nearly-ionized gas samples.

Zusammenfassung

Die meisten physikalischen Phänomene, die um uns herum auftreten, können durch Energie-Materie-Wechselwirkung beschrieben werden. Photonen können Energie effizient auf ein System übertragen und somit die Erforschung von Materie unter verschiedenen energetischen Regimen ermöglichen. In Form von Lichtpulsen können Photonen ultraschnelle Ereignisse auf einem bestrahlten Zielobjekt auslösen. Drei wesentliche Komponenten sind erforderlich, um diese Ereignisse auszulösen und zu erfassen: eine Lichtquelle, die ultrakurze Pulse erzeugen kann, eine Probe und ein robustes Detektionssystem, das die durch die Lichtpulse induzierte Dynamik auflösen kann. In dieser Arbeit wird jede dieser drei Komponenten gründlich untersucht, um neue Werkzeuge für die Analyse von ultraschnellen Dynamiken in Molekülen vorzustellen. Außerdem werden neue Methoden für die Analyse ultraschneller Dynamiken in verschiedenen Materialien (atomare und molekulare Gase und Kristalle) dargelegt.

Die hier vorgestellten Ergebnisse werden mit zwei verschiedenen Systemen erzielt. Das Erste ist ein Titan-Saphir-basierter Laser, der 4 fs (1 fs = 10^{-15} s) Pulse bei 800 nm erzeugt. Das System wird zur Untersuchung von Argon und Ammoniak in der Gasphase eingesetzt. Die Experimente zielen darauf ab, zu beweisen, dass feldsensitive Ereignisse durch Pulse mit wenigen Zyklen initiiert, kontrolliert und detektiert werden können. Das Lasersystem erzeugt derartige ultrakurze elektrische Felder mit einer Feldstärke, die mit der atomaren Bindungsenergie vergleichbar ist. Aufgrund dieser einzigartigen Eigenschaften ist es möglich, die Gasproben impulsartig zu ionisieren und die Dynamiken hochangeregter Rydberg-Zustände zu induzieren, wie in dieser Dissertation für Argon vorgestellt wird, oder Schwingungswellenpakete zu injizieren, wie hier für Ammoniak-Kationen beobachtet wird. Nach der Anregung oder Ionisation, wird die von den Proben emittierte Strahlung mittels elektro-optischer Abtastung (EOS) feldaufgelöst, was eine hintergrundfreie Detektion ermöglicht. Im Gegensatz zu anderen Pump-Probe-Techniken, die auf der Messung von XUV-Strahlung, Ionen oder Elektronen beruhen, wird in diesen Proof-of-Principle-Experimenten nur Strahlung bis zum Sichtbaren verwendet. Konkret wird ein THz-Feld detektiert mittels Frequenzen die vom IR bis zum sichtbaren Bereich reichen.

Die in dieser Arbeit realisierte Kombination von EOS und intensiven Pulsen mit nur einem Zyklus erlaubt, nach Kenntnis des Autors, zum ersten Mal den direkten Nachweis des Feldes welches von pulsierenden Rydberg-Zuständen und Elektronenwellenpaketen in Kationen emittiert wird. Diese Beobachtungen ebnen den Weg für die Untersuchung komplexerer Systeme und können Aufschluss über Dynamiken geben, die vorher nicht zugänglich

waren.

Die Ergebnisse fordern die Entwicklung von laserbasierten Strahlungsquellen, die einen höheren Grad an Abstimmbarkeit ermöglichen. Der hier entwickelte Wellenformsynthesizer bietet diese erforderliche Kontrolle über das Feld. Der Zweikanal-Synthesizer, der in dieser Dissertation verwendet wird, wird mit einem 2 μm optischen parametrischen Verstärker gespeist und liefert 3.8 fs lange Pulse mit einer Wellenlänge von 1.7 μm. Die Plattform ermöglicht die Modellierung beliebiger elektrischer Felder mit einer Bandbreite von mehreren Oktaven, die vom Sichtbaren bis zum IR reichen. Ihre elektrischen Feldformen werden mittels EOS charakterisiert. Die Feldcharakterisierung von Schwingungen im sichtbaren Spektralbereich wird üblicherweise mit Techniken erreicht, die auf hoch nichtlinearen Prozessen basieren, wie Attosekunden-Streaking oder mit optischen Petahertz-Oszilloskopen. In dieser Arbeit wird EOS erstmals zur Rekonstruktion von Frequenzen im sichtbaren Spektralbereich, bis zu 450 THz verwendet, obwohl es sich nur um eine nichtlineare Technik zweiter Ordnung handelt. Außerdem erlaubt uns EOS beliebige Formen synthetischer elektrischer Felder aufzulösen und bietet dabei eine hohe Empfindlichkeit und einen großen Dynamikbereich. Als Proof-of-Principle werden die synthetisierten Pulse angewendet um ein Elektronen-Wellenpaket in einer dünnen Quarz-Probe zu injizieren, was zeigt, dass dieser Prozess in einem Zeitfenster von etwa 0.5 fs eingegrenzt werden kann.

Als natürlicher nächster Schritt können die Pulse aus dem Synthesizer für die Untersuchung der kationischen Dynamiken von Molekülen in der Gasphase eingesetzt werden. Der hohe Grad an Kontrolle, der durch die synthetisierten Pulse ermöglicht wird, kann potenziell genutzt werden, um das gewünschte Ergebnis innerhalb einer Rückkopplungsschleife zu optimieren und für die kohärente Steuerung von ionisierten und fast ionisierten Gasproben zu nutzen.

List of Abbreviations

ADK	Ammosov-Delone-Krainov theory
AGS	silver gallium sulphite
AOPDF	acousto-optic programmable dispersive filter
ARPES	angular-resolved photoelectron spectroscopy
BBO	beta-barium borate, β-BaB_2O_4
BPF	band-pass filter
CCD	charge-coupled device
CEP	carrier envelope phase
CM	Chirping mirrors
CPA	chirped pulse amplification
DFG	difference-frequency generation
DS	delay stage
EOS	electro-optic sampling
FFT	fast Fourier transform
FROG	frequency-resolved optical gating
FRS	fi eld resolved spectroscopy
FTI	frustrated tunnelling ionization
FTIR	Fourier-transform infrared spectroscopy
FWHM	full width at half maximum
FWM	four-wave mixing
GaP	gallium phosphide
GD	group delay
GDD	group-delay dispersion
HCF	hollow-core fiber
HHG	high harmonic generation
HOMO	highest occupied molecular orbital
IR	infrared
ISRS	instantaneous stimulated Raman scattering

IVR	internal vibrational relaxation
LGS	lithium gallium sulphite
LO	local oscillator
MATI	mass analyzed threshold ionization
NL	nonlinear
NPS	nonlinear photoconductive sampling
OPA	optical parametric amplification
OPCPA	optical parametric chirped pulse amplification
OR	optical rectification
PD	photodiode
PEC	potential energy curve
PES	photoelectron spectroscopy
PPLN	periodically polled lithium niobate
REMPI	resonant multi-photon ionization
SAEP	single active electron approximation
SFG	sum-frequency generation
SHG	second-harmonic generation
SNR	signal-to-noise ratio
SPIDER	spectral phase interferometry for direct electric-field reconstruction
SRS	stimulated Raman scattering
TDSE	time-dependent Schrödinger equation
TFISH	THz fi
	eld induced second harmonic generation
Ti:Sa	titanium-doped sapphire, Ti^{3+}:Al_2O_3
TMF	transient molecular fi
	ngerprint
TOF	time of flight detector
UV	ultraviolet
XUV	extreme ultraviolet
Yb:YAG	ytterbium-doped yttrium aluminum garnet, Yb^{3+}:$Y_3Al_5O_{12}$
WP	Wollaston prism
ZEKE	zero kinetic energy spectroscopy

List of Figures

Introduction

I try to push the colors through a prism back to white
To sync our different pulses into a blinding light
And if love is not the key...
I hope that I can find a place where it could be.
Asaf Avidan - Different Pulses

Until the 17^{th} century, the Latin word "spectrum" was exclusively used as a synonym for "apparition". Newton, for the first time, gave this name to the sequence of colors that, indeed, appear when the sun shines on a glass prism. After that, Fraunhofer identified the absorption lines of the sun and assigned them to the absorption spectrum of sodium. His pioneering work laid the foundations of what we nowadays call spectroscopy. In its early stage spectroscopy was mainly applied to the study of celestial bodies. We have to wait until the end of the 19^{th} century to have the first measurements of atomic levels and the advent of quantum mechanics to understand their nature.

Over the years, the gist of spectroscopy has not changed much. Light emitted from, or absorbed by, a sample is analysed by looking at its frequency components. This technique can reveal the microscopic nature of the sample and how photons, the constituents of light, change its property. In other terms, spectroscopy studies how light interacts with matter. Today, the samples under study span from simple molecules to clusters [4] and complex nano-structures [5]. Light sources have achieved tremendous developments as well, merging technology with a deep understanding of the physics behind it.

The invention of highly spatially and temporally coherent sources, lasers, marked a revolution in this field. Lasers made it possible to select specific transitions and to drastically increase the spectral resolution. These unique sources allowed doing spectroscopy in a time-resolved fashion with unprecedented results. Their capability of producing short light pulses triggered the curiosity of many scientists around the world over the last five decades. Shorter pulses indeed means being able to resolve faster events.

Spectroscopy entered a new era when laser sources reached pulse durations in the femtosecond (fs) regime, one quadrillionth of a second [6]. This time scale is particularly intriguing being the one in which molecular vibrations occur. Light with such a short pulse duration can be used to manipulate chemical reactions and achieve coherent control [7]. More recently this limit has been pushed to the attosecond time scale, thus allowing for the exploration of electrons dynamics in solids [8, 9] and gasses [10].
All these observations usually rely on a powerful pulse used to pump and initiate the re-

action, and a second weaker pulse that probes the end products. By changing the time delay between these two pulses is possible to acquire different frames of a reaction. This detection scheme is called "pump-probe" and is an essential technique in all time-resolved spectroscopic experiments.
Pump-probe measurements are typically performed by investigating the spectrum of the probe beam. However, they can also be implemented to resolve electric fields. This application becomes particularly useful when the sampled pulse is only a few cycles long and can reveal information not directly accessible only from its spectrum.
When electric fields are intense enough, two or more photons can interact simultaneously with a sample. Because of this nonlinear interaction, dynamics even faster than the pulse duration can be explored. Few and sub-cycle pulses can easily reach intensities able to ionize molecules in the gas phase. In a solid, instead, ultrashort pulses can be employed to drive electron wavepackets in a highly confined fashion.
At this point one question rises: *how can we apply intense sub-cycle pulses and field-sensitive detection techniques to spectroscopy?*

This thesis answers the question above in the framework of terahertz and visible-infrared field-resolved metrology. The research presented here evolves along two directions: the first is the application of short pulses to the investigation of vibrations induced by impulsive ionization and the second is the generation and detection of sub-cycle pulses in the visible-infrared spectral region. The detection is done in both cases with electro-optic sampling (EOS) [11]. This technique, which use is well established in the THz spectral region, has been demonstrated to work even at higher frequencies [12, 13]. In this work, the spectral limits of EOS are pushed up to the visible spectral region of light, thus, filling the gap between conventional photodiodes and fully optical field-resolved detection. High sensitivity and easy implementation are just two of the advantages of this technique which will be described in more details in the following chapters. The dynamics under studies will be two: the direct observation of Rydberg-states beating in argon atoms and the umbrella modes of ammonia cations.
This dissertation has the following structure:

Chapter 1 introduces the theoretical background necessary to understand the main ideas and concepts behind this research. This chapter equips the reader with the most important mathematical and experimental tools used in this dissertation. This chapter stresses how light can control and induce ultrafast electronic motions. Both perturbative and non-perturbative regimes are introduced. The first is used to describe the processes behind pulse amplification and broadening, the second to explain ionization. Different schemes of how to generate and detect single-cycle pulses are presented. Applications involving the control that light has over electrons is shown in several contexts like high harmonic generation and coherent control. In the last part, it will be discussed how the energy of the electrons from ionized molecules can be used to extract information on the energy levels of cations through photoelectron spectroscopy and, in particular, zero kinetic energy spectroscopy.

Chapter 2 is mainly focused on the description of the electron dynamics following the ionization of an atomic gas by a single-cycle pulse. We will see how this process results

in the emission of terahertz radiation which characterization is crucial to get access to unique molecular signatures. The main dependencies of this radiation from the pump laser properties are demonstrated and measured. Thanks to EOS detection, dynamics following ionization can be examined. In the case of argon, this will allow here the detection of dynamics involving highly excited Rydberg states.

Chapter 3 explores molecular signatures of ionised ammonia. In particular, the quest for specific vibrational modes and their origin is presented. Previous theoretical and experimental studies with photoelectron spectroscopy have been used as references for the results shown here. This chapter demonstrates how it is possible to control the population of ionized states by changing the symmetry of the ionizing laser pulses.

Chapter 4 shows the tools needed to generate sub-cycle pulses in the infrared-visible spectral range. In particular, the spectrum out of a thin hollow-core fiber is studied. This presents unique features due to the highly nonlinear processes happening inside the fiber. Furthermore, in this chapter is presented a multi-channel waveform synthesizer able to generate sub-cycle pulses as short as 3.8 fs at 1.7 μm. It is demonstrated how different transients can be synthesized by changing the arrival time of the different channels and their carrier-envelope phase. The pulses are then used to drive ultrashort electron wavepackets in a thin quartz sample. Furthermore, these measurements give access to the EOS sampling pulse via nonlinear photoconductive sampling.

Chapter 5, finally, sums up all the results and presents future applications that can derive from them.

Chapter 1

Theoretical background

The main goal of this chapter is to present the mathematical and experimental tools that constitutes the backbone of this work. In the first part, the concepts introduced are related to the theory behind ultrashort pulses (section 1.1) and nonlinear optics (section 1.2). It is explained how to generate ultrashort light transients and why they play a central role in the study and control of molecular dynamics. In section 1.2, the main perturbative nonlinear interactions of light with matter is discussed, mainly referring to their implications on ultrashort pulses. Here, it is explained how it is possible to take advantage of nonlinear processes to directly measure electric fields. Different pulse retrieval techniques are illustrated with their advantages and disadvantages in section 1.3.2. Among these electro-optic sampling (EOS) is described in more details. The working principle of this field-resolved method is demonstrated, together with its limits and potentialities. A second technique, nonlinear photoconductive sampling (NPS), is also discussed. Both EOS and NPS are used to resolve sub-cycle pulses later on in chapter 4.

In the second part of this chapter, nonlinear optics is illustrated taking into account not only the perturbative regime but also considering non-perturbative effects. Both can be described by the Keldysh parameter, which is introduced in section 1.4. Particular attention is given to tunnelling ionization. This type of ionization is recalled later in chapter 2. In section 1.6, some of the applications of ultrashort pulses to atoms and molecules are discussed. The theory discussed here is mainly focused on the Schröndinger equation, plasma and Rydberg physics. Under a more experimental perspective, the study of atoms and molecules is carried out considering photoelectron techniques and, in particular, zero kinetic energy spectroscopy.

In conclusion, this chapter presents how the interaction of ultrashort pulses with matter can be described and detected in the case of gaseous media and why it is worth studying it.

1.1 Ultrashort pulses

From Maxwell's equations it can be derived that the relation between the magnetic and the electric component of electromagnetic radiation is the following:

$$|B| = |E|/c \tag{1.1}$$

where B and E are the magnetic and electric field, respectively, and c is the speed of light. This equation implies that the magnetic contribution is negligible compared to the one due to the electric field, therefore, only the electric component are taken into account in this work. If we ignore the spatial distribution, in the time domain the real electric field, $\mathcal{E}(t)$, takes the following form:

$$\mathcal{E}(t) = \frac{1}{2}A(t)e^{i[\omega_0 t - \phi(t)]} + c.c. \tag{1.2}$$

where A(t) is the real pulse envelope, ω_0 is the pulse central frequency, $\phi(t)$ is the temporal phase and c.c. indicates the complex conjugated. We can assume from now on that A(t) has a Gaussian profile and define the pulse duration as its full-width-at-half-maximum (FWHM). This approximation works particularly well for short pulses, the main focus of this chapter. To simplify the analysis, we can rewrite equation 1.2 in its complex form:

$$\tilde{E}(t) = \tilde{A}(t)e^{i[\omega_0 t - \phi(t)]} \tag{1.3}$$

The interaction of light with matter reflects mainly on $\phi(t)$. This factor contains most of the information in which we are interested and it is therefore analysed in more details. The role played by the temporal phase becomes clear when looking at the Fourier transform of $\tilde{E}(t)$:

$$\tilde{E}(\omega) = \sqrt{S(\omega)}e^{-i\varphi(\omega)}. \tag{1.4}$$

Here $S(\omega)$ is the spectrum and $\varphi(\omega)$ the spectral phase, the equivalent of the temporal phase in the frequency domain, and describes the phase of the pulse spectral components. We can now look at different orders of the power expansion of $\varphi(\omega)$ around the pulse central frequency ω_0 and illustrate their role:

$$\varphi(\omega) = \varphi(\omega_0) + \underbrace{\frac{d\varphi}{d\omega}_{|\omega=\omega_0}}_{\text{GD}}(\omega - \omega_0) + \underbrace{\frac{d^2\varphi}{d\omega^2}\Big|_{\omega=\omega_0}}_{\text{GDD}}\frac{(\omega - \omega_0)^2}{2!} + ... \tag{1.5}$$

In this expression, GD stands for group delay, while GDD for group delay dispersion. The last term affects the pulse envelope by stretching, or "chirping", it symmetrically around its peak. A GDD higher or lower than 0 means indeed that different frequencies arrive at different times. The GD, instead, affects the relative phase of the field within the envelope over time but does not disperse the different spectral components. This factor plays a role only for few-cycle pulses. The reason for this is that it changes the carrier-envelope phase (CEP) from pulse to pulse. Figure 1.1 shows how the CEP affects the profile of the field only in the case of a few-cycle pulse. The asymmetric profile of the field in Figure 1.1b

(blue line) can be changed to symmetric by setting the CEP to $\pi/2$ (orange line). It is this degree of control over the asymmetry of a pulse that makes them appealing and allows for the study of field sensitive phenomena, like the ones studied in this thesis.

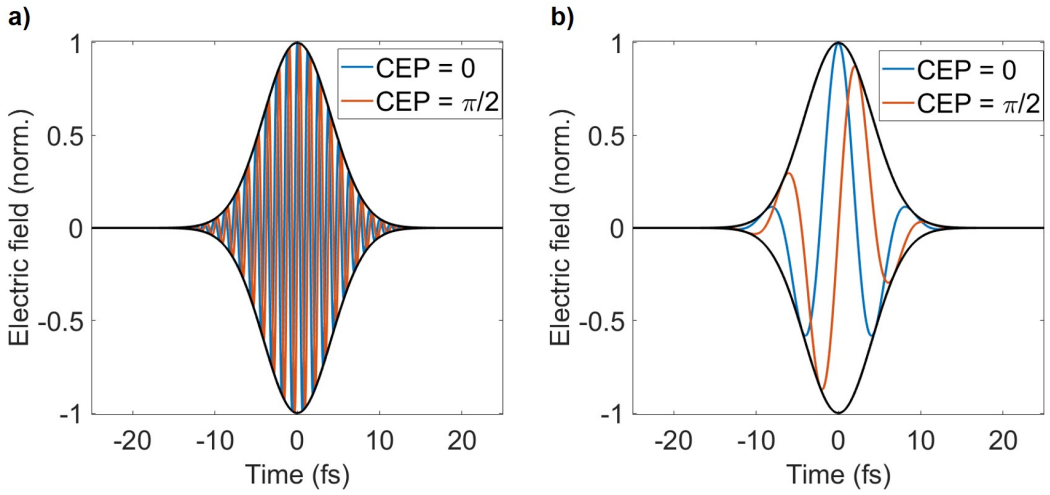

Figure 1.1: Multi-cycle vs few-cycle pulse. The two plots show two cases in which the CEP changes from 0 to $\pi/2$. It is clear how the shape of the field in (a) is mainly defined by its envelope and does not change at different values of the CEP. On the other hand, the CEP changes the shape of the field in (b) from a cosine-like (CEP=0) to a sine-like (CEP $= \pi/2$) function.

One of the goals of the work presented here is to generate sub-cycle pulses. These are particularly affected by the propagation through a material. It is therefore important to know how a pulse interacts with matter. In general, when light travels through a material, its spectral components are dispersed and its spectrum, $S(\omega)$, changes according to the complex refractive index, $\tilde{n}(\omega)$, of the material. In particular, the real component of $\tilde{n}(\omega)$ induces a phase shift given by the following equation:

$$\Delta\phi = \frac{\mathrm{Re}(\tilde{n}(\omega))\omega}{c} d \tag{1.6}$$

where d is the thickness of the material. The imaginary part of $\tilde{n}(\omega)$, instead, affects the amplitude of the spectral components according to:

$$\tilde{S}'(\omega) = \tilde{S}(\omega) e^{-\frac{\mathrm{Im}(\tilde{n}(\omega))\omega}{c} d} \tag{1.7}$$

where S' is the spectrum out of the material and S the incoming one. The latter equation is also used to describe linear absorption.

The two equations above imply that we can control the shape of a pulse by carefully choosing the right $\tilde{n}(\omega)$.

Shaping techniques rely on this concept to produce arbitrary waveforms. This control is conventionally achieved according to three steps below:

1. the pulse frequency components are dispersed using diffractive optics;
2. the beam, after collimation, is sent through a phase and amplitude mask;
3. the spatially dispersed frequencies are then recombined.

This procedure shifts the problem from finding a material with the right $\tilde{n}(\omega)$ to setting up a phase/amplitude mask complex transmission function, $Y(\omega)$, which gives the wanted field shape, $\tilde{E}'(\omega)$, from the incoming complex field, $\tilde{E}(\omega)$:

$$\tilde{E}'(\omega) = Y(\omega)\tilde{E}(\omega) \tag{1.8}$$

Figure 1.2a shows a schematic of the pulse shaping technique just described.

Materials have the drawback of not having a simple analytical form of $\tilde{n}(\omega)$. Having the ability to customize $Y(\omega)$ is, therefore, an advantage if one wants to change the different orders of $\varphi(\omega)$ separately. The setup shown in Figure 1.2a is just one of the configurations through which it is possible to control the spectral phase of a pulse. Other beam shaping techniques are based on dispersing the beam with prisms, instead of gratings, or on dielectric multilayer mirrors, also known as chirped mirrors [14]. These mirrors are made of thin layers of two different materials that are alternated with increasing widths on a substrate. The configuration and the material of the layers are what determines the final GD curve.

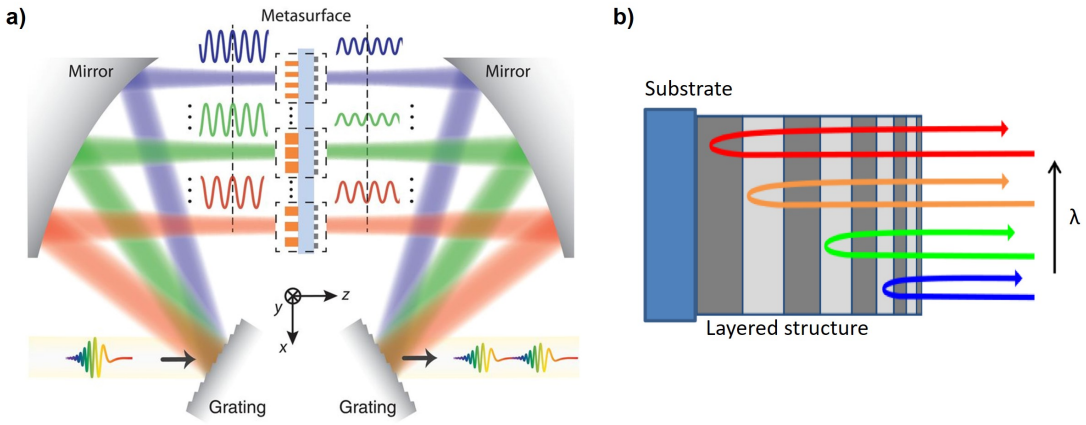

Figure 1.2: Beam shaping techniques. (a) The incoming beam is sent through a metasurface after being spatially dispersed by a grating. The metasurface controls separately the amplitude and the phase of the light transmitted by respectively rotating nanostructures and changing their transversal size (along the x-y plane). (b) Design of a chirped mirror. Longer wavelengths are reflected by layers closer to the substrate. This configuration imparts a negative GDD to the incoming pulse. Pictures edited from [15] (a) and [16] (b).

Chirped mirrors have the advantage of being compact and can be custom made. On the other hand, they are not actively tunable. For this reason, these special dielectric mirrors are used to compensate for a given material dispersion. Their structure makes them particularly suitable to deal with ultrashort pulses. They can indeed support spectra spanning more than one octave. With the right choice of materials they can be used to compress pulses in the infrared (IR) and can also be adapted to work down to the ultraviolet (UV) [17]. In a multi-layer structure, a wave is reflected when it impinges on a layer when its wavelength is comparable to the thickness of the layer. This implies that operating in the UV requires particularly thin layers making their production technically challenging and therefore requiring advanced layer-deposition techniques [18].

1.2 Nonlinear optics

So far we have limited the analysis to linear effects. New physics unfolds when we take into account the nonlinear action of light on matter. The analysis and the formalism presented here is based on [19]. The way electric fields interact with matter is through electromagnetic force. In a dielectric, this force distorts the electron cloud around its atoms, resulting in a net dipole moment given by:

$$\tilde{p} = \delta q \tag{1.9}$$

where δ is the charge displacement and q is the electric charge. The polarization, P, can be defined as the density of these induced dipoles. From Maxwell's equations it can be derived that P is related to the electric field via the following equation:

$$\tilde{P} = N\tilde{p} = \epsilon_0 \chi \tilde{E} \tag{1.10}$$

where N is the density of charges, ϵ_0 is the vacuum permittivity and χ is the susceptibility tensor. If a time varying electric field, $\tilde{E}(t)$, is strong enough, it can affect the optical properties of a material. It results that $\tilde{P}(t)$ does not depend linearly on $\tilde{E}(t)$ but non-linearly. The analysis that follows is done under the perturbative approximation, which implies that $\tilde{E}$ is weaker than the ionization potential. This regime allows the use of a convergent power series expansion of $\tilde{E}(t)$:

$$\tilde{P}(t) = \epsilon_0[\chi^{(1)}\tilde{E}(t) + \chi^{(2)}\tilde{E}^2(t) + \chi^{(3)}\tilde{E}^3(t) + ...] \tag{1.11}$$

The superscript on χ indicates the tensor's order. The first term on the right side is just the linear contribution, while the other terms constitute what is defined as nonlinear polarization, $\tilde{P}_{NL}$. Now, we would like to have a way to measure this factor to understand how a strong field changes the instantaneous properties of a material. Keeping in mind that time varying dipoles are sources of radiation, we can write a wave equation that takes into account the nonlinear polarization:

$$\nabla^2\tilde{E} - \frac{\epsilon^{(1)}}{c^2}\frac{\partial^2\tilde{E}}{\partial t^2} = \frac{1}{\epsilon_0 c^2}\frac{\partial^2\tilde{P}^{NL}}{\partial t^2} \tag{1.12}$$

here $\epsilon^{(1)}$ is the relative permittivity of the material. From this equation it is possible to calculate how the radiation emitted from the nonlinear components propagates and builds up in a material. To know at which frequency the nonlinear component of the dipoles oscillates we have to look back at equation 1.11. If we stop the expansion at the second term on the right hand side, it follows that the material interacts with up to two photons at the same time. We can consider the general case in which these two fields, $\tilde{E}_1$ and $\tilde{E}_2$, have different frequencies, ω_1 and ω_2. Being $\tilde{E}$ a complex function given by:

$$\tilde{E}(t) = Ee^{-i\omega t} + c.c. \tag{1.13}$$

it results that $\tilde{E}^2$ takes the following form:

$$\begin{aligned}(\tilde{E}_1 + \tilde{E}_2)^2 =& E_1^2 e^{-i(2\omega_1)t} + 2\epsilon_0\chi^{(2)}E_1E_1^* + 2E_1E_2e^{-i(\omega_1+\omega_2)t} + E_1E_2^*e^{-i(\omega_1-\omega_2)t} + \\ &+ 2\epsilon_0\chi^{(2)}E_2E_2^* + E_2^2e^{-i(2\omega_2)t} + c.c.\end{aligned} \tag{1.14}$$

In 1.14 different terms indicate different frequency generation processes. The first and the last term lead to the second harmonic generation (SHG) of the fundamental frequencies, the second and the fifth to optical rectification (OR), the third to the sum of the two frequencies (SFG) and the fourth to their difference (DFG), shown in Figure 1.3a. DFG is the process through which optical parametric amplifiers (OPA) coherently transfer power from a pump (ω_1) to a seed (ω_2) pulse. The third component (ω_3) is called idler and its build-up can compromise the amplification of the seed. DFG can also be used to down-convert an incoming beam. Using a single pulse with a broad spectrum, it is possible indeed to mix two frequencies of the same pulse to generate lower frequencies. A feature of this process, called intrapulse DFG, is that the CEP of the idler is intrinsically stable, making it not sensitive to CEP fluctuations of the pump. The same analysis done above for $\tilde{E}^2(t)$ can be extended to $\tilde{E}^3(t)$ by stopping the Taylor expansion at the third order. This time there are three fields interacting resulting in 44 different terms instead of 16 like in equation 1.14. Among those, we are mainly interested in the following term:

$$\tilde{E}(\omega_4) = \tilde{E}(\omega_1 + \omega_2 - \omega_3). \tag{1.15}$$

This process is called four-wave-mixing (FWM) because it involves four different frequencies (see Figure 1.3b). In a cascade process, like the one happening in a fiber, FWM results in the spectral broadening of an incoming beam. If we look at the temporal domain, it can be demonstrated that FWM does not affect the envelope of a pulse and that longer wavelengths are at the leading edge while shorter ones at the trailing edge. It follows that an incoming compressed pulse is chirped after FWM but has a shorter Fourier limit.

Figure 1.3: Schematic of DFG and FWM. The two processes sketched here show how DFG (a) and FWM (b) are generated. Both processes are parametric, which means that energy is not transferred to the medium. Only virtual levels are indeed involved in these interactions. Arrows which point upward/downward mean that a photon is absorbed/emitted.

The spatial equivalent of FWM is the Kerr effect. This effect is given by the nonlinear dependence of the medium on the real refractive index, n:

$$n(r,t) = n_1 + n_2 I(r,t) \tag{1.16}$$

where n_1 and n_2 are respectively the linear and the nonlinear component of n and I is the pulse intensity. Because more intense regions experience a higher refractive index, the Kerr effect results in the self-focusing of a beam. When n_2 scales linearly with the electric field is instead called the Pockels effect. In the latter case, the mixing happens between an oscillating and a static field. The process can be described as SFG where one pulse has a frequency of ω while the other one of zero. We will come back to the Pockels effect later in section 1.3.2.

From eq. 1.14 it is clear that we need a discriminating factor to allow just one of the processes to dominate over the others and ultimately to build up coherent radiation at a given frequency. This discrimination is imparted by the susceptibility of the material. The form of χ depends indeed on the material's structure. For example, if a medium is centrosymmetric $\chi^{(2)}$ is identically zero. Gasses fall into this category, making them suitable for FWM. Crystals like lithium niobate and beta-barium-borate (BBO) have instead an asymmetric lattice, so second-order effects can take place. To discriminate among all possible processes, crystals can be grown or cut such that only one process is favoured. This property is called phase-matching. The crystal structure is not the only factor that determines the phase-match. Its thickness also has an influence on the bandwidth and on the output power of the process. Because both energy and momentum conservation have to be fulfilled, for a thick crystal the phase-matching favours only a narrowband portion of the spectrum. In general, the output intensity of a second-order nonlinear process is given by:

$$I = I^{(max)} sinc^2(\Delta k L/2) \tag{1.17}$$

where Δk is the wave vector mismatch and L is the length of the crystal. This expression shows how the crystal properties reflect on the generation of new frequencies through Δk. There are different ways to obtain mismatching wave vectors that satisfy the equation above over a broad spectrum. Birefringent crystals are one option as well as quasi-phase-matched crystals. The latter is produced by alternating the ferroelectric domains of a crystal with a period given by twice the coherent length ($L_{coh} = 2/\Delta k$). In chapter 4 is presented a laser system that makes use of both these types of phase-matching.

1.3 Pulse characterization techniques

1.3.1 Spectral phase techniques

The nonlinear processes described in the previous section can be employed to reconstruct the spectral phase of ultrashort pulses. In general, it is possible to resolve a pulse only if it is sampled by a shorter gating pulse. Nevertheless, this condition can be loosened when nonlinear phenomena are considered. For example, second harmonic frequency-resolved optical gating (SHG-FROG) gives access to the envelope of a pulse by mixing it with a replica in a crystal, phase-matched for SHG [20]. The idea behind this detection scheme is shown in Figure 1.4a. Changing the delay between the two replicas results in changes in the SHG intensity according to the following relation:

$$I_{FROG}(\omega, \tau) \propto \left| \int_{-\infty}^{\infty} E_{sig}(t, \tau) e^{-i\omega t} dt \right|^2 \tag{1.18}$$

where E_{sig} depends on the type of nonlinear interaction. In the case of SHG it can be written as:

$$E_{sig} = E(t)E(t - \tau) \tag{1.19}$$

where τ is the time delay between the two pulses. The information of the pulse envelope is not directly provided by SHG-FROG and to retrieve it it is necessary to use an algorithm.

A similar technique which instead does not require a retrieval algorithm is called spectral phase interferometry for direct electric-field reconstruction (SPIDER) [21]. Two delayed identical test pulses are up-converted using a chirped pulse in a crystal and coupled to a spectrometer (see Figure 1.4b). In this case the signal is given by:

$$\begin{aligned} I_{SPIDER}(\omega, \tau) &= |E(\omega) + E(\omega - \Omega)e^{-i\omega t}|^2 \\ &= I(\omega) + I(\omega - \Omega) + 2\sqrt{I(\omega)I(\omega - \Omega)}cos[\varphi(\omega) - \varphi(\omega - \Omega) - \omega t] \end{aligned} \tag{1.20}$$

SPIDER has the main drawback of suffering from coherent artefacts and, like FROG, gives access only to the pulse envelope but not to the field.

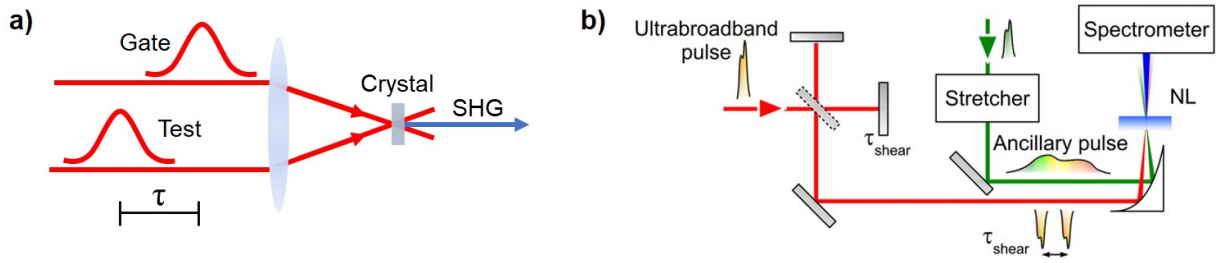

Figure 1.4: Schematic of FROG and SPIDER. (a) SHG-FROG can sample a test pulse using a time-delayed replica (gate). The two beams are focused on a crystal and the time-dependent SHG is coupled to a spectrometer. (b) In SPIDER a single ultrabroad pulse is split into three pulses. Two are time-delayed replicas while the third is stretched and combined with the other two pulses in a nonlinear (NL) crystal where the two replicas are upconverted and coupled to a spectrometer. Image (b) edited from [22].

1.3.2 Field sensitive techniques

EOS

Envelope sensitive measurements do not reveal field-sensitive effects. In other terms, techniques like FROG and SPIDER are not CEP sensitive. As shown in Figure 1.1 in the case of few-cycle pulses it is crucial to get access to the field since this can differ substantially from its envelope. Electro-optic sampling (EOS) is a field-sensitive technique that has been extensively used to characterize fields in the THz regime [23, 11, 24] and more recently has been extended to the mid- [25] and near-infrared [13]. In the few THz spectral region, EOS can be described in terms of Pockels effect. A THz field induces a polarization rotation of a sampling pulse when they temporally and spatially overlap in a $\chi^{(2)}$ crystal. The change in polarization can be detected using an ellipsometer. Time-resolving this quantity gives direct access to the test pulse electric field. Unlike the techniques shown before, in EOS the test field cannot be used to sample itself but the sampling pulse needs to be shorter. We have to change picture if we want to describe EOS when the frequencies to sample are higher than the inverse of the pulse duration. In this case, EOS provides the electric field of a test pulse by time-resolving the interference between an up-converted version of the test pulse and a sampling pulse, which acts as a local oscillator in a heterodyne detection scheme. The way this process can be detected is through ellipsometry. This can be implemented by employing a Wollaston prism, which spatially splits a beam into its orthogonal polarization components, and a balanced photodiode (see Figure 1.5b). Figure 1.5a shows the main idea behind EOS detection. An IR (or THz) pulse is up-converted in the visible spectral region by a short sampling pulse. The blue components of the last overlap with the up-converted test pulse and only the overlapping region is then detected by the balanced detection. The up-conversion has the big advantage of shifting the detection in a spectral range where conventional Si detectors work efficiently.

Given that the information is contained just in the blue part of the sampling pulse, filtering out the other spectral components with a band-pass filter is possible to increase the signal to noise ratio (SNR) [26]. This equips EOS with a great sensitivity and dynamic range that makes it able to resolve both strong and weak electric fields [27, 28].

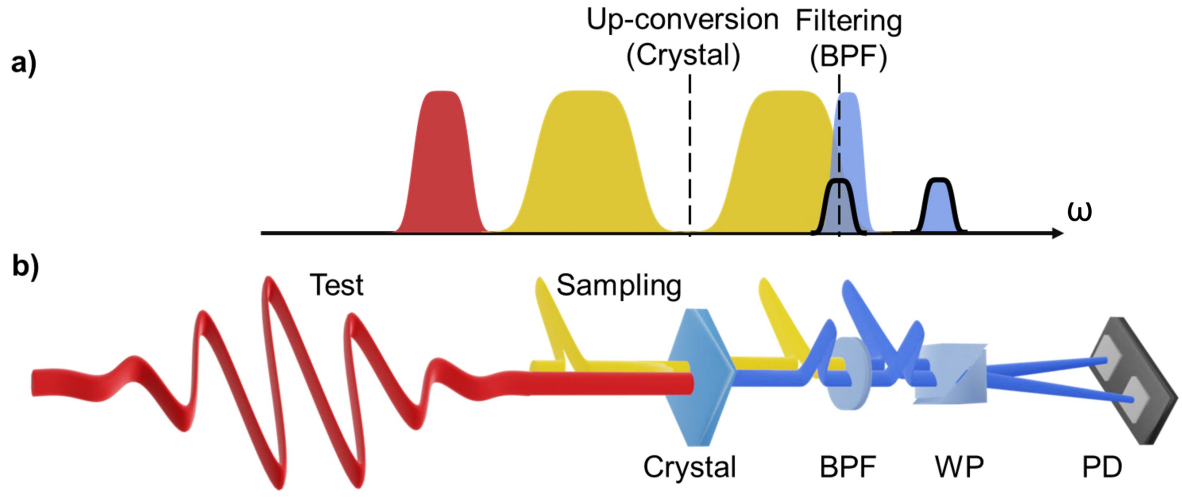

Figure 1.5: EOS detection mechanism. (a) reports the processes underlying EOS detection in the frequency domain. The test pulse (red) is up-converted in the EOS crystal by the sampling pulse (yellow). The spectrally overlapping portion of the sampling pulse and the up-converted test pulse is then sent through a band-pass filter (BPF). The beam is finally split into two orthogonally polarized components using a Wollaston prism (WP) and sent to a balanced photodiode (PD). (b) shows a schematic of the setup.

The ellipsometer is balanced such that the same intensity impinges on the two photodiodes without test pulse. When sum frequency is generated, the signal on the two photodiodes is unbalanced, thus allowing for the detection of the test field. From this configuration it results that one photodiode detects a total intensity of $|E_s + E_{SFG}|^2$ while the other one of $|E_s - E_{SFG}|^2$. We can now write down the detected signal in terms of the electric field of the test (E_{Test}) and sampling pulse (E_s):

$$|E_s + E_{SFG}|^2 = E_s^2 + E_{SFG}^2 + 2E_sE_{SFG} = E_s^2 + E_{SFG}^2 + 2E_s^2E_{Test} \tag{1.21}$$

$$|E_s - E_{SFG}|^2 = E_s^2 + E_{SFG}^2 - 2E_s^2E_{Test} \tag{1.22}$$

here $E_{SFG} = E_sE_{Test}$ is the electric field of the sum-frequency. The EOS signal is given by doing the difference between equation 1.21 and equation 1.22:

$$|E_s + E_{SFG}|^2 - |E_s - E_{SFG}|^2 = 4E_s^2E_{Test} \tag{1.23}$$

The term obtained is proportional to the test field and the sampling pulse intensity. The latter, in a first approximation, being just a constant, can be assumed to not affect the EOS readout. This simple expression just obtained proves that EOS does not require any retrieval algorithm to access the information contained in the field.

Based on the crystal used for the up-conversion we can either have SFG or DFG between the test and the sampling pulse. In this work, we consider only the case of SFG, where the up-converted test pulse interferes with the shorter wavelength components of the sampling pulse.

Ideally, the signal detected should be directly proportional to E_{Test} as proved in equation 1.23. This holds only if all the components used in the setup have a flat spectral response and if the sampling pulse is compressed down to its Fourier limit. In a real case scenario, a deconvolution is necessary to know the test pulse before the EOS crystal [29]. To deconvolve the field we can follow the beam path shown in Figure 1.22b and go through each component. Test and sampling pulse interact first in the EOS crystal where SF is generated. The propagation in the crystal can be obtained from the following equation:

$$\frac{\partial E_\omega(z)}{\partial z} = -ik_\omega(z)E_\omega(z) - \frac{i\omega}{2n_\omega\epsilon_0 c}P_\omega^{NL}(z) \tag{1.24}$$

From the expression above it is possible to simulate how a broadband test pulse and the sampling pulse propagate in the crystal. We can calculate as well how the SFG changes as a function of the time delay between the two pulses and, therefore, obtain the signal on the two photodiodes. This derivation implies that we know in advance the spectral phase of the sampling pulse. If we now take into account the spectral response of the BPF and of the photodiodes, we can obtain the full response function of our EOS setup by dividing the simulated spectrum with the measured one. The final analytical form of the response function is the following:

$$S(\Omega) = \int_\Omega^\infty d\omega_s R(\omega_s)|E(\omega_s)||E(\omega_s - \Omega)|e^{i[\varphi(\omega_s)-\varphi(\omega_s-\Omega)]} \tag{1.25}$$

where Ω is a test pulse frequency. $|E(\omega_s)|e^{i\varphi(\omega_s)}$ and ω are the complex spectral amplitude and the spectrum of the sampling pulse, respectively. $R(\omega_s)$ is the product of the spectral response of the crystal, the band-pass filter and the photodiodes.

Photoconductive antennas offer an alternative to EOS [30]. However, their sensitivity drops above 100 THz [31, 32]. Operating EOS above 100 THz would have the advantage of both avoiding the phonon modes of the EOS crystal as well as having a high sensitivity in the visible and near IR-spectral ranges [33]. Photoemission and photoionization are instead two alternatives able to resolve fields in the visible range [34, 35, 36, 37] but their implementation is more complex than the one of EOS as is explained in the next sections.

NPS

In the previous section, we saw how it is possible to resolve electric fields using a fully optical simple setup. Despite being a versatile technique, EOS is mainly limited by the

sampling pulse duration. If we could "shrink" the gating to shorter transients we would be able to resolve shorter wavelengths. This can be achieved by exploiting the optical properties of dielectrics. For example, if we look at the band-gap energy of SiO_2 (9.3 eV), it is six times larger than 1.55 eV, the energy of a photon at 800 nm (the central wavelength of commercial Ti:Sa systems). This implies that six photons are needed to inject electrons from the valence to the conduction band. The injected electron wavepacket is therefore as short as the sixth power of the injecting field. A way to obtain an electron wavepacket that is even more confined in time is to increase the nonlinear order necessary to inject carriers. This can be achieved by employing a wider bandgap material, like LiF_2 (14 eV) but increasing the central wavelength of the injecting pulse does not have the same effect. The duration of the wavepacket is indeed proportional to the injecting pulse duration, therefore, in this case, a higher nonlinear order does not produce a shorter injection.

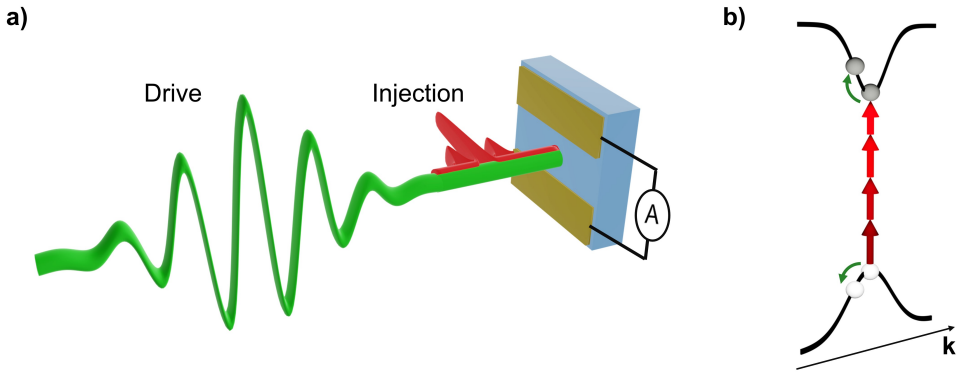

Figure 1.6: NPS detection mechanism. (a) Two beams with orthogonal polarization are collinearly focused on a thin dielectric sample. A short intense pulse is used to nonlinearly inject carriers into the conduction band of the sample (injection) while the pulse we want to reconstruct (drive) is strong enough just to drive a current in two electrodes positioned at two opposite sides of the sample but not to inject carriers. (b) Illustration of the nonlinear process happening on the surface of the sample. The injecting field (red) leaves a hole in the valence band and puts electrons in the conduction band, thus, generating a dipole. The driving pulse (green arrows) subsequently steers the dipole towards the electrodes and a current is detected. The axis k indicates the crystal momentum space.

We can use now this confined electron wavepacket as electrical gating to sample another pulse. By putting two electrodes on the surface of a dielectric it is possible to detect the current driven by the pulse we want to retrieve (drive). To be more precise, what is detected is the dipole generated by the electrons steered towards the electrodes by the driving field. The arrival time of the two pulses can be changed to obtain the full electric field of the driving pulse. The detection scheme just described is called nonlinear photoconductive sampling (NPS) [38, 39] and can sample frequencies down to the UV [40]. Figure 1.6 illustrates the working principle of NPS.

To work efficiently, NPS requires the two beams to be perpendicularly polarized. In particular, the injecting field needs to be parallel to the electrons. In this way, possible contributions to the current due to the injection are minimised. The driving field has to be instead perpendicular to the electrode orientation such that the detected current is maximised. Like in EOS, also for NPS what we detect is a convolution of the gating with our signal. However for NPS, the current does not provide directly the electric field but the vector potential, $A_d(t)$, of the driving field, d:

$$A_d(t) = \int_t^\infty E_d(t')dt' \tag{1.26}$$

From what just said it follows that the signal on the electrodes, $S_d(\tau)$, is given by:

$$S_d(\tau) = -\int_{-\infty}^{\infty} A_d(t)G(t-\tau)dt \tag{1.27}$$

where τ is the relative delay between injection and drive and G is the gating function of the injecting field. Ideally, we want the injecting pulse to be a cosine single-cycle pulse and to be powerful enough that only the most intense peak can inject carriers. If multiple peaks inject, the different electron wavepackets can interfere giving rise to artefacts and a distorted readout. This makes NPS particularly sensitive to the injecting pulse compression.

Compared to EOS, NPS is more complex to operate. This is mainly due to the necessity of having custom made samples and of carefully choosing the intensities of both pulses and the CEP of the injecting pulse before performing the measurements.

Attosecond streaking

The two field-sensitive techniques described above rely on the interaction of light with solids. Gasses can also be used to generate short gating pulses able to sample frequencies in the THz and PHz range. Attosecond streaking is an example of how this can be achieved. Unlike solids, gasses do not have a damage threshold. They can indeed be ionised and immediately replaced by fresh molecules/atoms if a gas jet is employed. This feature allows the use of ultra-intense pulses which electric field is comparable to the binding electron potential. Under the right focusing and phase-matching conditions, extreme UV (XUV) pulses can be emitted from the gas target. The process through which this emission occurs is called high-harmonic generation (HHG) and can be described by a three-step model [41, 42]. At first, the laser ionizes the gas target via tunnelling ionization (see section 1.4), then the free electron is driven by the laser field and, finally, the free electron recombines with the parent ion, emitting an XUV burst that has a pulse duration in the attoseconds (as) time scale [43]. The three steps occur at each half cycle that can ionize the target. The final result is a train of XUV pulses. An XUV spectrometer reveals that this train of pulses presents at low energies a series of peaks at every odd harmonic of the pump laser central frequency and at high energies a plateau, up to a cut-off energy. The first pattern

is due to the interference of different XUV pulses in the spectrometer, while the plateau by the most energetic portion of the most intense burst. The energy cut-off, instead, depends on the laser and atom parameters according to:

$$E_{cut-off} = I_P + 3.17U_P \tag{1.28}$$

where I_P is the atom ionization potential and U_P is the ponderomotive potential acquired by the free electron under the influence of an electric field, E_{pump} [44]. U_P can be expressed as follows:

$$U_P = \frac{e^2 E_{pump}^2 \lambda_0^2}{4mc^2} \tag{1.29}$$

e and m are respectively the electron charge and mass, while λ_0 is the electric field central wavelength. It follows from equation 1.29 that the energy cut-off scales quadratically with λ_0. Lasers with a lower frequencies would therefore shift the $E_{cut-off}$ to higher energies. On the other hand, this would lower the XUV generation efficiency [45].

Different schemes can be used to isolate or generate a single burst [46, 47]. An isolated XUV pulse represents the ideal gating to resolve optical frequencies, being confined to just a few hundreds of as. The detection scheme used in this case is called attosecond streaking. An isolated XUV burst and the test pulse are focused collinearly on a gas target, where the XUV resonantly ionizes the target atoms, bringing one electron in the continuum. The free electron is then driven by the test pulse towards a time of flight (TOF) detector that detects their kinetic energy. The time delay between the test and the XUV pulse can be controlled to sample in the time domain the test electric field. From this detection scheme it follows that, like in NPS, the readout at a given time delay is proportional to the vector potential of the field. The power of attosecond streaking lays in the possibility of reconstructing the isolated XUV pulse. This can be done by correlating the TOF readout with an XUV spectrum obtained by using a spectrometer like demonstrated in [8].

Compared to EOS, attosecond streaking requires a more expensive and complex implementation. Attosecond streaking needs indeed high vacuum and short IR-vis pulses able to generate an XUV burst. EOS can instead work in ambient air and does not require the test pulse to be compressed. However, both techniques require CEP-stable pulses. For attosecond streaking, it is the test pulse that generates the gating pulse. This means that CEP fluctuations on the first reflect as well on the sampling pulse. For EOS, CEP fluctuations of the test pulse do not limit its operation because the two pulses are independent from one another. Furthermore, EOS outperforms attosecond streaking in terms of time required to obtain one electric field trace. This is mainly due to the good sensitivity and dynamic range of EOS. On the other hand, EOS cannot be used to directly extract information about the gating pulse. In this sense, attosecond streaking is superior to EOS. Attosecond is indeed the typical time scale at which electrons orbit around atoms and therefore this technique is ideal to reveal how electrons move under the influence of electric fields [48, 49].

1.4 Non-perturbative regime

HHG is just one example of how electric fields, if powerful enough, do not simply excite a bound electron but can also drive an electron wavepacket away from its parent atom. In this case, the description given in section 1.2 does not hold anymore because equation 1.11 does not converge anymore to a finite value. When a laser field reaches intensities comparable to the electron binding potential, we cannot treat the field simply as a perturbation that affects the optical properties of the medium. This is the reason why we refer to this regime as non-perturbative. The transition from perturbative to the non-perturbative regime can be quantified referring to the so-called Keldysh parameter, γ:

$$\gamma = \frac{\sqrt{2mI_P}\omega}{eE_0} \tag{1.30}$$

where I_P is the ionization potential and E_0 is the external electric field of central frequency ω. Given an electric field, the Keldysh parameter describes whether the ionization occurs via multi-photon absorption or tunnelling. The last process is a quantum effect through which an electron finds itself over a potential barrier, without having enough energy to go over it. Quantum tunnelling can be explained considering that the electron's wave function can have a non-zero probability to find itself on the other side of the barrier. If we express the barrier length as I_P/eE_0 and the electron velocity as $\sqrt{2I_P/m}$, we obtain a time $\tau = \gamma/\omega$, which is the time it takes to the electron to travel through the barrier. This implies that when τ is long the probability of having tunnelling ionization is low. In other terms, if $\gamma >> 1$ the ionization is dominated by multi-photon absorption, instead, if $\gamma << 1$ the dominant process is tunnelling. To understand what happens in between we have to look at how the tunnelling probability depends on I_P and the width of the barrier, Δx:

$$P_{tunnelling} \propto e^{-\sqrt{I_P - E}\Delta x} \tag{1.31}$$

where E is the electron energy. At first, the electron cannot tunnel through the barrier and therefore starts absorbing photons. Once at higher energy, the electron experiences a smaller binding energy and therefore P in 1.31 becomes exponentially higher. The electron can now easily be ejected in the continuum via tunnelling ionization. It is in this overlapping region that most of the intense lasers operate, including the systems shown in this thesis.

One of the most commonly used and accepted model to describe tunnelling ionization is the Ammosov-Delone-Krainov (ADK) theory. The ADK model is based on a modified version of the analytical solution of hydrogen-like atoms The model can also be extended to molecules by taking into account the asymptotic region of the molecular wave function [50].

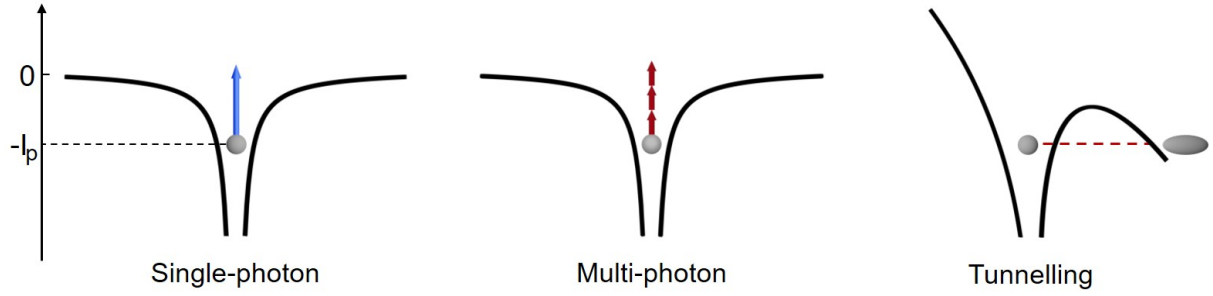

Figure 1.7: Ionization mechanisms. From left to right the intensity of the ionizing field is increased. On the left is shown the process of single-photon ionization. This is the simplest case that occurs when UV radiation is used. This process, being linear with intensity, does not have a power threshold. The second process depicts multi-photon ionization and the third tunnelling.

1.4.1 Laser-plasma interaction

For the pump-probe experiments presented in this work, the target sample is not an isolated atom or a single molecule but a collection of them. The goal of our measurements is to study the emission of molecules/atoms upon ionization without detecting secondary macroscopic effects that have a different origin. When high power lasers are employed, several atoms can be ionized, thus generating a plasma. Briefly, we can define a plasma as a neutral medium made of free electrons and ions that interact with each other electronically. If we imagine to instantly separate by a small amount negative and positive charges, an oscillation is induced. The frequency of this oscillation is called plasma frequency and takes the following form:

$$\omega_p = \sqrt{\frac{N_e e^2}{m_e \epsilon_0}} \tag{1.32}$$

where N_e is the electron density. This allows us to define a plasma refractive index as:

$$n = \sqrt{1 - \frac{\omega_p^2}{\omega^2}} \tag{1.33}$$

where ω is the laser frequency. The equation above tells us that for ω higher than ω_p the plasma is transmissive and for ω lower than ω_p reflective. Because the radiation that we want to detect in this work is in the THz range, the plasma frequency needs to be below this spectral region to allow their detection. The inhomogeneous density profile created in plasma is another factor that affects the propagation of a laser pulse. The Kerr effect can indeed take place above a critical power, resulting in a nonlinear dependence of the intensity in the focus on the incoming power. This effect is also called plasma self-focusing and it scales with the number of free electrons. In our case, by using a low pressure in the

gas jet is possible to avoid plasma self-focusing and at the same time reduce its plasma frequency.

1.5 Atomic systems

1.5.1 Rydberg physics

Most of the information on light-matter interaction is contained in the temporal evolution of the electron wavepacket induced by a radiation. Therefore, to describe how an irradiated atom or molecule evolves, we need an equation that can predict instantaneously the properties of a wavepacket. The time-dependent Schrödinger equation (TDSE), written below, provides this information:

$$i\hbar\frac{\partial}{\partial t}\Psi(x,t) = \Big[-\frac{\hbar^2}{2m}\frac{\partial^2}{\partial x^2} + V(x,t)\Big]\Psi(x,t) \tag{1.34}$$

where Ψ is the particle wave function. The particle kinetic energy is given by the first term on the right-hand side and $V(x,t)$ is instead the potential due to the environment. The sum of the two terms in the right hand side gives the hamiltonian of the system, $\hat{H}$. If $\hat{H}$ is not time dependent we can simplify the equation above to:

$$\hat{H}\,|\Psi\rangle = E\,|\Psi\rangle \tag{1.35}$$

The eigenvalues of this equation (E) give the static energy values of the system. In the case of hydrogen atoms, an exact solution can be easily found. Already for helium atoms, the hamiltonian is described by five terms (two kinetic energy terms for the two electrons, two terms for nuclear-electron interaction and one term for the electron-electron interaction), and requires approximations to be solved. Ideally, we would like to have a hydrogen-like system such that the Schrödinger equation can be applied and its solutions can be used to describe its energy levels. An approximation, called single active electron approximation (SAEP), comes in handy when describing hydrogen-like systems, i.e. an atom in an excited state. These states follow a well known progression: the Rydberg series. For an atom with atomic number Z, the series can be described by the following equation:

$$\frac{1}{\lambda} = \frac{E}{hc} = RZ^2\Big(\frac{1}{n'^2} - \frac{1}{n^2}\Big) \tag{1.36}$$

where R is the Rydberg constant ($\approx 1.097 \cdot 10^7\ m^{-1}$) multiplied by the element reduced mass, n' and n are two principal numbers of the initial and final state, respectively. The equation provides the inverse of the wavelength of the transition between two states. The description given by the Rydberg equation is not limited to atoms but can be extended to any hydrogen-like system, spanning from molecules to excitons [51]. The figure below shows the Rydberg states for hydrogen, atoms with $Z > 1$ and for molecules.

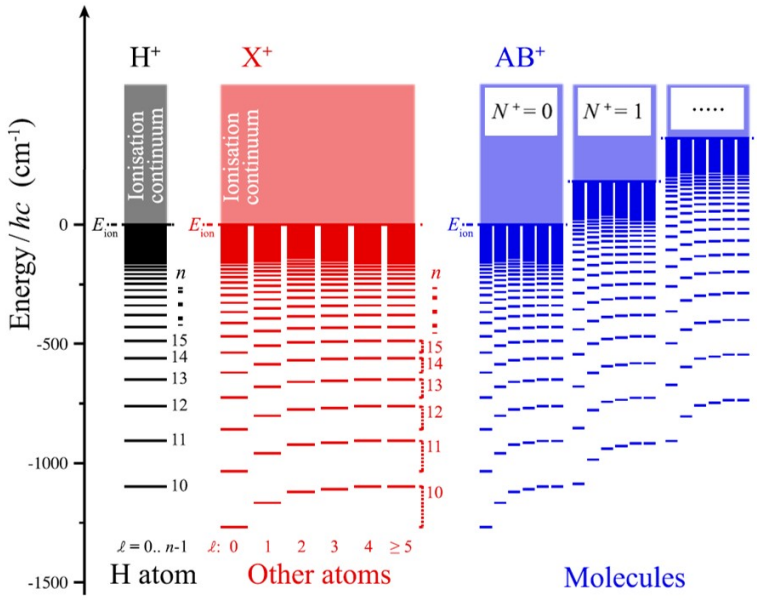

Figure 1.8: Rydberg states of different species. The picture shows how the highly excited states of different atoms and molecules are distributed as a function of their binding energy. It is clear how the states converge for $n \longrightarrow \infty$ to the ionization energy E_{ion} and how for molecules, the states are shifted to higher energies for different quantum numbers. Image edited from [52].

Their similarity demonstrates how Rydberg physics can be applied to different systems. A slight modification of equation 1.36 is required to correctly describe a Rydberg system different from hydrogen. In this case, the Rydberg series is given by:

$$E' = E - \frac{hcR}{(n - \delta_l)^2} \tag{1.37}$$

where δ_l is the quantum defect that depends on the secondary quantum number l. δ_l gives a quantitative value to how far the system is from an ideal hydrogen atom. Above we have only considered the energy levels occupied by an electron under the Coulomb potential of its parent atom. To include the interaction with an external electric field we can act on the $V(x,t)$ term of equation 1.34 and add the following potential:

$$F = -\mu \cdot \mathcal{E} \tag{1.38}$$

where μ is the transition dipole and $\mathcal{E}$ is the external electric field. This factor describes the so-called Stark effect. The potential in equation 1.38 results in a splitting of the energy levels similar to the one of magnetic fields (Zeeman effect). Here, our analysis is limited to the case of DC-fields, indeed, for AC-fields the hamiltonian is time-dependent and the solution becomes more complex. Equation 1.38 is an approximation to the first order of the full light-matter coupling. Nevertheless, this term can well describe how Rydberg states

and Stark shift are connected. If we assign to the dipole moment its maximum value, we obtain the following:

$$\mu_{max} \approx \frac{3}{2} n^2 e a_0 \tag{1.39}$$

where a_0 is the Bohr radius. It is clear how for higher n and therefore for higher Rydberg states the dipole moment becomes extremely sensitive to external electric fields. This feature of Rydberg atoms makes them particularly suitable for several applications like remote sensing, imaging, detection of microwave fields and quantum optics [53, 54, 55].

The dipole moment is not the only quantity that scales nonlinearly with n for Rydberg atoms. Their radius scales as well with n^2 making dipole-dipole interactions between neighbouring atoms scale with the fourth power of n and Van der Waals interactions with the eleventh power of n. The lifetime of highly excited Rydberg states scales as n^3. Highly excited Rydberg states can indeed last on the order of few hundreds of microseconds, making these systems unique and stable at the same time. The long-lasting lifetime means that the ground state and high n orbitals have a small overlap and that the dipole coupling is low. This implies that it is also unlikely to populate these states. To increase the transition dipole the atoms can be dressed by using continuous-wave lasers. This allows reaching states that live up tens of picoseconds [56], thus making Bose-Einstein condensate studies possible on ultracold Rydberg atoms [57]. In some other applications, the Stark effect is instead used to shift the Rydberg states such that they are resonant to a given radiation only when the states are Stark-shifted [58]. In this work is presented a way to control the excited Rydberg states of argon by controlling the shape of a few-cycle electric field. How this goal is achieved is the subject of the next chapter.

In equation 1.38, only the first term of the laser-atom system is taken into account. If we instead stop the Taylor expansion at the second term, we obtain the following equation:

$$F' = -\mu \cdot \mathcal{E} - \frac{1}{2}\alpha \mathcal{E}^2 \tag{1.40}$$

where α is the polarizability of the medium. This quantity gives a measure of how easily an external field polarizes a medium. Equation 1.40 contains both μ and α and is discussed later on when the differences between Raman spectroscopy and IR spectroscopy are explained in section 1.6.1.

1.6 Molecular systems

When we move from atoms to molecules the interactions considered so far become more complex and further approximations are needed. Molecules, on top of electronic transitions, can have vibrational and rotational modes. The nuclear coordinate, therefore, becomes another crucial parameter that affects the energy levels of the system and the interaction with light pulses. We can start our analysis from the TDSE and understand which approximations are required to describe molecular dynamics. The first step is to write down the Hamiltonian of the system. This includes terms deriving from the nuclear,

electronic motion and their mutual correlation. If we take into account that an atom is several orders of magnitude heavier than an electron, we can assume that the electrons move fast enough to experience a static potential given by the frozen position of the atoms in the molecule. This approximation is called the Born–Oppenheimer approximation. For the molecular wavefunction it implies that it can be separated into two independent contributions as follows:

$$\Psi = \chi(R_k)\Phi(r_i, R_k) \tag{1.41}$$

here $\chi(R_k)$ is the nuclear wavefunction at the nuclear position R_k and $\Phi(r_i, R_k)$ is the electronic wavefunction which depends on the position of the electrons r_i for a given R_k. The Born–Oppenheimer approximation implies that two separate dynamics can be derived for electrons and nuclei.

If we consider the case of a diatomic molecule and plug into the TDSE only the nuclear wavefunction, we can write two equations for the radial and angular dependence of χ, respectively, as:

$$\frac{1}{R^2}\frac{d}{dR}\Big(R^2\frac{dS}{dR}\Big) + \frac{2M}{\hbar^2}\Big[E - E_{pot}(R) - \frac{J(J+1)\hbar^2}{2MR^2}\Big]S = 0 \tag{1.42}$$

and

$$\frac{1}{sin\theta}\frac{\partial}{\partial\theta}\Big(sin\theta\frac{\partial Y}{\partial\theta}\Big) + \frac{1}{sin^2\theta}\frac{\partial^2 Y}{\partial\phi^2} + J(J+1)Y = 0 \tag{1.43}$$

where R, θ and ϕ are the spherical coordinates of the wavefunction, 2M is the mass of the nuclei, J is the rotational quantum number, E_{pot} is the electronic potential, which is described below, and S and Y are respectively the radial and the spherical surface harmonic which product gives χ. These two equations describe the vibrations (eq. 1.42) and the rotations (eq. 1.43) of a diatomic molecule. From the last term of eq. 1.42 it follows that we can have both purely vibrational modes (for J =0) and rovibrational modes (for J≠0). The potential where these vibrations take place is usually well approximated by the Morse potential, which has the following expression:

$$E_{pot}(R) = E_B\Big[1 - e^{-a(R-R_e)}\Big]^2 \tag{1.44}$$

where E_B is the binding energy and R_e is the equilibrium position. From this potential is possible to calculate the electronically excited states which are involved in visible/UV laser excitation.

On the same line of Born–Oppenheimer approximation, the Frank-Condon principle allows us to assume that electronic transitions are purely vertical. In other terms, when an electron is excited to a higher electronic state, the transition happens on a time scale that is shorter compared to the nuclear motion. For the two equations 1.42 and 1.44 this implies that R is fixed. The Frank-Condon principle gives us a map of the probability of all allowed transitions. An electronic transition is indeed more likely to happen when, for a given nuclear coordinate, the initial and final wavefunction overlap. We can now apply both approximations to describe the evolution of a wavepacket in a molecule. Let us

assume that upon excitation a molecule is brought to e=2 and v=4 (e = electronic state, v = vibrational state). Because of internal molecular motions, the molecule does not relax directly to its ground state but first undergoes a non-radiative vibrational relaxation (e=2, v=1) followed by a radiative relaxation to an excited vibrational state of e=1 (e=1, v=5). The last step is again a non-radiative vibrational relaxation which brings the molecule back to its ground state (e=1, v=1). The spontaneous emission of radiation between two electronic states is called fluorescence. This radiation is not coherent with the exciting radiation and it is red-shifted compared to the last. The difference in frequency between the absorbed and the emitted frequency is called Stokes shift. The typical time-scale of fluorescence is on the order of nanoseconds. This makes fluorescence a process too slow to study ultrafast internal relaxation dynamics happening in the order of few tens of fs. Nevertheless, fluorescence spectroscopy can be used to study the vibrational landscape of the electronic ground state of biological [59] and non-biological [60] samples and for imaging applications [61]. Fluorescence spectroscopy is just one of the numerous ways to study the energy levels and the dynamics happening in a molecule. This technique does not reveal the plethora of phenomena that characterizes these small building blocks. For example, on a longer time scale, phosphorescence studies inter-system crossings to access single to triplet transitions. Nuclear magnetic resonance spectroscopy is instead used to get an insight into molecular structures. Other techniques, like transient-absorption, time-resolved fluorescence spectroscopy and time-resolved photoemission instead allow for the study of dynamics of both simple and complex systems. Vibrations and molecular rotations can be studied also by other two types of spectroscopy: Raman and IR. These are the topics of the next two sections.

What explained above is used later on in chapter 3 to characterize the radiation emitted by ammonia molecules upon sudden ionization. In the experiments presented here the time scale that can be resolved ranges from tens of femtoseconds to few picoseconds. This interval is the typical time scale of molecular vibrations. Because we want to observe specifically those vibrations induced by ionization, we have to choose a cation that has a binding potential in its ground state. This requirement limits the choice of molecules to those which do not dissociate after a few ps and at the same time present a Stokes shift pronounced enough that several vibrations are involved in the dynamics.

1.6.1 Raman spectroscopy

Molecular dynamics can be tracked if there is an observable that is linked to the dynamic under study. The observable, in the case of spectroscopy, is usually a variation of the emitted, absorbed or scattered radiation. From equation 1.40 it can be inferred that the effect of a field on a molecule can either be on its dipole moment, μ, or its polarizability, α. Therefore, if one of these two quantities changes with time there is a physical quantity that can be used to follow the induced dynamics. The dipole moment μ and the polarizability α are related by the following relation:

$$\mu = \alpha \mathcal{E} \tag{1.45}$$

which tells us that while μ is a vector, α is a tensor. We can now write the Taylor expansion of α as a function of the normal coordinate system relative to the equilibrium position, Q:

$$\alpha = \alpha_0 + \frac{\partial \alpha}{\partial Q} Q + ... \tag{1.46}$$

in this equation the information on the dynamics is in the second term on the right hand side because of the time dependent variations of Q. For an harmonic oscillation of frequency ω_v, the last can be written as:

$$Q = Q_0 cos\omega_v t \tag{1.47}$$

if we now replace the last two equations in 1.45, the induced dipole moment takes the following form:

$$\mu = \alpha_0 E_0 cos(\omega t) + \frac{\partial \alpha}{\partial Q} \frac{Q_0 E_0}{2} [cos(\omega - \omega_v)t + cos(\omega + \omega_v)t] \tag{1.48}$$

where ω is the frequency of the electric field. The first term represents elastic scattering (Rayleigh scattering), the second and third terms are the Stokes and anti-Stokes contributions. The last two terms are the lowest order Raman processes that can drive molecular vibrations or rotations in a molecule. These processes can be either spontaneous or stimulated. In the second case, for Stokes transitions, the process is known as Stimulated Raman Scattering (SRS). All the modes that do not result in a change of polarizability are not Raman active but, as is shown below, IR active, being these two complementary techniques. If instead of a single frequency electric field we send an ultrashort pulse, the normal coordinates (Q) do not take the same form as in equation 1.47. Assuming a transform-limited Gaussian pulse and plugging it into the equation describing SRS, Q can be rewritten as:

$$Q(z > 0, t > 0) = Q_0 e^{-\gamma(t - zn/c)} sin[\omega_0 (t - zn/c)] \tag{1.49}$$

where γ is the damping factor of the oscillation. The process described by equation 1.49 is known as instantaneous SRS (ISRS) [62, 63]. From the equation above it can be derived that ISRS radiation propagates along the electric field propagation direction and it is a coherent process. The main difference between ISRS and SRS is that only the first process contains the information of when the vibrational wavepackets are launched. The factor zn/c indeed is related to the vibrational oscillation through the wavevector k ($k = 2\pi n/c\tau$). This allows for the observation of unique dynamics both in solids and molecules. In a pump-probe experiment, ISRS has an effect on both the imaginary and the real component of the probe. Transient grating configurations allow for example to detect background-free coherent radiation and to probe both components of the refractive index, therefore, providing a full instantaneous response function of the medium. ISRS finds several applications in the study of lattice motion [64], of liquids [65] where both inter and intra-molecular dynamics can be identified. ISRS can also be applied to telecommunication when a train of short pulses is used and to biological materials.

1.6.2 Impulsive excitation and coherent control

From the description given of ISRS emerges how through short pulses it is possible to retrieve information on dynamics following an impulsive process. These ultrafast motions are not limited to Raman active molecules but can occur in all systems that can coherently produce impulsive stimulated scattering processes. Coherent processes on an excited electronic/vibrational level can be not only induced and investigated by coherent radiation but can also be manipulated by acting on the radiation itself. This method consists of mapping the energy levels of a molecule by, for example, looking at its time and frequency-resolved absorption as a function of a laser parameter. The electronic potential surfaces of ICN were among the first ones investigated with this method [66]. Its study revealed the dissociating potential by tuning the wavelength of a probe pulse. The more complex quasi-bond potential of NaI has also been studied with a similar technique, revealing an avoided crossing when impulsively excited [67].

Changes in the shape of an electric field can also be used to manipulate molecular dynamics. Thanks to the coherent control of a system, it is possible to steer chemical reactions, induce bond-breaking or conical intersections. A well-known example of coherent control is the one achieved in iodine (I_2) in [68]. Here three pulses are used to control the outcome. The first pulse (pump) excites the iodine, the second pulse can either interfere constructively or destructively based on the relative delay with the pump. The third pulse induces the molecule to fluoresce. The oscillations observed in the fluorescence yield are proof of the control over the molecular system through electric fields.

The same concept can be extended to reactions where the branching ratio of the end products can be controlled by tuning the electric field shape or the relative arrival time of different pulses. A phase/amplitude mask as the one shown in figure 1.2 can be used in a loop configuration to direct the reaction. Most of the systems do not require a real-time field characterization and rely on a learning algorithm. The starting field is usually a guess which shape is changed iteratively to maximise the branching ratio. This optimization procedure requires thorough theoretical calculations especially when short pulses are used. A broad spectrum indeed triggers broadband wavepackets which can be the result of quantum interfering patterns, often hard to model. On the other hand, the amount of information we can extract from a system is higher for shorter pulses.

Imaging the interaction among different atoms in a molecule via coherent control is the ultimate goal that this branch of femtochemistry aims to reach. The waveform synthesizer presented in chapter 4 is an ideal source for such a goal, being able to generate and control the shape of ultrabroad pulses. As a proof of principle, the pulses are used to inject electrons wavepackets in a solid sample but the platform is flexible for application in liquids and molecules. Another laser system, presented in chapter 2, is instead used to control the final excited state of ammonia molecules in a proof-of-principle experiment that aims at proving the possibility to control excited states of cations by tuning the CEP of the ionizing pulses.

1.6.3 Infrared spectroscopy

A complementary technique to Raman is infrared (IR) spectroscopy. To understand why this is the case, figure 1.9a below depicts both processes together with SRS showing the energy levels involved in the transitions.

The infrared is the natural spectral region of molecular vibrations. For this reason, IR spectroscopy finds immediate applications mainly in biology or, in general, where molecules are free to vibrate. Most of the biological functional groups, indeed, have peculiar vibrational modes that can be used to uniquely identify them. The fingerprinting of samples, both in the gas, liquid and solid-state, is achieved by looking at the linear IR absorption spectrum of a sample.

The law that describes how a spectral component is absorbed, while propagating through a medium, is called the Beer-Lambert law which has the following form:

$$A = -log_{10}\frac{I_0}{I} = \epsilon c l \tag{1.50}$$

where A is the absorbance of the medium, I_0 and I are the incoming and outgoing beam intensities, respectively, ϵ is the molar attenuation coefficient, proportional to the absorption cross-section, c the concentration and l the path length. Based on the application, equation 1.50 can be modified to retrieve the transmission or the reflection at a given frequency.

Another important definition conventionally used in IR spectroscopy, and, in general, in spectroscopy, is the unit of frequency or wavenumber, defined as the inverse of the wavelength. This quantity is measured in cm^{-1} and simplifies the numbers used in the IR spectral region of light.

The possibility of targeting specific molecular vibrations calls for sources able to provide radiation at the desired wavelength and for sensitive detectors able to resolve the different frequencies involved. Table-top sources are usually based on thermal emitters which provide black-body radiation and, therefore, a broad IR spectrum. The sample can be either analysed in reflection or transmission. Usually, reflection is preferred for thick samples while transmission for thin ones. The detectors can be based on thermal sensors or photodiodes. The firsts detect heat, the seconds light intensity, a feature that makes photodiodes more sensitive in a limited spectral range.

IR spectra present usually several lines which can make their identification not trivial. If we consider an ensemble of n atoms, indeed, these have $3n$ degrees of freedom. If these atoms are now bound, like in the case of a molecule, the degrees of freedom are reduced to $3n - 6$. For a relatively small molecule like benzene already 30 spectral features are present in the spectrum. The complexity of the signal, therefore, requires reliable and robust detection schemes. Commercially available systems like Fourier-transform infrared spectroscopy (FTIR) rely on a Michelson interferometer where a Globar emits a broad IR spectrum which is then detected by sensitive pyroelectric detectors. The main limitation of FTIRs are the low brilliance of the light source and the lack of information on the sample dynamics. These limitations are due to the nature of the Globar radiation emission which

lacks coherence. Nevertheless, FTIRs are compact table-top setups that reliably provide information over several spectral octaves.

A source that instead does not suffer from low brilliance is the synchrotron. These sources are often used to perform IR microscopy on biological samples but, unlike FTIR, require large-scale facilities to operate. The source of radiation in this case is provided by the bending of electrons achieved via dipole magnets that steer an electron beam which emits Bremsstrahlung radiation.

A new configuration described in [28] is field resolved spectroscopy (FRS) that combines the benefits of both synchrotrones and FTIRs, relying on highly brilliant sources and a compact table-top setup that produces ultrashort pulses. FRS relies on EOS that provides background-free detection and information about the phase of the molecular signature. In this work we are not directly make use of IR-spectroscopy, nevertheless, an IR source with a novel amplification scheme is presented in chapter 4.

All the techniques presented above deal exclusively with neutral species. Different methods to study cationic states are explained below. The concepts behind the technique discussed in this dissertation are similar to the one of vibrational IR spectroscopy but are adapted to investigate cations. Here, in particular, we analyse relaxation dynamics that follow an impulsive ionization, so no linear absorption of photons is involved in the process. As described below in chapter 2, the ionization process results in the emission of a broad-band THz/far-IR radiation that is linearly absorbed by neutral molecules. In this sense, IR-spectroscopy enters into play in this work.

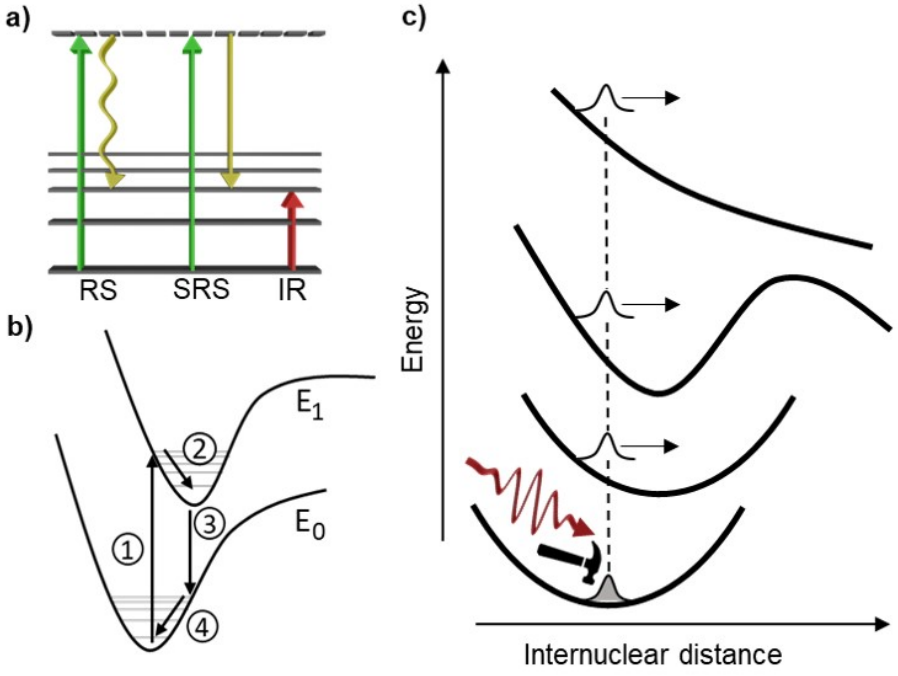

Figure 1.9: Molecular spectroscopy. (a) shows how the real and imaginary state of a molecule are involved in the three different types of spectroscopy described above, namely, spontaneous Raman scattering (RS), stimulated Raman scattering (SRS) and infrared (IR). While IR spectroscopy directly brings the molecule to the desired vibrational energy level, SRS brings first the molecule to a virtual state and a second pulse, which is resonant to a vibrational state, results in the scattering process. (b) shows how an electron wavepacket evolves after is excited by visible radiation. The first step (1) is the vertical excitation that brings the molecule to a high vibrational excited state in E_1. Afterwards (2) the electron relaxes through internal vibrational relaxation (IVR). Once in the E_1 ground state, the molecule can fluoresce (3) and then through IVR reach again the E_0 ground state (4). (c) depicts the process of ISRS. In this case, we are mainly interested in the evolution of the wavepacket in the excited state (2 in b). It is possible to map the excited state of a molecule by probing the wavepacket at different times. In (c) different shapes of potentials show the three types of potential energy curves that the excited state could have.

1.6.4 Photoelectron spectroscopy

When light interacts with a molecule or an atom, not all the electrons have an active role in the interaction. Nevertheless, all together they contribute to an average potential which defines most of the properties of the system. Under a fully quantum point of view, one photon interacts with only one electron that, therefore, can serve as a probe to study the properties of the system to which it belongs. Photoelectron spectroscopy (PES) partly relies

on this concept, taking advantage of the information carried by the kinetic energy of an electron to study the properties of a neutral and ionized atom/molecule before ionization. The basic principle behind PES can be easily understood by recalling the photoelectric effect:

$$E_K = h\nu - E_B \tag{1.51}$$

here E_K is the kinetic energy of the emitted electron, $h\nu$ is the photon energy and E_B is the electron binding energy. The equation above can also be rewritten in a form that includes the initial and final configuration of the system:

$$E(M) + h\nu = E(M^+) + E_K \tag{1.52}$$

where M and M^+ are the neutral and ionic state, respectively. From these two equations, it follows that E_B depends on both the neutral and ionized version of the same molecule. In general, we can say that E_B is equal to the negative of the eigenvalue of the highest occupied molecular orbital (HOMO) obtained via the Hartree-Fock method. This definition of E_B is the one used in the Koopmans' theorem which explanation goes beyond the scope of this work. What should be kept in mind is that the ionization energies are related to the shape of the HOMO and provide information on the structure of molecular orbitals and their dynamics.

In a typical PES experiment what is measured is E_K, what we can control is the photon energy and the information we want to extract is the binding energy. The final readout is therefore a plot showing the electron counts as a function of electron binding energy. Different spectroscopic techniques have been devised based on the frequency of the ionizing radiation. For example, XUV and VUV light is commonly used for solid-state samples. Inner-core electrons are indeed less sensitive to fluctuations of the external environment. They can therefore reveal a material composition and reactions/dynamics happening on the surface of a solid. The emission of electrons can also be resolved along the plane perpendicular to their propagation direction, revealing the band structure of the irradiated sample. This technique is known as ARPES (angular-resolved PES) and can be used to study the unique features of 1D and 2D materials. PES finds many applications as well in molecular physics. Unfortunately, in PES the measurement of electrons kinetic energy suffers from spatial charge effects and noisy readouts that ultimately limit the energy resolution. A standard PES experiment has a resolution of around 40 cm^{-1} which is not enough to resolve rovibrational manifolds. These limitations can be lifted by exploiting the electronically excited energy levels of the molecule. We can indeed first bring the electron in one of these intermediate states and then ionize it. This type of resonant multi-photon ionization (REMPI) requires at least two photons, the first resonant with an excited state and the second able to ionize the excited molecule. REMPI can be performed both using a single-color, (1+1) REMPI, or a two-color beam, (1+1') REMPI. In the second case, the second photon can be tuned to be close to the ionization threshold. Looking back at equation 1.52, it follows that the electron thus freed has a small kinetic energy and in the case the second photon should be resonant to a highly excited Rydberg state, it has zero kinetic energy. It is these specially dressed state that are the starting point of

ZEKE spectroscopy. This technique has mainly two advantages [69]. The first is that the resonance of the excitation process has a high cross-section, thus increasing the number of detectable electrons. A second advantage is that the detection is background free. The ZEKE electrons indeed are still weakly bound to the molecule while all the other electrons which do not contribute to the ZEKE signal are free. It follows that after a given time interval all the free electrons can just be driven away from a static field. Once the free electrons are far from the parent ions, it is possible to ionize the molecules by applying a DC electric field. The sequence just described provides a clean detection which allows improving the resolution up to 0.5 cm^{-1}, one order of magnitude higher compared to conventional PES. As mentioned before one of the properties of these states is to be long-living (lifetime $\propto n^3$), therefore, the waiting time before the DC field ionization does not affect the final readout. Because of their high resolution, ZEKE spectra give access to the rovibrational states of ionic species. As mentioned before, a molecule is not completely ionized until the DC field removes the electron. This means that we can carry spectroscopy of ions without having them repelling each other. Their Coulomb interaction would indeed greatly reduce the signal, resulting in a spectrally broadened signal because of the Doppler effect.

Now we can understand what the ZEKE spectra report. If we look back at figure 1.8 we can see indeed how for different quantum numbers the molecular Rydberg series converge to different ionization energies. The ZEKE spectra therefore plot the intensity associated with those energies and therefore gives an insight on the states of cations.

More information can also be extracted from the same process if we collect ions instead of electrons. This is achieved using a technique is known as Mass Analyzed Threshold Ionization (MATI) [70]. MATI provides insight into the dynamics of clusters and conformers. Nevertheless, ZEKE is more suitable for rovibronic analysis providing a higher spectral resolution for these states. In the framework of this thesis photoelectron spectroscopy results obtained by other groups in previous works via ZEKE serve as a comparison with the measurements presented in chapter 3.

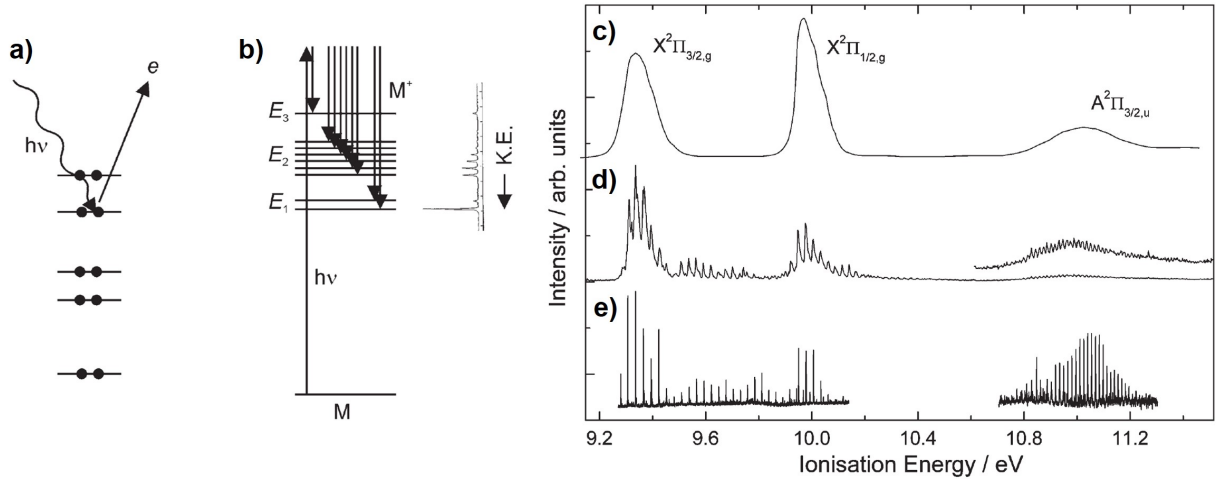

Figure 1.10: Photoelectron spectroscopy principle. (a) is a simplified sketch of the photoelectric effect. A highly energetic photon impinges on an atom and an inner-core electron is ejected after the interaction. The kinetic energy of the last is given by the difference between the photon energy and the Rydberg states of the parent ion. (b) These highly excited states can be accessed via ZEKE spectroscopy which reveals the rovibrational structure of a cation. These states cannot be resolved instead by other types of photoelectron spectroscopic techniques like PES (c) and threshold-PES (d). The panel on the right demonstrates the higher resolution that can be achieved with ZEKE in the case of molecular iodine. One of the reasons for the higher resolution is the way the atoms are ionized. In (c) and (d) the molecules are ionized by a single photon, while in (e) a (1+1') REMPI process is used. Picture edited from [71].

Chapter 2

THz generation in argon and subsequent dynamics

In this chapter an experimental implementation is shown on how to efficiently ionize argon atoms and study the dynamics of highly excited Rydberg states. This chapter aims at reaching two goals: find the optimal conditions to achieve impulsive ionization and second, detect the ensuing emission. As described below, the ionization of an atom or a molecule by an asymmetric pulse results in the emission of terahertz (THz) radiation. In the first part of the chapter the main dependencies of this radiation are characterized and studied to finally obtain THz pulses which spans several octaves. The detection scheme used is electro optic sampling (EOS). EOS allows for a background free detection which gives access to the dynamics of the ionized atoms/molecules. The latter will be the main focus of the second part of this chapter. The superposition of states left after excitation will be described, measured and supported by ab-initio simulations. Unlike other techniques, like ZEKE and, in general, PES, the measurements are based on a fully optical setup which, therefore, does not rely on the detection of electrons and their kinetic energy. This makes the setup easy to implement without requiring any high vacuum equipment. Furthermore, only visible and IR pulses are used for both signal generation and detection.

This chapter serves also as an introduction to the experimental tools and methods used in chapter 3. Here, the analysis is limited to the case of argon. It is demonstrated that the highly excited superposition of states induced after ionization can be detected for this gas as well as for molecular nitrogen.

2.1 THz generation upon ionization

Before the dynamics of ionized species is presented, a review of the ionization process itself is given. In the case of ultrashort pulses, like the ones used in this work, a short transient of current is induced upon ionization. The fast switching on and off of this current results in the emission of an electro-magnetic field in the THz spectral range.

Numerous studies have demonstrated the generation of THz radiation through the

ionization of gaseous media [72, 73, 74]. THz pulses can be produced either in a continuous or a pulsed fashion and can be obtained through different processes like biased antennas [75], optical rectification in crystals [76], two color excitation [77] and broadband few-cycle pulses in both gasses and crystals [78]. Only the generation in gas will be discussed here, since we are interested in molecular/atomic dynamics. As mentioned above, the origin of the THz radiation in this case resides in the varying dipole generated when an electron is spatially separated from its parent ion. The properties of the THz field are therefore related to the temporal evolution of the dipole/current. In the case of an ultrashort pulses ionizing an atom, an electron wavepacket is first injected in a highly-nonlinear fashion in the continuum and then driven by the field. To result in a coherent emission of radiation it is necessary that the ionizing field (pump) is the same for all the ionized atoms. Any slip-off or strong pulse distortion results in the loss of coherence. This phase-matching condition limits the bandwidth of the THz radiation. A second factor that influences the generation of this radiation is the pump symmetry. Let us assume that the pump is a multi-cycle linearly polarized pulse. Once the electron is free, this is steered symmetrically in both directions over the pump duration. The net dipole, therefore, does not have a preferential direction, and the THz radiation cannot build up along the laser propagation direction. We can imagine this configuration as two dipoles with almost opposite phase, the result is a weak THz field.

An asymmetric pump can instead drive the electrons more towards one direction, resulting in the propagation of a THz field along the laser propagation direction. The asymmetric pump does not have to be a few-cycle pulse but can also be obtained by overlapping the fundamental of the pump with its second harmonic (ω+2ω). In this thesis both approaches are presented, giving particular attention to the case of few-cycle pulses.

The goal of this and the next chapter is to study the effects of sudden ionization on atoms and molecules. What we want to detect is in particular the dynamics and the transient molecular fingerprint (TMF) signal following ionization. In the time domain, we can expect to detect first a strong THz signal, due to ionization, followed by the atomic or TMF signature. This type of study requires a time-resolved measurement with the highest possible sensitivity. EOS provides both. This technique is a well affirmed field-sensitive detection scheme for the detection of THz radiation. THz pulses can also be detected using THz field induced second harmonic generation (TFISH) [79]. TFISH has the advantage of having a higher dynamic range if the interaction medium is a gas like in [80]. What limits the detection is the ionization threshold of the gas which is several orders of magnitude higher than the damage threshold of a crystal. TFISH also does not have issues related to the phonon modes. Despite that EOS is easier to implement and the crystal phase-matching can be optimised to the desired frequency, improving the SNR in a given region. Furthermore, by using heterodyne detection, the SNR can be increased significantly, making EOS the ideal detection technique for our purposes.

2.1.1 ω+2ω vs few-cycle ionization

ω+2ω

Laser systems can have different sources of noise, mainly related to thermal drifts and mechanical instabilities. Long term drifts, for example due to thermalization, can be avoided by actively cooling the system. Pulse-to-pulse drifts are instead more complex to tackle and require loop systems that can compensate for them. In an experiment, the SNR is not only defined by the source but also by the detection system used to record a phenomenon. For photon detectors, like the ones used in this thesis, the ultimate noise limit is due to the quantum nature of light. This Poissonan source of noise is called shot noise and its SNR scales with the square root of the number of photons. It has been demonstrated that MHz repetition rate systems in the IR combined with sensitive detection schemes can achieve the shot limit [81].

The main laser parameters that influence the signal generation in our case are the power, the central wavelength and the peak power of the pump pulses. As mentioned above, high-repetition rate systems in the MHz regime have the advantage of greatly reducing the SNR, therefore, improving the detection of weak signals. MHz systems can achieve high power pulse trains up to several tens of watts but, on the other hand, cannot yet produce CEP-stable single cycle pulses [82]. Their peak power is also lower due to the longer pulse duration compared to Ti:Sa based few-kHz laser systems. It follows that to generate asymmetric pulses, MHz laser pulses need to be combined with their second harmonic (ω+2ω). This scheme requires that both the fundamental and its second harmonic are in phase when impinging on the gas sample, such that they sum up constructively and, therefore, generate an asymmetric pulse. Their relative power and polarization are other two parameters that play a role in the ionization efficiency.

The measurements presented in this section are performed using a Ti:Sa oscillator combined with an erbium fiber amplifier. The system, called MEGAS, delivers pulses centered at 1030 nm with a power of 50 W and a repetition rate of 18 MHz (more details can be found in [83]). Figure 2.1a shows how MEGAS pulses are used to generate and detect THz radiation. The 1030 nm pulses are sent through a BBO crystal which generates the second harmonic that ultimately forms asymmetric pulses. The BBO is mounted on a movable stage such that the relative phase between ω and 2ω can be changed to optimise the THz intensity. Once the THz is generated, it propagates together with the pump pulses. To separate them a perforated mirror is used to reflect the THz and transmit the pump pulses. The THz has indeed a wider beam size compared to the pump due to its longer wavelength. The reflected THz pulses are then sampled by the EOS setup used to reconstruct their electric field shapes. The EOS probe pulses are directly picked up after the Ti:Sa oscillator and sent to the EOS setup where the THz pulses are obtained (Figure 2.1b). Their FFT squared (Figure 2.1c) shows that pulses up to 4 THz can be detected.

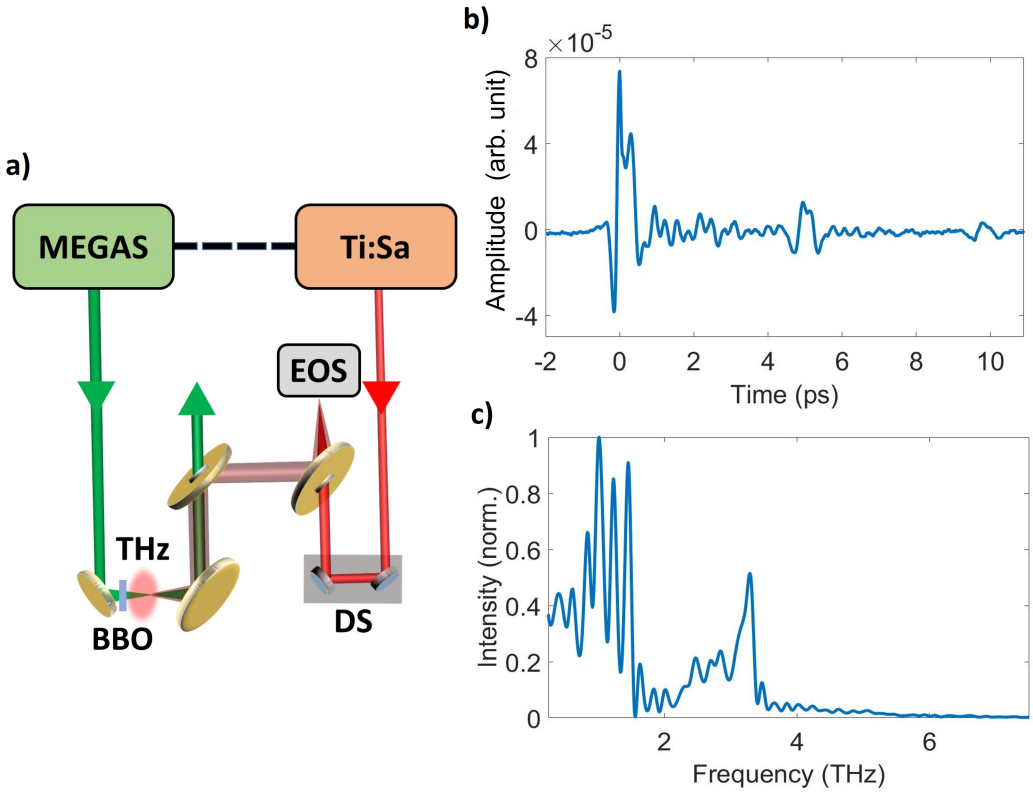

Figure 2.1: THz measurements at MEGAS. 1030 nm pulses are reflected by a 90 degree off-axis parabola that focuses the fundamental and its second harmonic generated via a BBO crystal positioned few centimetres before the focus. The THz pulses and the pump are recollimated by a second parabola. The two beams are then split by a perforated mirror which reflects the outer part of the THz mode. This is then collinearly combined on the EOS crystal (GaP) with pulses directly picked up after the Ti:Sa oscillator (EOS sampling pulse). A delay stage (DS) allows to time-resolve the THz pulses reported in (b). (c) shows the FFT squared of the pulse in (b). Frequencies up to 4 THz have been detected.

The oscillations following the THz pulse (after 1 ps) are due to air absorption and the stronger structures after 5 and 10 ps are internal reflections of the THz pulse in the EOS crystal. Though the SNR, 14 dB, would allow for the resolution of weak signals following ionization, the narrow THz bandwidth means that the gas is not efficiently ionized, despite the tight pump focusing. This is due to the low peak power of the pulses. Furthermore, the damage threshold of the BBO used for SHG limits the achievable degree of asymmetry, decreasing the signal even more.

Few-cycle ionization

A second way to generate asymmetric pulses, other than through ω+2ω, is by using the intrinsic asymmetry of single-cycle pulses. In our case these are produced using the FP3

system by broadening in a hollow core fiber (HCF) amplified Ti:Sa pulses. The setup is sketched in Figure 2.2a. A Ti:Sa oscillator produces pulses at 780 nm with a power of 170 mW. The pulses are then amplified in a CPA that brings the pulses to a power of 4.25 W and the repetition rate down to 4 kHz. After being sent to a grating compressor and a pointing stabilizer, the beams are focused on a 1.5 m long HCF with an inner core diamater of 140 μm filled with 1.6 bar of Ne. After the HCF, the beam goes through a wedge pair used to optimise the pulse's compression. A reflection from the first wedge is sent to an f-2f interferometer which actively corrects through a feedback loop for CEP fluctuations happening after the oscillator which pulses are instead CEP stabilized by a 0-f interferometer. The pulses out of the HCF fiber are finally compressed by a set of CMs down to 4 fs and have a power of 2 W.

The laser pulses are then sent to a second set of CMs, a wedge pair and, finally, to the chamber where the experiments are performed. Before entering in it a reflection from a wedge is recycled and used as EOS probe beam. This is sent to a delay stage and a second wedge pair to control the compression of the probe pulses. Both pump and probe are sent into the experimental chamber through periscopes that set the final polarization state of the beams. The setup inside the chamber is similar to the one described in the previous figure.

The pump pulses are focused using a 6 inch focal length 90 off-axis parabolic mirror. At a given gas pressure this condition allows for a wide area where the atoms can be ionized, therefore, increasing the number of emitters compared to a tight focus at lower peak power, like the one above. The gas used for the generation of THz radiation is emitted by a gas nozzle that limits the interaction region to few hundreds of microns around the focus. Furthermore, the chamber can be pumped down thanks to a vacuum pre-pump, limiting the gas only to the interaction region.

The THz pulses obtained using FP3 are shown in Figure 2.2b. The lack of air and the higher peak power result in a cleaner time trace compared to the one of Figure 2.1 where the internal reflections of the THz pulse in the crystal can be clearly isolated from the main ionization signal at 0 ps. The FFT squared of the trace from -2 to 4 ps is shown in Figure 2.2c. The bandwidth goes well above 50 THz demonstrating the more efficient ionization process. The EOS crystal here is the same GaP crystal used above (GaP <110> = 10x10x0.5 mm). As it will be shown below, the good SNR (26.3 dB) allows for the detection of ultrafast relaxation dynamics in Ar and N_2.

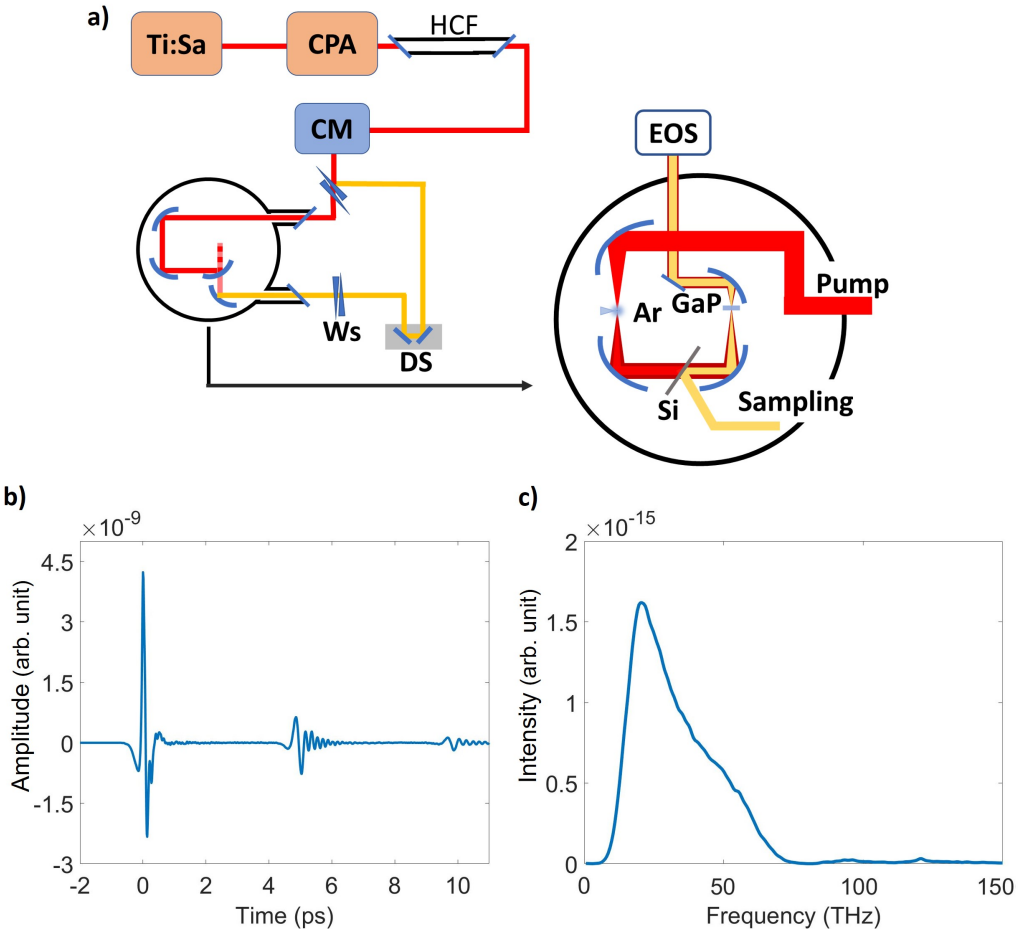

Figure 2.2: THz measurements at the FP3. (a) shows the setup used at the FP3 to carry the experiments on Ar, N_2 and NH_3. Ti:Sa pulses are first amplified in a multipass CPA and then broadened in a HCF filled with Ne. The compression of the pulses is finely tuned by a wedge pair (Ws). One reflection is used as probe and the transmission as pump for the experiment which setup is shown on the right side. The cylindrical chamber used for the experiments allows to carry out experiments in vacuum down to 0.01 mbar with just the use of vacuum pre-pumps. By focusing the beam with a 90◦ parabola (6 inch focal length), the gas sent to the nozzle is ionized and the radiation emitted from it that propagates in the same direction of the pump is recollimated by a second parabola. Being in vacuum, the water absorption in the IR does not interfere with the read out of the measurements, resulting in a clean measurement. To separate the pump and the THz signal, a 1 mm thick float-zone silicon wafer (Si) reflects the former and transmits the latter. The Si wafer also acts as a beam combiner for the probe pulses (sampling) and the THz radiation. The two are then combined in the EOS crystal, in this case GaP. The information of the THz field is contained in the upconverted sampling pulse. It means that vacuum is not required anymore and the beam can be sent out of the chamber. Here the rest of the EOS setup allows for the reconstruction of the THz fields. (b) and (c) show, respectively, a THz trace and its FFT squared for Ar, measured with the same crystal used for the measurements of Figure 2.1.

2.1.2 CEP dependence

Ultrashort pulses that have a bandwidth wider than one octave can reach the single-cycle regime and have a high degree of asymmetry when the CEP is set equal to 0 or π. The system shown in Figure 2.2 delivers pulses as short as 4 fs centered at 780 nm which means that each envelope contains one cycle and half. As mentioned above, the pulses are actively CEP stabilized by a fast and a slow loop that allow for the active control of the CEP. The CEP stability of the system is 0.3 mrad. This provides a good dynamic range over which the CEP can be tuned. To understand how the CEP influences the THz generation we can imagine to set the intensity of the pulses such that only their strongest peak is powerful enough to ionize the gas. For CEP = 0 there is only one peak able to ionize, inducing an asymmetric plasma density. For CEP = $\pi/2$, instead, there are two opposite peaks that will therefore induce a symmetric plasma density. We are describing the laser-gas interaction in terms of plasma density because this is directly related to the varying plasma polarization which is ultimately the source of our THz radiation. In particular, since we are detecting the THz pulses in the far field, the THz in our EOS trace is proportional to the second derivative of the time varying polarization. This quantity, therefore, is directly linked to the total induced plasma charge density.

With our set up is possible to measure how the THz pulses are affected by the pump's symmetry. Figure 2.3 shows the THz radiation recorded at different values of the pump's CEP. Just three traces are shown to simplify the visualization.

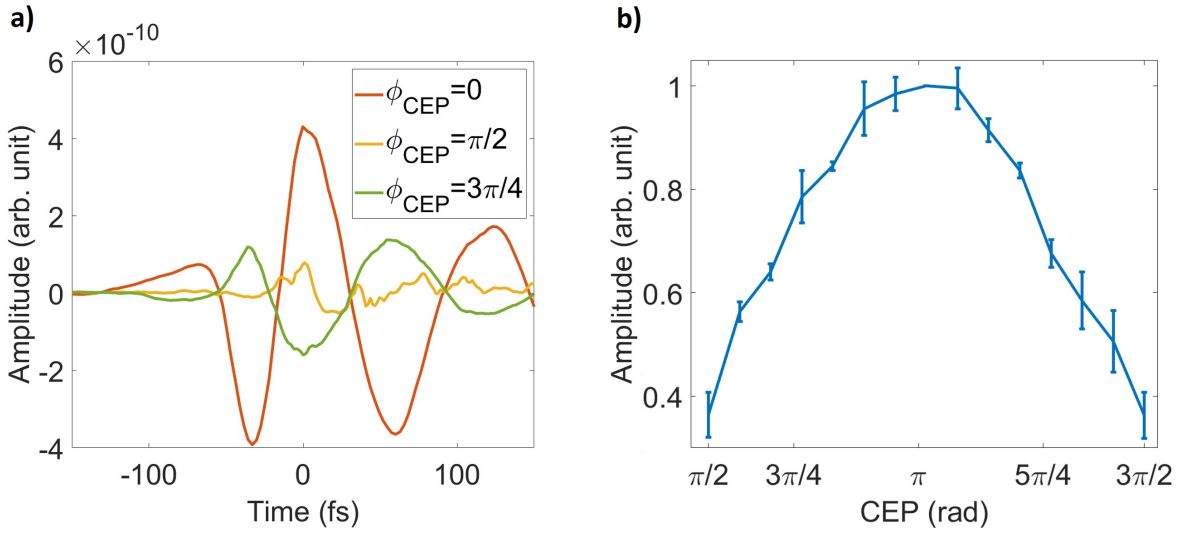

Figure 2.3: THz CEP dependence. The three traces in (a) show how the THz radiation changes for the three different CEP values reported in the legend. A factor of 5 in field amplitude is gained when going from the less to the most asymmetric pump profile. In (b) each point is obtained by calculating the integral of the absolute value of a trace at a given value of the CEP.

The ratio between the peak of the fields shows how the THz and the asymmetry of the ionization can be easily controlled by tuning the CEP of the pump. A ratio of 5 is found in this case for opposite CEP values. The three measurements are shown in Figure 2.3a. The detection crystal used for this measurement is still GaP. To demonstrate that it is possible to finely control the THz intensity Figure 2.3b shows how the intensity of the traces depends on the CEP. The scan is performed from $\pi/2$ to $3\pi/2$. As expected the intensity is symmetric around π, the value for which the pump pulses have the highest asymmetry. The intensity of the THz can in turn be used to retrieve the absolute value of the pump CEP as demonstrated in [78].

2.1.3 Pressure dependence

In the analysis presented so far we have considered the gas as a whole, ignoring the interaction between neighbouring atoms.

The coherence of the process is related to the coherence of the ionized electron wavepacket. This can be lost if the electron impinges on an atom next to the parent ion. In the time domain this causes an echo that is pressure dependent. Another effect related to pressure is the plasma defocusing happening when the electron density is too high. Given that the THz radiation increases with the number of emitters, ideally, we do not observe any saturation effect. Plasma defocusing can act indeed against this proportionality saturating the number of atoms that can be ionized and, consequently, the THz power at a given pump intensity.

We are interested in characterizing the pressure dependence of the THz because later on our measurements are focused on extrapolating information out of intensity scalings. We therefore want to make sure that the detected nonlinearities are solely given by a sum of microscopic events and not by macroscopic effects happening in the plasma. At the same time, we want to work with the highest possible pressure to increase the number of emitters.

To characterize the pressure dependence, different THz traces have been recorded at different pressures. The values reported here are again the integral of the intensity of the THz traces and the pressure is the backing pressure before the gas nozzle. From Figure 2.4 it can be clearly seen the transition to the saturation regime which occurs around 1.5 bar. To make sure that we are far enough from this region, the measurements presented from now on are performed with a backing pressure of 50 mbar.

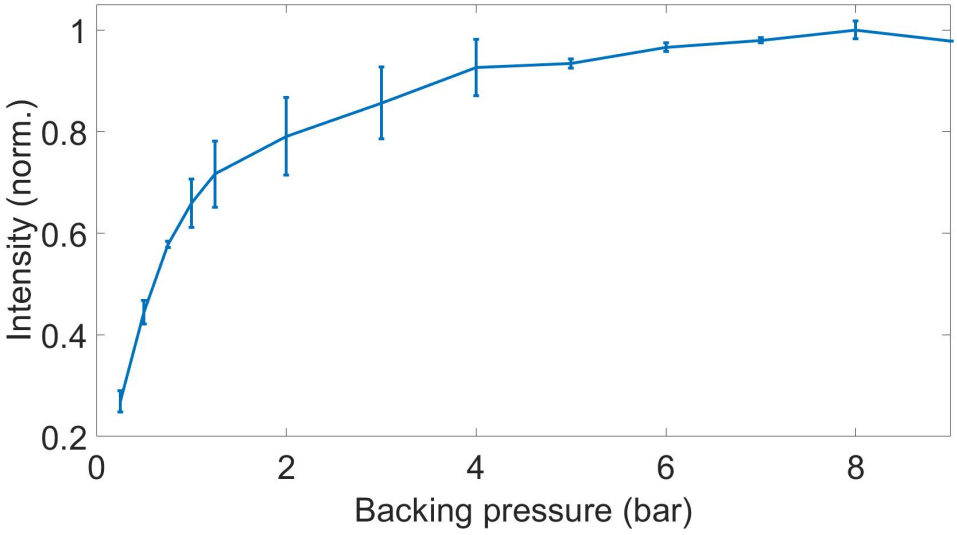

Figure 2.4: THz pressure dependence. The plot shows how the intensity of the THz changes with different backing pressures. Two regions can be identified. A more linear trend, below 2 bar, and a saturation regime, above 2 bar. This last region is reached once the electron density defocuses the beam because of the high electron density, therefore, decreasing the number of ionized atoms.

2.1.4 Intensity dependence

The last dependence that we are going to analyse for Ar is the pump intensity. The way this is done in the setup shown in Figure 2.2 is by placing two wiregrid polarizers and use them in reflection (see setup in Figure 2.5). This preserves the pulse compression and does not affect any other beam parameter, except for the intensity which can be changed by rotating the first wiregrid as shown in the inset below. The option to reduce the intensity by closing an aperture it is not ideal for this experiment. Keeping in mind that the EOS readout depends on the crystal's phase-matching and the THz generation depends on the divergence of the pump, it is necessary to fix the beam size and divergence while performing an intensity scan. Special wiregrids with the wires exposed have been employed for the measurements, thus, keeping at the lowest the amount of glass along the beam path.

If we record the THz intensity and plot it as a function of the pump pulse energies, we expect to see a highly nonlinear trend due to the highly nonlinear intensity dependence of the ionization (blue curve in). Furthermore, at really low intensities we should not be able to ionize and therefore we expect the curves to have an ionization threshold.

The intensity threshold, the lack of saturation and the highly nonlinear dependence can be all identified in the intensity scaling reported in the blue curve of Figure 2.5. For comparison, a second intensity scan at a higher pressure is performed (orange trend in Figure 2.5). The saturation regime due to plasma defocusing and, in general, macroscopic effects clearly emerges. The onset at which the THz intensity starts increasing is different

for the two curves, despite using the same gas. This is most likely due to the self focusing of the pump when the pressure is increased. This results in the shift of the energy threshold towards lower energies. The orange curve in the figure below shows a change in the trend above 300 μJ where the saturation regime starts. On the other hand, the blue curve below does not show any saturation and the highly nonlinear dependence can be clearly observed. The blue trend demonstrates that for this pressure macroscopic effects are not dominating, therefore, indicating that this intensity scaling follows the ionization probability.

Despite being the pump peak power that ultimately determines the ionization efficiency, only the pulse average energy is reported in the intensity scalings. The peak power indeed cannot be accurately measured in the focus.

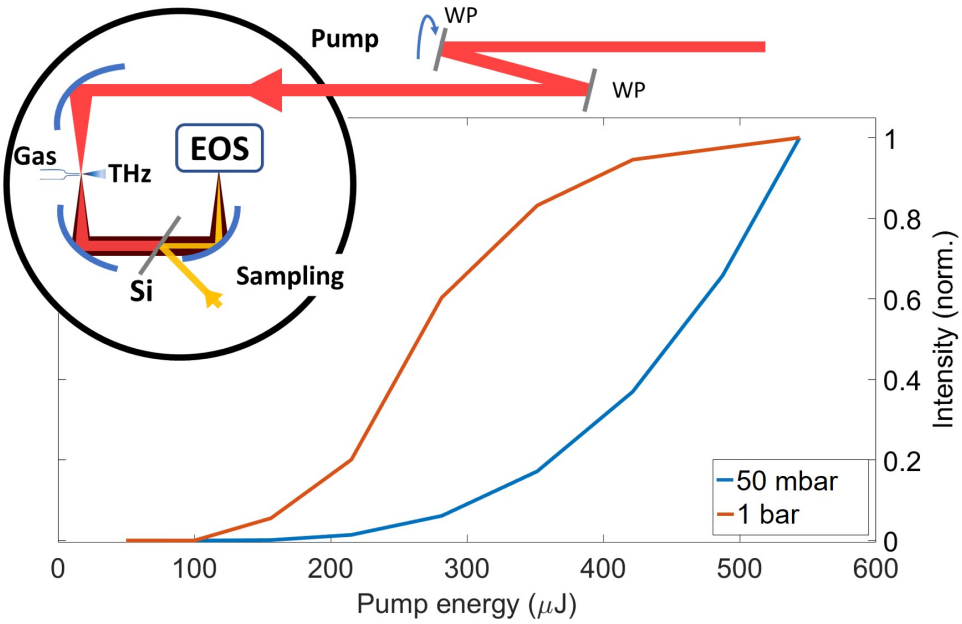

Figure 2.5: THz intensity dependence. The setup shows how the pulse power can be controlled by rotating the first wiregrid polarizer (WP). It is crucial for EOS detection that the polarization of test and sampling pulse are fixed while changing the intensity, being EOS detection polarization dependent. The second WP takes care of it, fixing the polarization after the first WP. The plot reports two trends of the THz intensity recorded as a function of the pump energy for two different pressures. The orange curve shows that the saturation regime is achieved when the intensity is above 300 μJ. The blue curve, recorded at 50 mbar, instead, does not show any sign of saturation. The curves have been normalized to favour their visualization.

2.2 Superposition of highly excited Rydberg states in argon

The capability of characterizing the main scaling behaviours of the THz radiation allows us to follow the dynamics happening in the ionized atoms once the pulse has gone. The evolution of the system can be easily studied in the case of EOS detection by simply applying a time window which selects just the part of the trace after the THz peak. Because of the long central wavelength of the THz pulse, we cannot resolve events which occur a few fs after the THz peak but it is necessary to wait until the THz is weak enough. The time at which we cut the time trace depends not only on the THz itself but also on the crystal used to detect it. In general, the broader the detected bandwidth the faster the detected THz vanishes. In this section, an LGS crystal is used in the EOS setup ($LiGaS_2$, 5x5x0.2 mm, $\theta = 48°$ and ϕ=0). In the case of Ar, the crystal allows for the detection of background free dynamics already after 50 fs.

To emphasize and study dynamics following ionization, it is necessary to get rid of all the contributions that derive from the THz emitted upon ionization. An intensity scaling can potentially reveal if there are dynamics that scale differently from the THz. Through the three steps described in Figure 2.6, it is possible to minimize the root mean square error between each trace and a reference and be left only with signatures that were hidden before by the THz. In general, we can write the recorded EOS signal as given by two contributions: the THz, due to ionization, and the atomic signal. Let us now assume that there are two different functions f and g that describe their intensity dependence (1). If we now optimise the difference between one trace and the others, the f(I)*THz factor can be greatly reduced, being this the dominant contribution (2). The last step (3) is to perform the FFT of the electric field after the THz pulse and obtain the atomic signature.

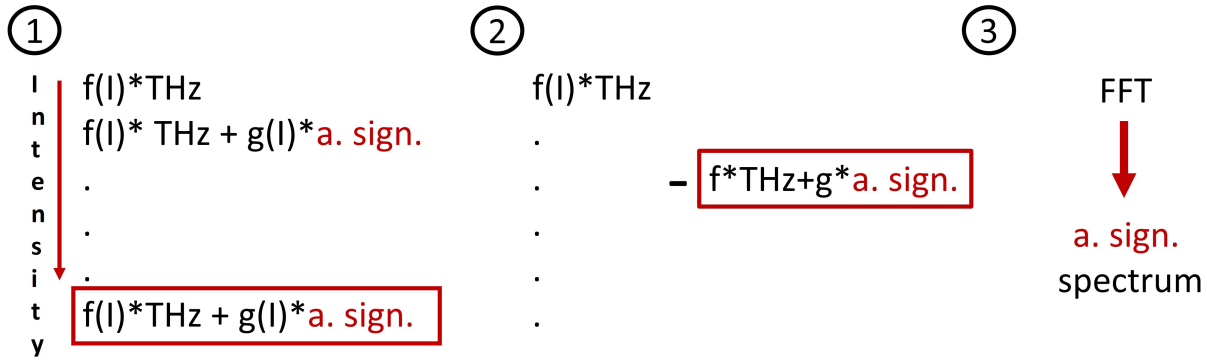

Figure 2.6: Data analysis scheme. The following three steps are performed to reduce the THz contribution from the time traces. f(I) = intensity dependence of the THz signal (THz) g(I) = intensity dependence of the atomic signature (a. sign.)

It is important to notice here that the EOS trace used as reference is the one recorded at the highest intensity. If the less intense one were chosen the worse SNR due to the weaker intensity would reflect in all the traces from which this trace is subtracted, providing misleading results.

Following the three steps above, we can obtain the spectra reported in Figure 2.7b and 2.7c. The data show how the spectrum has distinct features when the window is cut 70 fs after the THz peak. To simplify the visualization only one trace is shown. This is the one obtained by subtracting the trace recorded at the highest intensity from the one recorded at the lowest intensity. The pump power for the two is respectively 500 and 250 μJ.

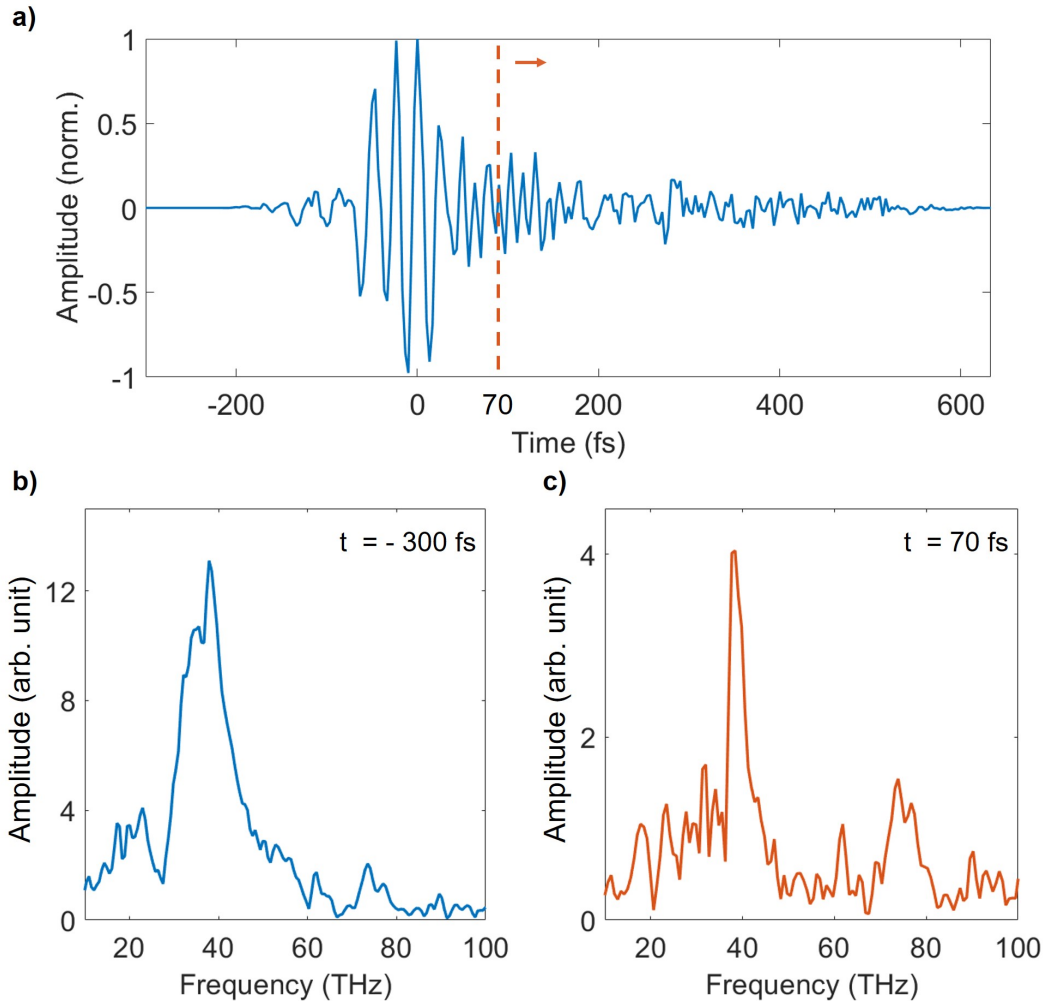

Figure 2.7: FFT of the EOS trace before and after the THz pulse. (a) shows the time domain trace obtained with the procedure shown in Figure 2.6 by subtracting the most and least intense EOS trace. The spectra in (b) and (c) are respectively the FFT of the trace in (a) and of the same trace cut after 70 fs (orange line in (a)).

The THz radiation cannot be completely cancelled out by the data post-processing but weaker frequencies can now more easily resolved.

The time-windowing in Figure 2.7c is not performed by simply setting to zero the field outside the time window but by applying a super-Gaussian filter that avoids sharp edges and, therefore, side bands in the frequency domain.

To assign the spectral components in Figure 2.7c and understand the physics behind this radiation, it is necessary to compare the results above with simulations. Before carrying on with further analysis, it is worth mentioning that if the radiation emitted by the Ar atoms was purely given by the THz emission, this radiation should be temporally confined to few tens of fs. It follows that no sharp spectral components should be present afterwards. What we instead observe in the spectrum of Figure 2.7c are distinct features around 40, 60 and 75 THz.

To verify that these spectral features are not just an artefact due to phase-matching in the EOS crystal, a new set of measurements (intensity scaling) is recorded with a different phase-matching angle. The curves below show again the difference between the most and least intense EOS trace.

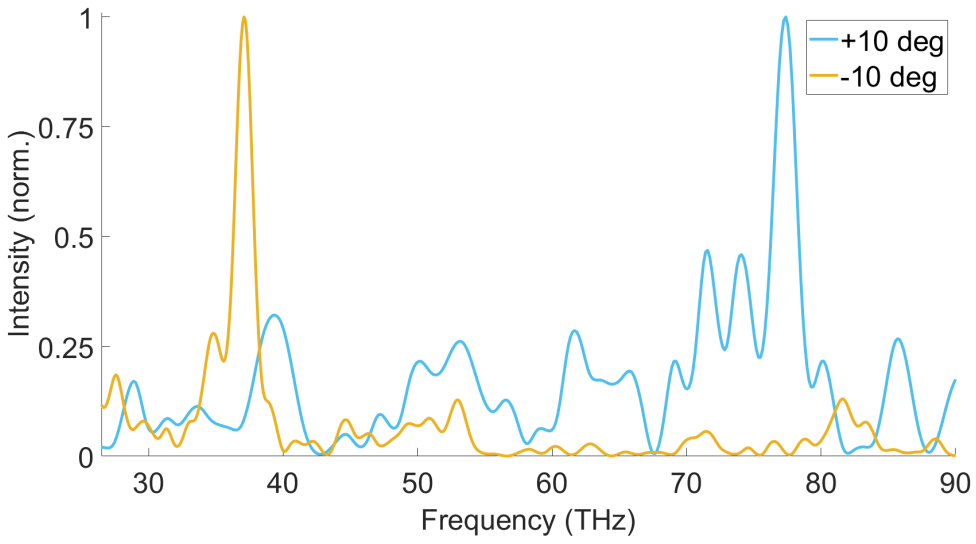

Figure 2.8: FFT squared of EOS trace for two different phase-matching angles. The yellow spectrum is obtained for optimal phase-matching and the blue spectrum by tilting the EOS crystal by 10∘ from the ideal position.

The two spectra show how for a different angle the phase-matching can be shifted more to the red or the blue part of the spectrum. Nevertheless, in both cases the spectral features which have been emphasized before can be detected. Tilting the crystal has the effect of reducing the phase-matching bandwidth and, therefore, to stretch in time the contribution from the THz in the EOS trace. To reduce the contribution of the THz the spectrum was obtained cutting the time trace after 100 fs.

2.2.1 TDSE simulations

The results just presented are now compared to ab-initio simulations performed by Dr Nicholas Karpowicz. The simulated spectra are obtained assuming that 4 fs pulses centered at 780 nm, like the ones used in these experiments, interact with a single Ar atom. Figure 2.10 shows six frames of the temporal evolution of the electron wavepacket density. Before the pump arrival, the wavepacket is localized around the atom. When the pulse arrives, the wavepacket is driven by the field and is spatially dispersed and distorted. Once the pulse is gone, the system still has a net dipole and momentum that results in the emission of radiation. The total dipole is given by the superposition of states in which the atom is left after the interaction with the pump.

From the point of view of the electron wavepacket what happens can be summarised as follows: first, the wavepacket is at rest, then, the laser pump heavily distorts the atomic potential bringing the wavepacket in a superposition of states which oscillates according to the excited states. The oscillations of the superposition can be observed in the last two frames (e) and (f). Part of the wavepacket leaves the field of view being driven away by the field in the continuum.

A purely multiphoton process cannot explain the observed spectrum. This type of interaction would result in the excitation of the electron in a single excited state. The multiple lines in the spectrum confirm that this is not the case. The process described above instead can be explained in terms of frustrated tunnelling ionization (FTI). FTI is a non-radiative process through which atoms can be excited. Their detection usually requires the use of multi-channel detectors able to assign, from the energy of the atoms, the Rydberg state in which the electron is located. From experiments carried out in He, it is possible to learn about the distribution of Rydberg states after FTI occurs [84]. As mentioned in chapter 1, the long lifetime of Rydberg states is due to the low dipole coupling with lower states, making them difficult to be reached. Through FTI is possible, on the other hand, to have a unique ensemble of states that can be generated only by giving energy to the electron wavepacket in the potential given by the combination of an electric field and the atomic Coulomb potential. Having the control over the former means that we can control the final atomic state. Furthermore, in this experiment the detected quantity is an electric field which is less challenging to detect compared to electrons or excited atoms and contains more information of the final states, i.e. their relative phase.

The output of the simulations provides the spectrum at which the atom radiates. This is reported in Figure 2.9. Before comparing the simulated and the measured spectra, it is possible to assign the spectral features to transitions based on the Rydberg equation 1.36.

We expect to not directly detect the energy associated to a Rydberg state but rather a beating between two of them. Because the detection bandwidth is limited from 30 to roughly 80 THz the simulations are limited to this spectral region. The possible states for which the beating occurs between the detection limits are plotted in Figure 2.9 above the spectra. Though there are several transitions, we can exclude some of them by looking at previous experimental observations. In [84], it is demonstrated that most of the atoms are left in a Rydberg state with n = 4 after FTI. This means that most likely Rydberg states around n=13 or 12 do not play a major role. Nevertheless, further simulations and observations would be required to uniquely identify the transitions involved in the process.

The simulations are carried out under the single active electron approximation (SAE). The total potential of the Ar is therefore reduced to an hydrogen-like atom. While greatly simplifying the calculations, this approximation does not work efficiently for s-orbitals where the electron wavefunction has a non-zero probability to be in the center of the atom. For these orbitals the electronic configuration of the atom affects the solutions and, therefore, it cannot be correctly simulated. The disagreement between the calculated and simulated spectra is clear from the missing components in the spectrum where there should be instead a beating.

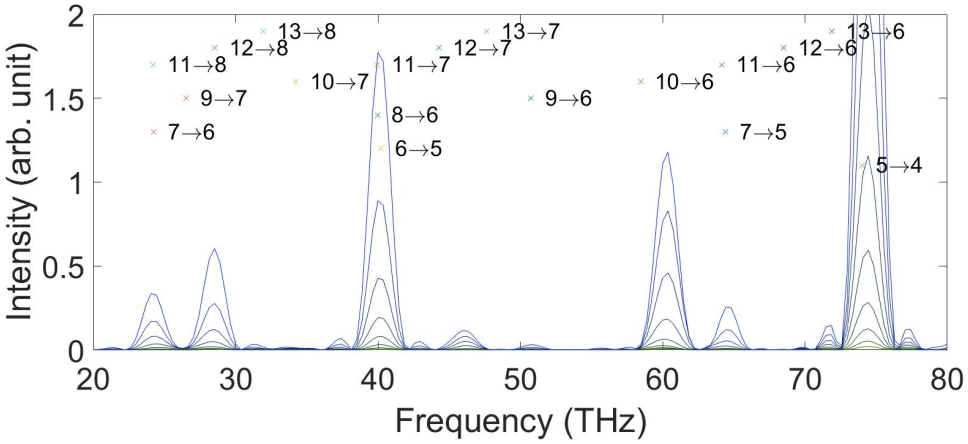

Figure 2.9: Simulated spectra for Ar. The continuous lines show the emission spectrum of Ar after being excited by laser pulses at 780 nm. The different lines represent the spectrum at different pulse energies (most intense in blue, less intense in green). The crosses and the numbers next to them indicate the frequency at which two Rydberg states, given by the correspondent label, beat.

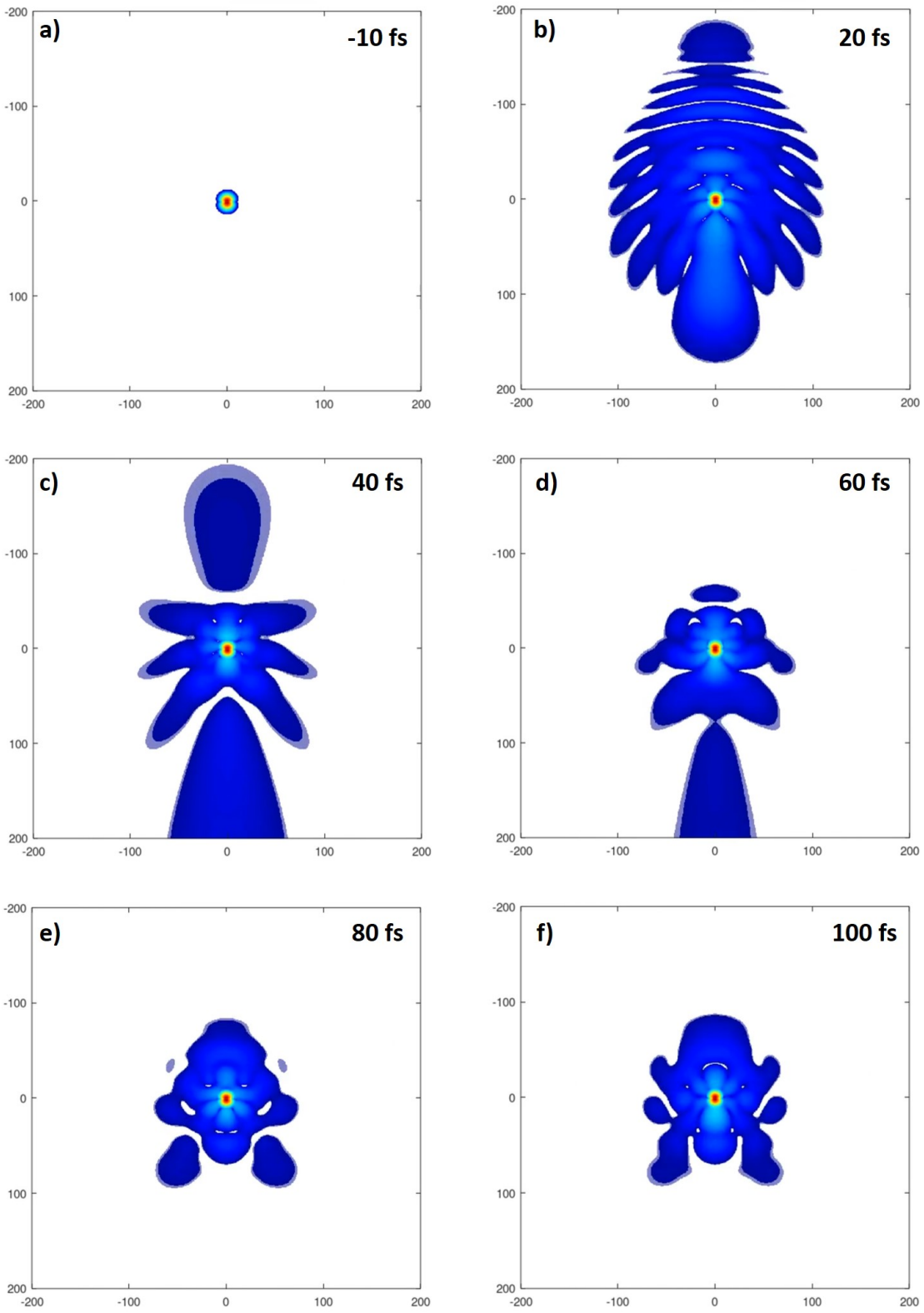

Figure 2.10: Wavepacket evolution of Ar after impulsive excitation. From (a) to (e) the spatial distribution is shown, in atomic units. The time on the top right of each frame is relative to the arrival time of the pump.

2.2.2 Comparison between measurements and simulations

The simulated spectra can now be compared with the measurements shown in the previous section. The plots in Figure 2.11 demonstrates the high degree of overlap between the two spectra. The $5 \rightarrow 4$ transition at 75 THz has been detected in both settings and can be identified as one of the superpositions present in the system. The feature around 62 THz, up-shifted by 2 THz compared to simulations, can be assigned either to the $11 \rightarrow 6$ or to the $7 \rightarrow 5$ transition. Finally, the spectral feature at 37 THz, which also presents a sideband at 40 THz, can be due to one of the following three transitions: $11 \rightarrow 7$, $8 \rightarrow 6$, $6 \rightarrow 5$. Based on the results reported in [84] and given that the transition at 75 THz is probably due to $5 \rightarrow 4$ transition, it is tempting to state that at 40 THz the emission is due to $6 \rightarrow 5$.

Despite the long lifetime of high Rydberg states we can detect their beating only until they have a constant phase-relationship with the neighbouring atoms. EOS, indeed, being a field sensitive detection can only detect coherent events. The coherence of the beating can easily be lost because of atom-atom interaction which can be reduced by decreasing pressure, resulting, on the other hand, in a lower SNR due to the lower number of emitters. The loss of coherence ultimately limits the spectral resolution of our detection system, making the unambiguous identification of the lines not straigthforward.

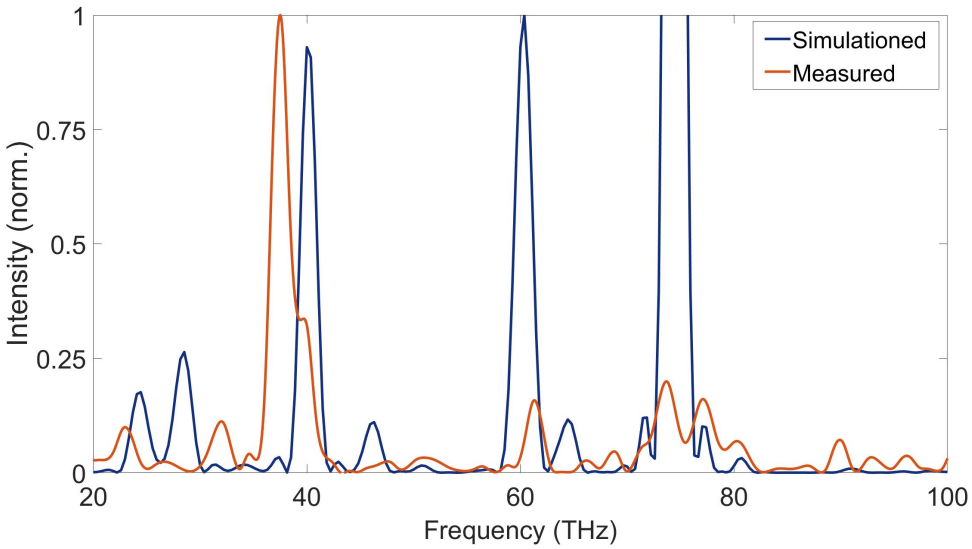

Figure 2.11: Comparison between measured and simulated spectrum. The main three features of the simulated spectrum (dark blue line) are all present in the measured spectra (orange line), though with different relative intensities. The peak at 75 THz, which has twice the intensity of the peak at 60 THz, is not fully shown to better display weaker spectral features.

2.2.3 IR emission of Ar and molecular nitrogen

To verify that the detected emission spectrum described above are distinctive of Ar, molecular nitrogen, N_2, is used in the chamber. The main difference between the two gasses is that N_2 posses rotational and vibrational degrees of freedom while Ar does not. Nevertheless, the choice of N_2 is motivated by the similar ionization potential of the two gasses, 15.6 eV for N_2 and 15.8 eV for Ar. This implies that the THz generation occurs in the same way for both. Referring back to the scheme shown in Figure 2.6, this means keeping f(I) the same while changing g(I).

It is important to mention that both gasses are IR inactive. Argon, indeed, cannot absorb IR radiation in its ground state and N_2 is just Raman active, being a diatomic molecule. No THz absorption is therefore present for these two gasses and the IR emission can only occur in the focus. This greatly simplifies the analysis of the spectra. Nevertheless, the vibrational manifolds results in a spectrum with more features as demonstrates the green spectrum below. The series of lines can be associated with internal vibrations. The molecular structure clearly influences the coherence between the excited Rydberg states. The absence of the peak at 40 THz and the stronger feature at 75 THz confirms how different dynamics are involved.

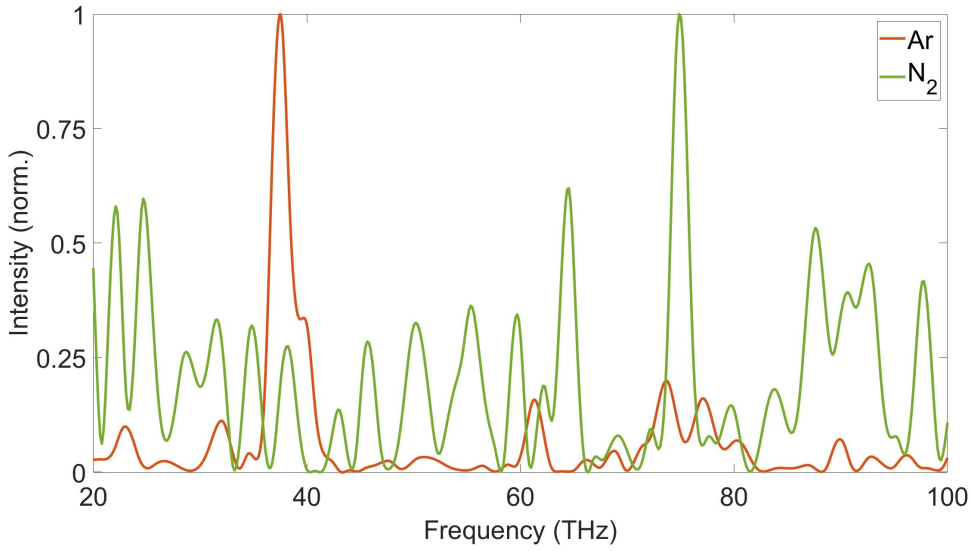

Figure 2.12: Ar vs N_2 spectra. The orange line reports the same spectrum as the one shown in Figure 2.11. The green spectrum is the one obtained for N_2.

2.3 Concluding remarks

In this chapter the ionization and excitation of Ar atoms has been studied in the impulsive limit. Two systems have been compared to increase the percentage of atoms ionized asymmetrically by an ultrashort laser pump. The results presented here demonstrate that 4 fs pulses with a power of 2 W can be used to generate THz pulses up to 100 THz, proving the high degree of asymmetry of the interaction. The main dependencies of the THz radiation from the pump pulses have been studied. This analysis showed that it is possible to access the absolute CEP of the pump pulses, that saturation effects can be avoided by decreasing the density of atoms in the focus. Macroscopic phenomena like phase-matching can be thus avoided by reducing the backing pressure.

When combined with EOS detection, the system presented here gives access to highly-excited Rydberg state dynamics that, for the first time to the author knowledge, have been field-resolved. The data have been collected by comparing time scans at different intensities. This allowed the detection of weaker spectral components hidden below the ionization signal. Compared to the techniques presented in the theoretical chapter, this method allows to directly detect the beating of highly excited Rydberg states without looking at ions or electrons but directly detecting the emitted radiation.

TDSE simulations of the system revealed that the beating of these states results indeed in an in the THz spectral range. A quick comparison with molecular nitrogen showed the complexity of the spectrum that vibrations introduce. Another molecule, NH_3, will be instead the focus of the next chapter.

Chapter 3

Transient molecular fingerprinting of ammonia

In the previous chapter, the analysis was mainly focused on an atomic system, argon. Now the case of a more complex system, ammonia (NH_3), is studied in the context of sudden ionization, achieved using almost single-cycle pulses.

The focus of this chapter is to detect dynamics and identify the emission of ionized molecules. The detection is performed again with EOS with the same setup described in chapter 2. The high dynamic range and SNR of EOS allows for the direct detection of weak electric fields that cannot be resolved by conventional time-resolved spectroscopy. Besides providing background-free measurements, EOS gives access to the information encoded in the phase of a field. This information is used here to improve the SNR.

The spectroscopy of ions is usually performed detecting either ions or almost free electrons via photoelectron spectroscopy (see chapter 1). In this chapter, a proof of principle experiment is demonstrated of how a simple scheme can be used to access the spectra of ammonia cations. The specific vibrations under study are the umbrella modes of both neutral and cationic ammonia.

Within this chapter, the main features of ammonia are introduced and is justified why this is the molecule of choice. In the second section is described the optimization procedure that lead us to directly detect the field emitted by the ammonia cations. In the third section, the data analysis is shown and the results are compared to data from the literature. The main dependencies on the pump parameters are also presented, showing how the detected features can be observed only in a small region of the parameters space.

3.1 Ammonia: Symmetry and vibrational modes

In its ground state, ammonia has the following electronic configuration: $(1a_1)^2(2a_1)^2(1e)^2(3a_1)^2$ (see NH_3 molecular orbital schematic in Figure 3.1a). Because of the nitrogen lone pair, $(3a_1)^2$, that pushes the three hydrogen atoms, ammonia does not have a planar configuration in its ground state. Its geometry falls into the C_{3v} symmetry group, which means that

the molecule has a three-fold rotational axis and three planes of symmetry. This electronic configuration results in a molecule that has two energetically degenerate geometries. Indeed, in the absence of an external field, there is no preferential side in which the nitrogen can be found relative to the plane described by the three hydrogen atoms.

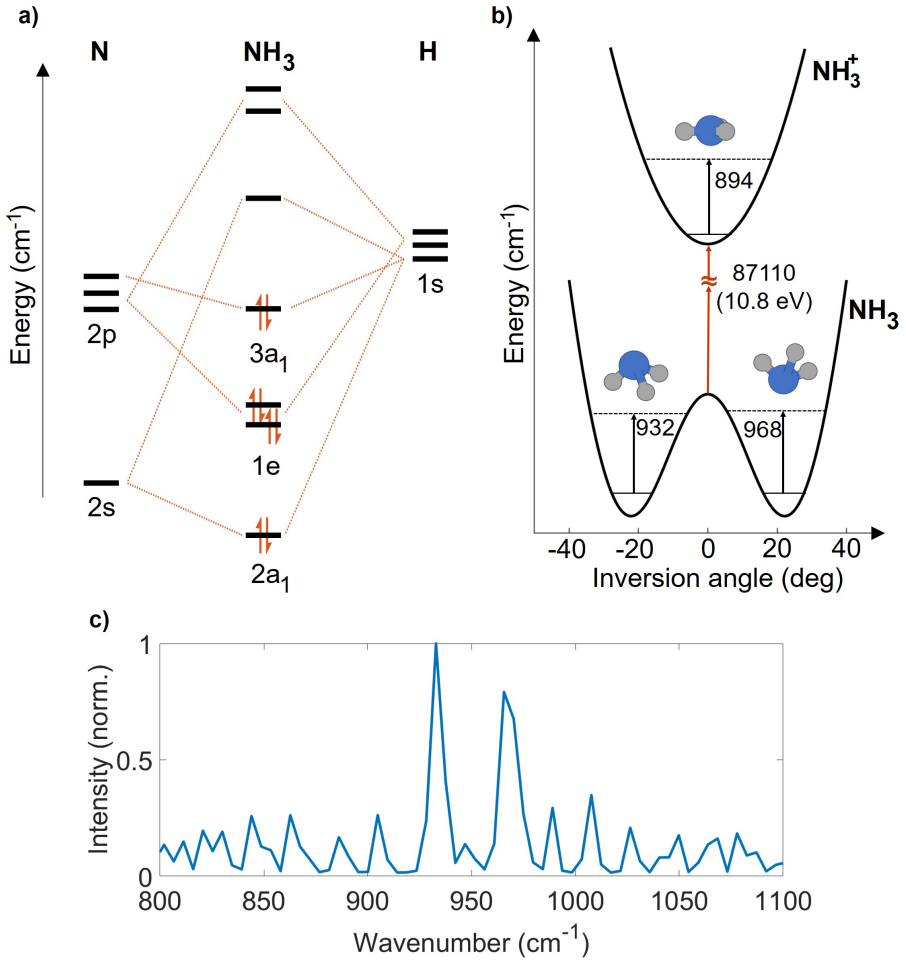

Figure 3.1: Molecular orbital, PEC and absorbance of neutral ammonia. In (a) is reported a schematic of the molecular orbital diagram of NH_3. The highest occupied molecular orbital (HOMO) is the $3a_1$ state. The two electrons in the HOMO are also called lone-pair, because they are not mixed with the orbitals of the three hydrogen atoms. (b) shows the PECs as a function of the inversion angle for neutral and ionised ammonia (NH_3^+). The black vertical lines indicate the transition from the ground state (solid line) to the first excited ground state (dashed line), both with C_{3v} symmetry. The PEC of NH_3^+ has instead a single well potential and a planar geometry. (c) shows the absorbance of NH_3 (data from Hitran database [85]).

Because of this degeneracy, the potential energy curve of ammonia presents a double-well potential energy curve (PEC). The PEC of ammonia is shown in Figure 3.1b. This

displays how the energy changes as a function of the inversion angle, that is the angle between the plane of the H atoms and a N-H bond. Looking at the PEC, the degeneracy of the system can be described in terms of tunnelling of the nitrogen through the plane of the hydrogen atoms. At ambient temperature, the system has already enough energy to allow for the tunnelling to occur. This motion is also referred to as *umbrella mode*. The double well potential of ammonia implies that the symmetric and an asymmetric vibrational eigenfunctions are closely spaced. In turn, this leads to two slightly different energies for the third and fourth vibrational level, 932 cm^{-1} and 968 cm^{-1}. The analysis here is focused on this vibrational modes and, therefore, our EOS system is optimised for their detection.

The goal of the measurements presented here is to detect radiation emitted from NH_3^+. The PECs in Figure 3.1b show that the double-well potential is reduced to a single well for the cations. It follows that ammonia cations are planar (D_{3h}), unlike neutral ammonia. Here, because of the lack of a potential barrier, there is no energy splitting as for NH_3 for the umbrella modes. The IR absorption spectrum of neutral ammonia, shown in Figure 3.1c, displays indeed a spacing of 36 cm^{-1} between the two strongest feature. The neutral spectrum of ammonia has been measured and carefully characterised for hot [86] and ambient-temperature ammonia in both its excited [87] and ground electronic state [88, 89].

What we want to characterise is the spectrum of ammonia cations. Their umbrella modes are expected to be centered around 894 cm^{-1}. This value has been obtained by Edvardsson et al. in [90] through ZEKE measurements and theoretically predicted by Woywod et al. in [91].

This clarifies why ammonia is an ideal case of study for this work. An impulsive ionizing event indeed would result in the reshaping of the molecule and in a sudden geometrical reorganization following the removal of an electron from the HOMO. It follows that the Stokes shift is also pronounced for vertical ionizations and a vibrational wavepacket can be easily excited in the cations. These features of ammonia and, specifically, of the umbrella modes have motivated several groups to study them both using photoelectron [92, 93, 94] and HHG [95] spectroscopy.

Another advantage of impulsively ionizing is that no intermediate excited electronic state comes into play before ionization, as demonstrated in [96]. This leads to a direct transition from the ground state of the neutral to the excited ammonia cation. An energy of 10.8 eV is required to ionize ammonia from the HOMO which, in a multiphoton picture, at 780 nm (1.6 eV) means seven photons. In our case, the pump has a pulse duration of 4 fs. For a cosine pulse, the ionization occurs in less than one fs, therefore, the molecule is frozen during ionization. It is important to notice at this point that ammonia cations have in their first excited vibrational state a binding potential, therefore, the molecule does not dissociate once ionized, thus allowing for ps-long scans.

3.2 Experimental settings and EOS detection

The same setup described in the previous chapter in Figure 2.2 is used here to perform the measurements presented below.

Being IR active, ammonia introduces a higher degree of complexity compared to argon or molecular nitrogen. The THz emitted during ionization can, therefore, be absorbed by the neutral molecules in the chamber [97]. To avoid it we would like to confine ammonia molecules only around the gas nozzle. Despite implementing a catcher and reducing the backing pressure, the experimental setup could not achieve background pressures below a few 10^{-2} mbar when the gas flow was on, resulting in a still detectable background absorption. It follows that there are three sources of radiation that fall into the EOS detection spectrum used in this experiment:

1. Transient molecular emission due to molecular dynamics (TMF)
2. THz radiation following ionization
3. Linear THz absorption due to residual neutral molecules in the chamber

The total EOS signal is, therefore, given by the sum of these three contributions.

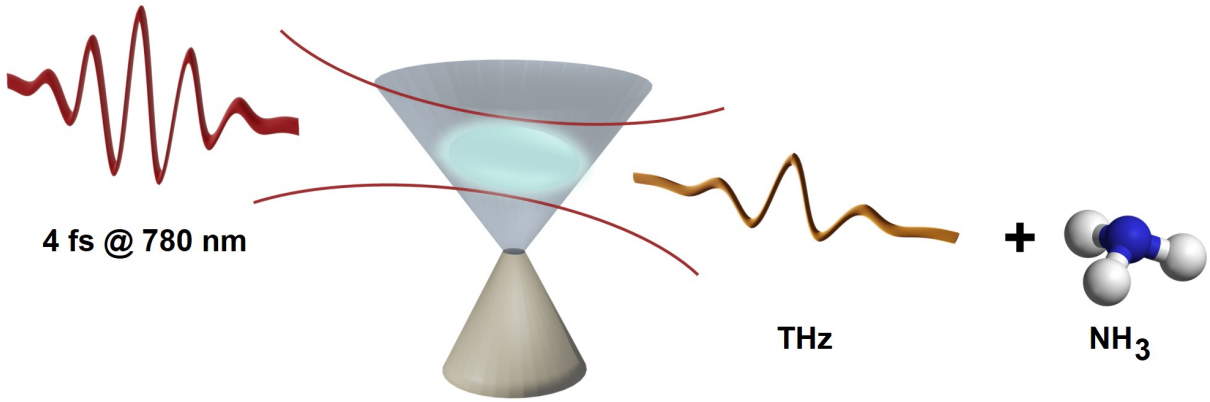

Figure 3.2: Schematic of signal source. 4 fs pump pulses at 780 nm are focused on a gas jet emitted by a nozzle with an aperture of 50 μm. The pulses impulsively ionize the ammonia molecules coming out from the nozzle. The ionization results in the build-up of THz generation that, in turn, linearly excites the molecules of ammonia out of focus.

The experimental procedure followed here is the same one as in the previous chapter. First, different crystals are tested to optimally detect the ammonia umbrella modes, then a backing pressure that does not generate a dense plasma is set and, finally, an intensity scaling is performed to emphasize the spectral features over the background.

The easiest test that we can perform to verify if a signal from ammonia molecules can be detected is to record the THz emitted upon ionization. To perform this measurement a backing pressure of 0.5 bar is used. The crystal employed in this case is GaP (same as in 2.1.1). The EOS trace recorded and its FFT squared are shown in Figure 3.3a and 3.3b.

A quick comparison with Figure 2.2 obtained for argon shows how the two revivals at 1.8 ps and 3.6 ps are absent in the time trace of argon. The feature at 5 ps is due to the internal reflection of the THz signal in the EOS crystal.

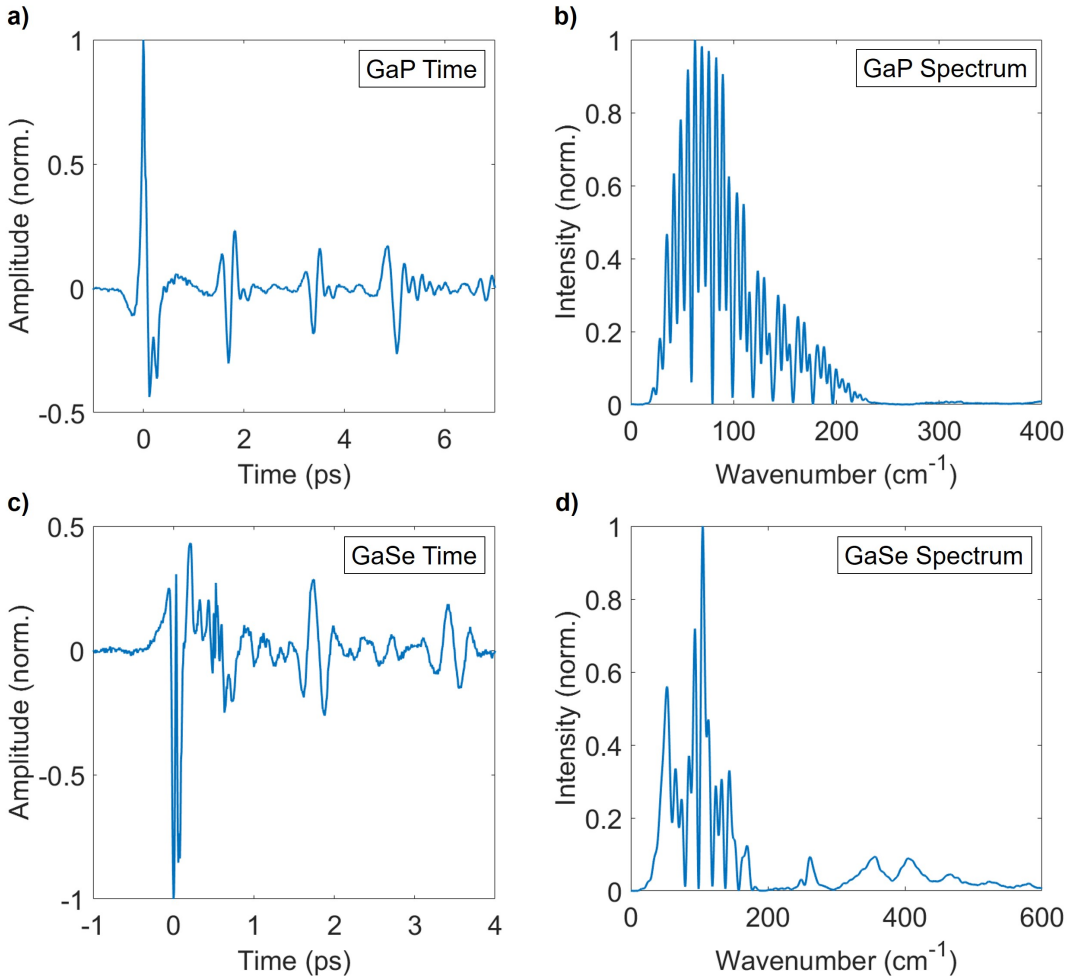

Figure 3.3: Time traces for different EOS crystals. (a) and (b) show the time trace and its FFT squared obtained when using GaP as EOS crystal. (c) and (d) show the same quantities in (a) and (b) but for GaSe. The higher frequencies resolved here derive from the leakage of the pump pulses through the Si wafer.

The two revivals seem to be induced by rotational dynamics but are actually due to the beating of the two strongest vibrations (see Fig. 3.1c). Their spacing is 36 cm^{-1} which corresponds to a beating with a period of 1.85 ps.

In Figure 3.3c and 3.3d the signal is detected using GaSe (Z-cut, 5x5x0.2 mm). The phase-matching is tuned such that higher wavenumbers can be detected to field-resolve the umbrella modes. As shown in the spectrum of Figure 3.3d, the low frequency components constitute still the main contribution. Furthermore, the broad phase-matching has the effect of detecting the 1000 nm part of the pump spectrum (not shown in Figure 3.1d) that leaks through the Si wafer, introducing extra noise and radiation that makes the EOS trace interpretation more complex. Because the umbrella modes are in a narrow spectral region around 950 cm^{-1}, an $AgGaS_2$ crystal (AGS, 5x5x0.1 mm, θ=57° and ϕ=45°) is used in the EOS setup. As it is demonstrated in the next section, AGS provides the highest detection efficiency around the umbrella modes, allowing for the identification of the different spectral components.

The reader could think at this point that the results presented above with GaP and GaSe are not strictly necessary to reach the goal of detecting signals from cations. In terms of experimental proof-of-principle, these are instead crucial tests to perform. Different crystals reveal different portions of the molecular emission or absorption. GaP and GaSe can, therefore, reveal information on the spectral shape of the THz at frequencies that cannot be detected using AGS.

To sum up, with the three crystals we phase-match respectively: 0-100 cm^{-1} with GaP, 50 - 600 cm^{-1} with GaSe and 700 - 1100 cm^{-1} with AGS. The use of different crystals gives the possibility to detect not only vibrations but also rotations, providing a rotovibrational map of a molecule and giving the opportunity to study different modes.

3.3 Detection of NH_3^+ umbrella modes

Now we want to demonstrate that it is possible to distinguish the three dynamics mentioned in the previous section for the umbrella modes. While the second process (THz radiation following ionization) can be easily isolated by looking at the time trace after a few hundreds of fs, the linear absorption of THz and the TMF signal are more complex to distinguish. This is due to the multi-dimensional set of parameters in which these evolve. The main parameters that we can tune are the CEP, intensity and focus size of the pump, gas nozzle position and gas pressure. To reveal dynamics related to ionized molecules it is necessary to carefully verify that each of these knobs is carefully tuned.

One parameter that is not mentioned above, is the orientation of the molecules. Unlike in other applications, the pump pulses act as an alignment selector, ionizing preferentially the molecules aligned parallel to the laser polarization. This has been demonstrated in [98] for ammonia in the case of ultrashort pulses. Moreover, the asymmetry of the field selects the molecules oriented with the lone pair pointing downwards if the field is pointing upwards. Keeping in mind that the TMF contribution from the cations, which is a dipole emission, scales with the square of the number of emitters, orienting the molecules would

result in an increase of signal by a factor of 9. The emitters that contribute to the signal would be indeed three times higher. Among the several parameters mentioned above, the first one to fix is the gas pressure because this would in turn influence all the other factors. This dependency has been characterized like in chapter 2 for argon, leading to similar a similar trend. At the value of 75 mbar backing pressure, the signal does not saturate at the highest available pump intensity and, therefore, this is the pressure set in the experiments presented here.

The other parameters are tuned to achieve the highest difference between spectral features of neutral and cationic ammonia. The results thus obtained are shown in Figure 3.4. The time trace in Figure 3.4a shows the average of a series of five scans within a time window which spans from -1 to almost 6 ps. The narrow phase-matching stretches the THz contribution over a longer time scale. To look at the background-free signal it is, therefore, necessary to cut the time trace after 400 fs (red box). Figure 3.4b shows the FFT squared of the time trace contained in this temporal window. To avoid sharp features at the extrema of the time trace, the latter is windowed with a super-Gaussian function. The light blue shaded area indicates the standard deviation of the measurements.

From the spectrum in Figure 3.4b, the two main features of the umbrella modes can be identified (929 cm^{-1} and 965 cm^{-1}). The small band at 950 cm^{-1} can also be found in the neutral spectrum of Figure 3.1c. This proves that the detection system has a spectral resolution better than 15 cm^{-1}. This is high enough to resolve spectral features from cations.

To assign the other features, it is necessary to refer to [90]. Here ZEKE experiments and supporting calculations demonstrate that the cation's lowest vibrational mode (umbrella) occurs at 894 cm^{-1}. This feature is present in the spectrum of Figure 3.4b and can be assigned to NH_3^+. The features below 894 cm^{-1} cannot be assigned to any of the two species and are probably due to excited states of neutral ammonia. The components around 1040 cm^{-1} could potentially belong to ammonia molecules ionized from the N-H bond but given the higher ionization potential (15 eV) this is likely not the case. Another source of these features could be clustering happening in the focus. Further analysis would be required to understand the origin of these components. The analysis performed here is limited to the investigation of the component at 894 cm^{-1}. To study the evolution of the system a time-frequency analysis is performed by Gabor-transforming the trace in Figure 3.4a.

Figure 3.5a shows the FFT squared of different time windows. The main features of neutral and ionized ammonia shown above emerge after 400 fs (red and yellow curves) while they are hidden by the THz radiation at earlier times (blue curve). The modulation in the blue spectrum is due to both phase-matching and the linear absorption of neutral ammonia. The non-trivial evolution of the spectral features calls for simulations able to explain the dynamics involved in the system. The analysis carried out above demonstrates that it is possible to detect vibrations of cations. Now, we want to present a pilot study on how we can control those vibrations. These measurements consist on changing the field and show how different spectral components are present at different field's symmetries. To prove it, two intensity scans at two different values of the CEP are performed.

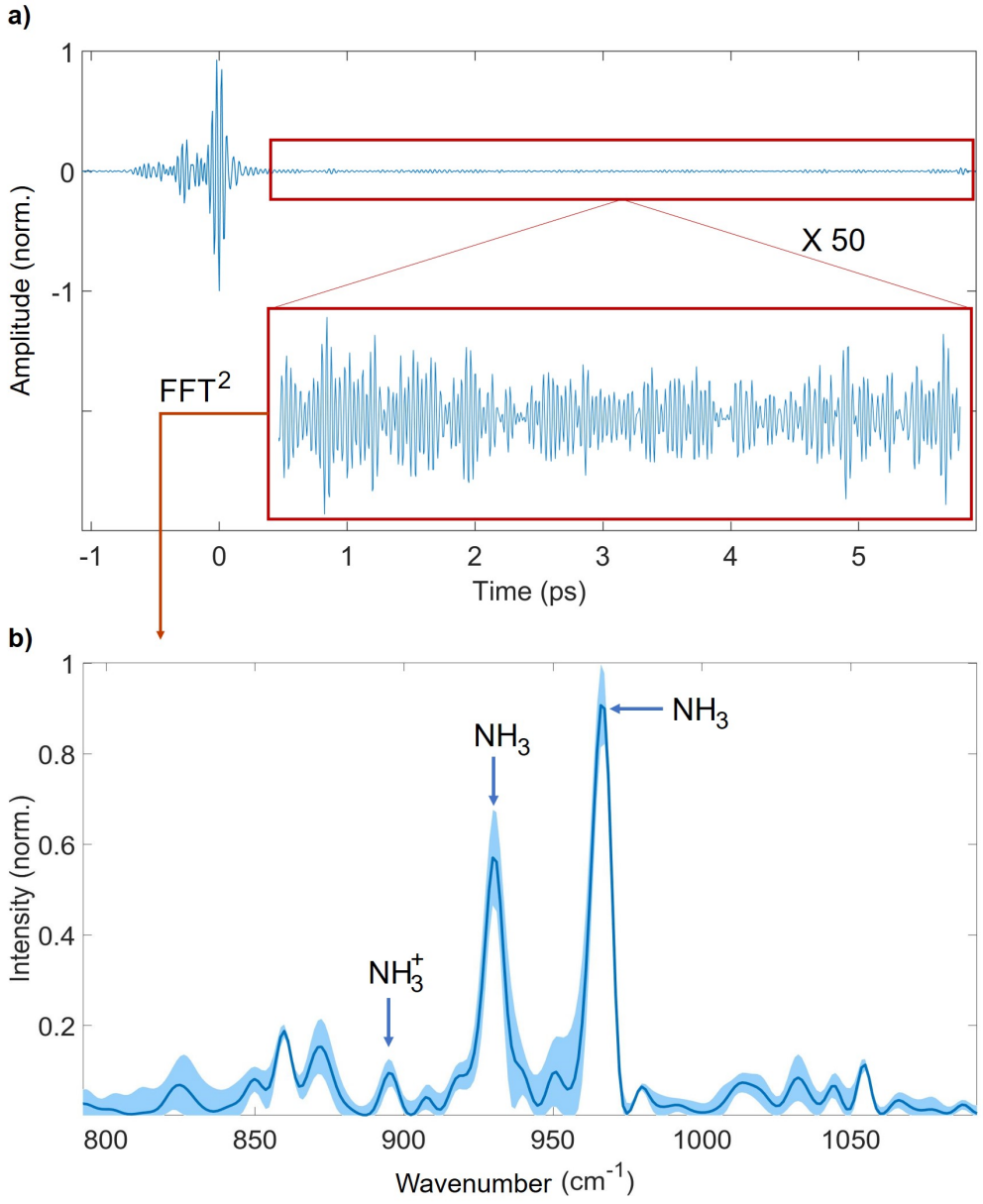

Figure 3.4: EOS trace of NH3 recorded with AGS. (a) shows the average of five EOS traces obtained using ammonia at a backing pressure of 75 mbar. The EOS crystal used is AGS. After the initial THz due to ionization (until $\sim$ 400 fs) the radiation left is given by the linear free induction decay signal and the emission from ionized molecules (TMF signature). The zoomed-in part of the time trace shows how these components evolve in time. The FFT squared of this region (zoomed-in in the red box) is shown in (b). The blue arrows indicate to which molecule the spectral features are assigned.

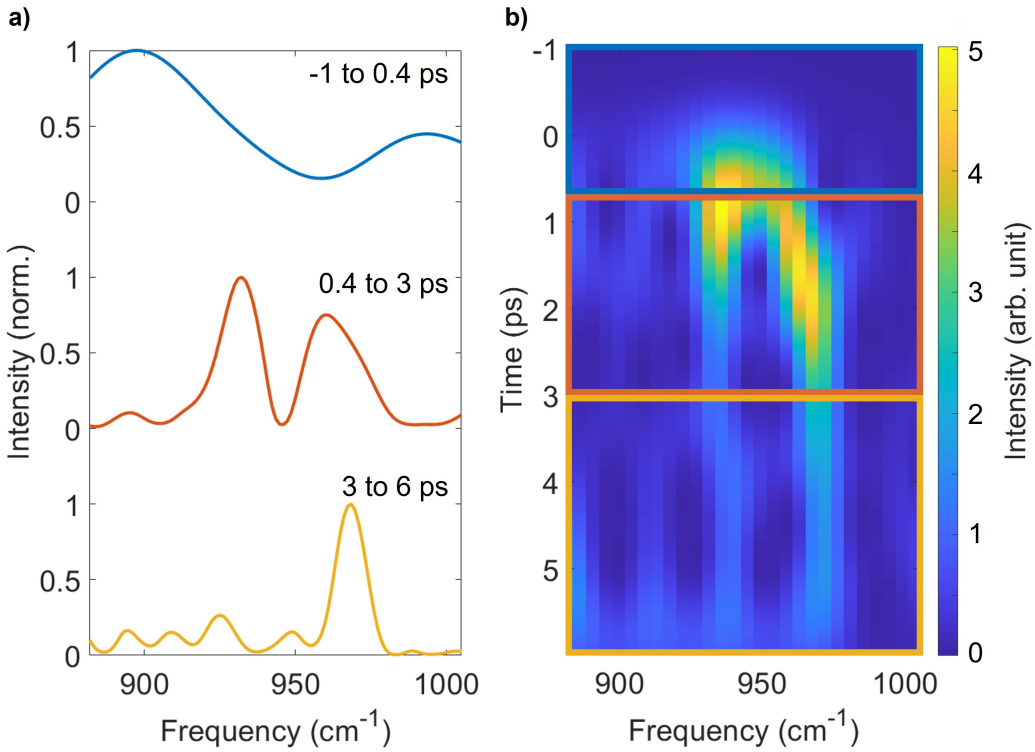

Figure 3.5: Time windowed spectra and Gabor transform. (a) shows three different spectra obtained by picking the part of the time trace within the interval specified on the top right of each spectrum. (b) shows the Gabor transform of the trace after 400 fs. The voxel size is chosen such to favour spectral over temporal resolution.

The results are shown in Figure 3.6a. The data analysis is done following the procedure explained in chapter 2. To understand what information can be extracted from the plots in Figure 3.6a it is necessary to refer to the three dynamics mentioned at the beginning of section 3.2. Because the measurements show the spectrum of the background-free part of the EOS trace, the THz radiation can be excluded as a component in this plot. The TMF and the linear absorption contributions are both present but their behaviour is different under CEP changes. The THz linear absorption, within the narrowband spectrum considered, depends just on the pump power. This means that at different CEPs we expect the same frequencies but with a different intensity, proportional to the THz power. On the other hand, the TMF signal is CEP dependent. The final state of the cation indeed is affected by the shape of the pulse. If the pump is symmetric it ionizes molecules independently from their orientation. Therefore, similarly to the THz generation, the signal from the cations cannot build up constructively for symmetric pulses. In the case of an asymmetric pulse only the molecules with a given orientation are preferentially ionized. This means that the cationic emission can build up coherently.

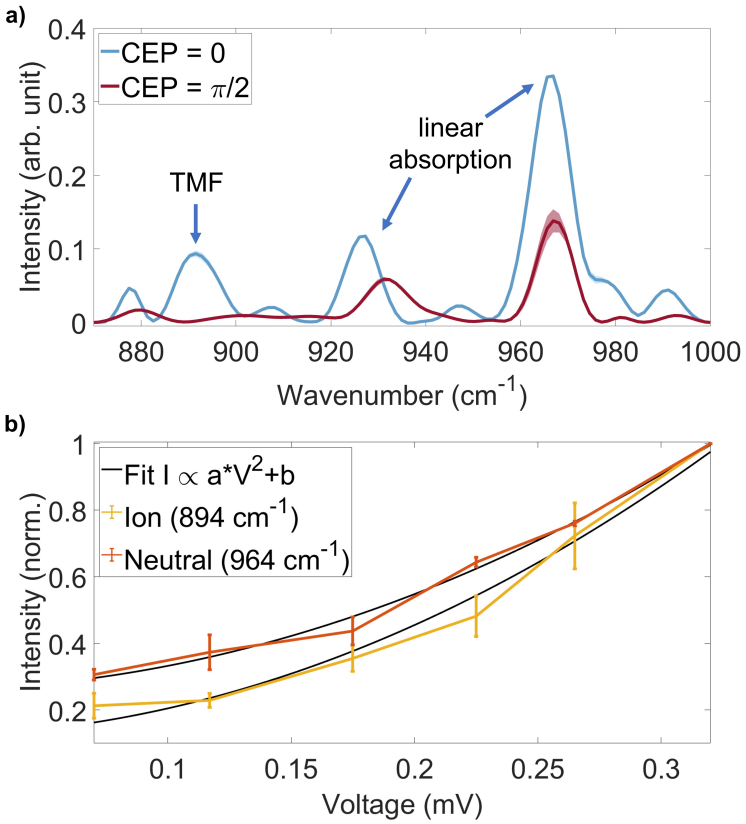

Figure 3.6: CEP and intensity dependence of ammonia. a) shows two different intensity scaling performed for two different CEPs of the pump pulses (0 and π). b) displays how the intensity for the spectral components at 894 and 964 cm^{-1} changes as a function of the number of emitters. The black lines are the fitting curves according to the equation reported in the legend.

Coming back to the results shown here, the red and the blue lines of Figure 3.6a have several similar features, like the two features at 932 ($\pm$ 2) and 964 cm^{-1}. These can be assigned to neutral ammonia. The feature at 894 cm^{-1}, the frequency that we assigned above to ammonia cations, is present only at CEP = 0. This demonstrates that it is possible to control the coherence of the ionised molecules in the focus by tuning the symmetry of the pump pulses. The shift of 4 cm^{-1} of the 932 component is due to the resolution of the system. This is proportional to the time window of the EOS scan. Because of the crystal's internal reflection at 6 ps, the resolution cannot be higher than 6.5 cm^{-1}.

A second feature that we can characterise is how the neutral and cationic components scale with the number of emitters. While these have a different dependence on the pump's CEP, they are expected to have the same trend on the number of emitters. Under the dipole approximation, the emitted THz power is proportional to the square of the number of emitters. The free induction decay, being linear with the THz radiation, has also the same proportionality. The TMF signal depends on the number of emitters quadratically

as well because the dipole induced in the cation oscillates according to the superposition of states in which is left by the impulsive ionization. It follows that both contributions have the same proportionality with the number of emitters. Figure 3.6b depicts what was just described. The intensity of two peaks, 894 cm^{-1} (cationic emission) and 964 cm^{-1} (neutral ammonia) is plotted as a function of the number of emitters. Both curves scale with the square of this quantity as indicated by the fit (black line). The number of charges is measured by setting up a biased pair of electrodes on two opposite sides of the gas nozzle. The electrodes are connected to an external circuit in which the voltage is read out by an oscilloscope and is measured in mV.

3.4 Concluding remarks

In this chapter we analysed the impulsive ionization of ammonia in the gas phase.The chapter shows how it is possible to distinguish between the free induction decay signal due to linear THz absorption and cationic emission, here, referred to as transient molecular fingerprint (TMF).

Ammonia has been chosen as the molecule to study because, upon ionization, its geometry changes from pyramidal to planar and because of its umbrella mode features. To observe the direct emission of excited cationic states, an EOS-based detection is implemented. This provides high sensitivity and a background-free readout. AGS is used as EOS crystal to directly capture the radiation from the umbrella modes of ammonia molecules around 950 cm^{-1}. The temporal-spectral evolution of the recorded EOS traces gives access to molecular dynamics and allows for the selection of the best time window to isolate the TMF signature from THz emission. The identification of frequencies that belong to cationic emission can already be achieved by looking at the spectrum after ionization. Nevertheless, their unambiguous assignment can be obtained only by looking at the CEP-dependent spectra. These reveal that only frequencies which belong to the cationic emission can be controlled with the pump CEP. The dependence on the number of emitters has also been characterised, proving that both the neutral and cationic contribution scale with the square of the emitters, stressing the importance of an efficient asymmetric ionization. The detectable bandwidth of the setup limited our analysis to the umbrella modes. Potentially, the study could be extended to higher-frequency vibrational modes. In the case of ammonia, several features could be explored like Jahn-Teller effects taking place in the $\tilde{A}^2E$ state of ammonia cations [99, 91].

In conclusion, this study opens up the door to the investigation and control of cationic states of small molecules. If combined with broader and more tunable sources, like the one shown in chapter 4, this control could be exerted over a wider frequency range and with a higher degree of control over field-dependent dynamics.

Chapter 4

Sub-cycle waveform synthesizer

In the previous chapter, it is shown an application of how single-cycle pulses can be used to initiate ultrafast motions in molecules. Ideally, what is needed is a laser field able to control highly nonlinear dynamics. Ultrashort pulses can induce the highest nonlinearity when they are compressed down to their Fourier limit. If further peak power is required to achieve a given nonlinearity, these pulses can be either amplified in nonlinear media or spectrally broadened and then compressed. In this chapter both methods are used to achieve, using a two-channel synthesizer, the generation of 3.8 fs pulses at 1.7 μm. With a peak power of 400 MW and a spectrum that spans from the IR to the visible spectral range of light, this source is the ideal platform to study dynamics in the few-fs regime. In section 4.1 different amplification schemes are introduced with particular attention given to optical parametric chirped-pulse amplifiers (OPCPAs), being this the laser pump used for the measurements performed in this chapter. The OPCPA implemented here is based on a hybrid amplification scheme and provides 15 fs pulses at 2 μm with an average power of 3 W. In section 4.2 the pulses out of the OPCPA are spectrally broadened in ambient air in a hollow-core fiber (HCF). Their spectrum is carefully analysed, in particular, their dependence on the CEP of the OPCPA pulses. In section 4.3 a waveform synthesizer is presented. This can control the arrival time and duration of three different channels, one spectral octave each. In the same section is described how these pulses are detected using EOS, in both temporal and spatial domain, and NPS. The measurements presented here are based on the work done by the author on [100] and [101].

4.1 Hybrid phase-matching OPCPA

4.1.1 OPCPA working principle

The quest for controlling ultrafast motion in atoms has pushed the development of laser sources able to trigger and investigate ultrashort dynamics. Powerful femtosecond laser sources are the natural probing tools of the attosecond and femtosecond realm. Intense ultrashort lasers are indeed necessary for HHG and, in general, to generate highly nonlinear

processes within a confined time window. One requirement that laser sources have to satisfy is power scalability over a broad range of frequencies. This is a crucial feature if we want to amplify short pulses but still keep their spectral phase undistorted. Different amplification schemes can produce powerful few-cycle pulses [102, 103]. Optical parametric amplifiers (OPAs) are among those [104, 105]. In the theoretical chapter 1, we described how OPAs transfer energy to a laser seed. Here this concept is considered in a real case scenario to introduce the experimental setup used to pump the waveform synthesizer of section 4.3.

The process shown in Figure 1.3 of chapter 1 depicts how in an OPA a photon of the pump is split into two lower energetic photons. This picture gives a glimpse of the interaction between pump, seed and idler, the three fields involved in the OPA process. When the seed overlaps temporally and spatially with the pump, this results in the amplification of the first via a positive feedback loop. After the pump and the seed enter the crystal, the idler is generated and amplified. The idler itself, in turn, can amplify the seed, thus favouring the transfer of energy from the pump to the seed. This positive loop gives rise to an exponential amplification. The amplitude of the seed, A_{seed} at the crystal output is given by:

$$A_{seed}(z) = A_{seed}(0)cosh(\Gamma z) \overset{z\to\infty}{\longrightarrow} \frac{A_{seed}(0)}{2} e^{(\Gamma z)} \tag{4.1}$$

where

$$\Gamma^2 = \frac{\omega_{idler}\omega_{seed}\chi_2^2}{16c^2 n_{idler} n_{seed}} |A_{pump}|^2 \tag{4.2}$$

and z is the crystal length.

The process just described can occur over a wide spectral range, thus, making OPAs widely tunable sources [106]. Because of this feature, OPAs are suitable and adaptable to different applications [107, 108, 109]. Furthermore, these systems can be operated at low [110] as well as at high repetition rate [111]. The spectral range where they operate is mainly defined by the pump source. This sets the degeneracy point which is given by half of the pump central frequency. Most of the commercially available OPAs are pumped with the fundamental produced by a Ti:Sa system. Depending on the application, in some cases this is frequency-doubled [112], producing radiation in the visible. The limited power that the latter can achieve makes OPAs in the IR a more fitting choice for the study of nonlinear effects.

The system presented here is an OPCPA that operates with a 1030 nm Yb:YAG pump laser [113] and has its degeneracy wavelength around 2 μm.

OPCPAs combine the advantages of OPAs with the ones of CPAs. Their working principle is the following: first, the pump and the seed are stretched, then amplified via OPA by a pump beam and, finally, compressed again. The procedure just described keeps the peak power low in the whole system, thus avoiding damages in the optics.

4.1.2 Seed generation and amplification in a degenerate OPCPA

The system delivers 2.1 μm pulses, 15 fs long with a power of 3 W and a repetition rate of 3 kHz [100]. The amplification is performed in two stages, based on 1/ a PPLN and 2/ a combination of two BBO crystals. Unlike other systems that rely on KTA [114], $LiNbO_3$ [115] or BiB_3O_6[116, 117], this offers a spectrally broader amplification as is explained below.

In the OPCPA here described, the 2.1 μm seed is generated from broadened Ti:Sa pulses via intrapulse DFG in a type-II BBO [118]. The seed spans from 1.6 μm up to 2.7 μm (central wavelength 2 μm). The main advantage of intrapulse DFG is that the seed pulses are intrinsically CEP stable, a feature that facilitates EOS detection. The use of a type-II BBO assures that both the OPCPA seed and the transmitted broadened Ti:Sa pulses preserve a flat spectral phase. This allows recycling the transmitted fields which can then be employed as possible gating pulses. After the seed is generated, it is sent to the OPCPA and combined with the pump. In this system, the last is provided by a thin-disk laser (Yb:YAG) which produces 50 W pulses at 1030 nm with a pulse duration of 1.4 ps.

To work efficiently, OPAs require crystals with the following features: high damage threshold, wide transparency range and broad phase-matching. The first characteristic defines the achievable OPA power. Crystals like periodically poled lithium niobate (PPLN) possess the last two features (around 2 μm) but have a relatively low damage threshold. Unfortunately, they cannot be grown with a wide surface area. This is the reason why a PPLN is used here just as the first amplification stage to bring the seed power up to 100 mW (33 μJ). If pulses with an energy of a few mJs are required, it is necessary to resort to another crystal configuration for further amplification. $LiNbO_3$ is a common choice that allows reaching the mJ level [119]. This crystal, despite having a large nonlinear coefficient around 2 μm is particularly sensitive to photorefractive damages. Even though making the beam larger could solve the problem, there are other factors to take into account. What makes $LiNbO_3$ a good and a bad option at the same time is its zero-dispersion point (ZDP). This is the frequency at which lower frequencies experience a negative GDD while higher frequencies a positive GDD. The ZDP is the ideal point where to phase-match the amplification being here the broadest. On the other hand, what just said implies that also SHG is phase-matched. The direct effect of SHG is the depletion of the pump which, therefore, cannot transfer efficiently power to the seed. Since we are operating the OPA in this degenerate configuration (pump at $\sim$ 1 μm and seed at $\sim$ 2 μm), the pump conversion into two equally low-frequency photons affects the OPCPA's efficiency. BBO represents a valid alternative to $LiNbO_3$, having a higher damage threshold. Its relatively low ZDP (1.5 μm), while hindering SHG, shrinks the amplification bandwidth compared to $LiNbO_3$. Nevertheless, a configuration can be found where two BBOs reach a broader phase-matching than $LiNbO_3$. The scheme is shown in Figure 4.1. A type-I and a type-II BBO, positioned 5 mm apart, are combined into a single amplification stage. To understand the underlying principle behind this scheme we can refer to the schematic in Figure 4.1a. I the case of type-II the seed and the idler propagate along two different axes, in particular, because the seed travels along the slower axis, higher frequencies are favoured.

The opposite happens for the type-I BBO. Figure 4.1b and Figure 4.1c show the results of a simulation performed by Dr Nicholas Karpowicz. In Figure 4.1b the simulated output spectrum after the first stage (PPLN) is propagated through the two BBOs. Figure 4.1c, instead, shows how the total intensity changes while the beam travels into the two crystals. The power saturates after the first crystal but not after the second. This implies that more energy could go to the red portion of the spectrum if the crystals were pumped harder. This though could lead to thermal effects which would require active cooling. Another side effect of hard-pumping is gain saturation in the crystals. Saturation results in distortions of the spatio-temporal profile which can make the beam practically impossible to focus while still preserving a short pulse duration [120]. A more detailed description of the system is reported in Figure 4.2.

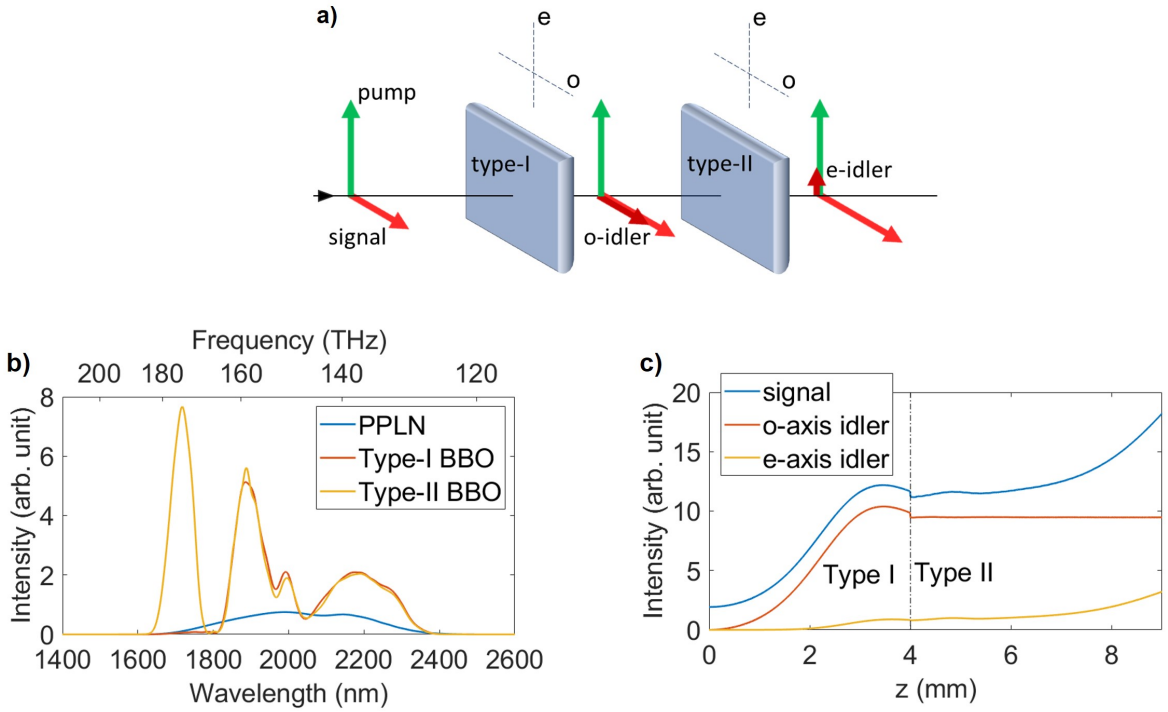

Figure 4.1: Second amplification stage. (a) depicts the working principle of the two-BBOs stage. The arrows indicate the polarization direction of the beams. Switching between type-I and II sets the idler into two different axes avoiding its build-up. (b) shows the simulated intensity after each BBO. In (c) is plotted the intensity build-up through the two crystals. The dashed line indicates the interface between the two BBOs, 4 and 5 mm thick, respectively. Figures adapted from [100]

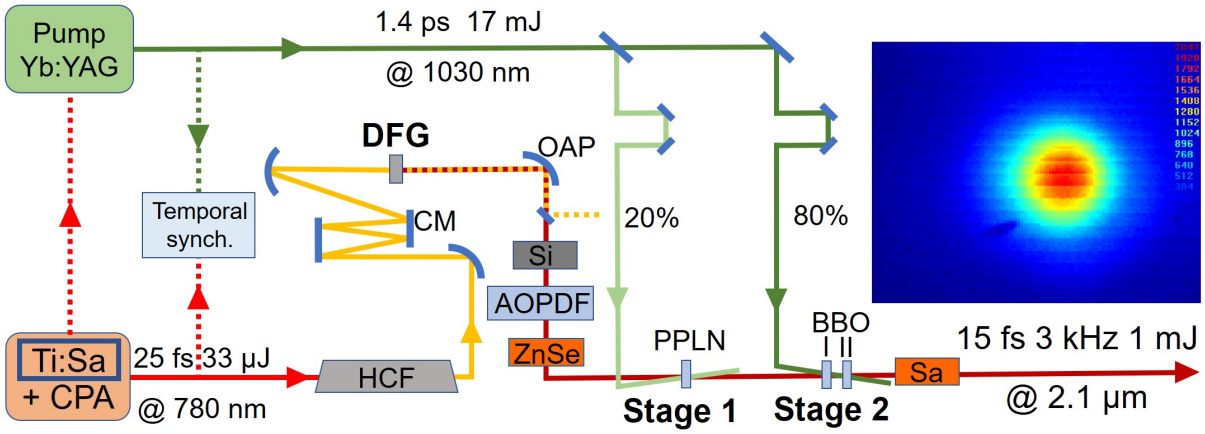

Figure 4.2: 2.1 μm OPCPA. The OPCPA is feed via a Ti:Sa oscillator, which provides CEP stable 780 nm pulses at 78 MHz. A dichroic beam-splitter transmits the spectral region around 1030 nm and reflects the rest of the pulse. The 1030 nm portion is sent to a fiber amplifier and provides the seed for the OPCPA pump. The 1030 nm portion is further amplified by a diode laser in a Yb:YAG thin disk-based regenerative amplifier. Before this step, the repetition rate is reduced from 78 MHz down to 3 kHz. The amplified pulses, after a grating compressor, achieve a pulse energy of 17 mJ and a duration of 1.4 ps. The reflected portion of the Ti:Sa pulses is instead sent to a CPA. Here the repetition rate is reduced to 3 kHz before amplification. The CPA provides 25 fs pulses and a power of 2.5 W. After compression, a second dichroic beamsplitter transmits 5% of the pulse energy which is then used for the OPCPA seed generation. The other 95% of the power is sent to another setup. The amplified pulses are spectrally broadened in a hollow-core fiber (HCF) where white-light (WL) is generated and compressed using chirped mirrors (CM). The pulses have a pulse duration of 4 fs and are focused on a type-II BBO for the 2 μm OPCPA seed generation. A 90° off-axis parabola (OAP) collimates the transmitted WL pulses and the 2 μm seed. The two have orthogonal polarizations and can be easily split by a wire-grid polarizer. A Si wafer stretches the pulses before sending them to an acousto-optic programmable dispersive filter (AOPDF). The stretching increases the efficiency of the AOPDF which has the role of actively controlling the spectral phase of the seed. ZnSe provides extra chirp before the first OPCPA stage. The first crystal used is PPLN which provides 100 mW when the seed is combined with 20% of the pump power. The pre-amplified seed is then sent to the second stage where it is amplified by the remaining 80% of the pump. The second stage is a combination of two types of BBOs as explained in the main text. A sapphire block provides the final compression to the pulses. After the sapphire block, the pulses are 15 fs long and have a power of 1 mJ. At 2.1 μm this means that the pulses are 2.2 optical cycles long. The inset shows the beam profile at the OPCPA output. Figure adapted from [100]

The system shown above is a modified version of the set up described in [119]. Compared to the OPCPA in [119], here the seed path, from the generation to the final amplification, is considerably shorter (see [120] and [121] for further details). The stages have been reduced from three to two, greatly simplifying the setup and its operation. The beam path has been indeed reduced by roughly three meters. In the current version, there are no optics between the two amplification stages, thus reducing thermal effects as well as long-term drifts and fluctuations. This comes with the price of losing degrees of control over the seed. The relative size of the pump and seed on the crystals heavily influences the performances and the stability of the OPCPA. With the use of telescopes, it is possible to adapt the pump size such that the seed experiences almost a constant beam intensity along the surface of the crystal, thus, amplifying uniformly the seed. The divergence of the last is set such that the focus is between the two stages. This allows for the compensation of possible wavefront distortions during amplification. To check the reproducibility of the amplified pulses the spectrum of the seed after intrapulse DFG, first and second amplification stage is recorded over one month of operation. The results are shown below in Figure 4.3.

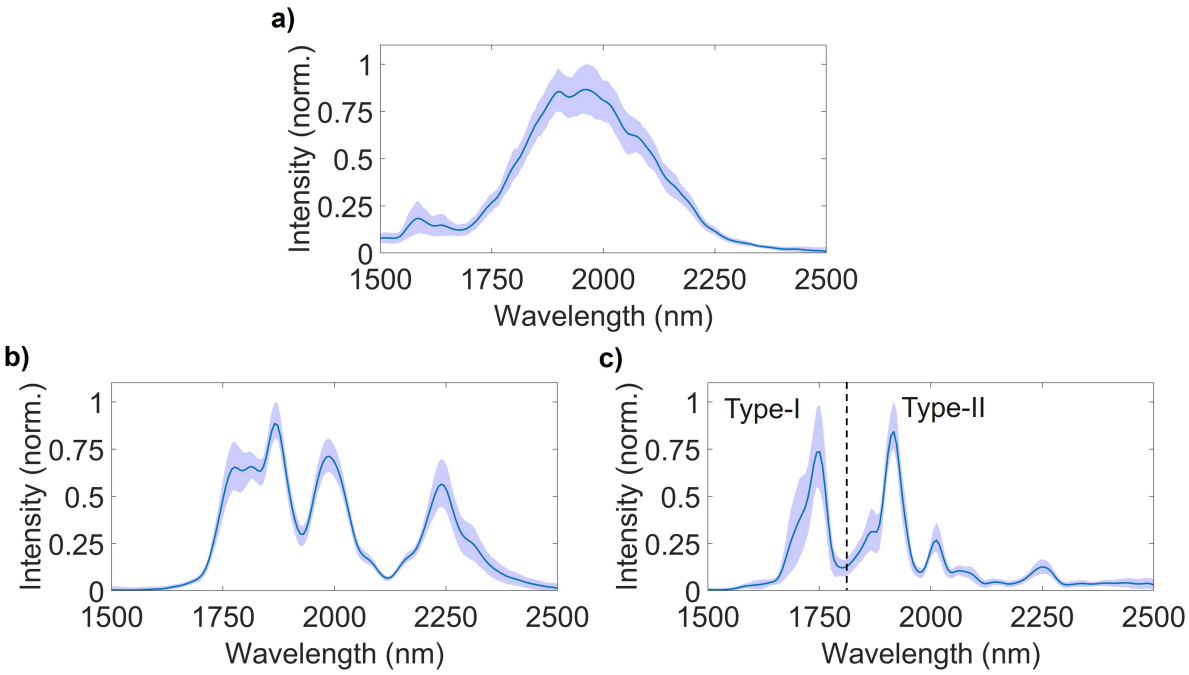

Figure 4.3: OPCPA spectra before and after amplification. The shaded areas show the standard deviation and the solid lines the average spectra. (a) shows the spectrum after intrapulse DFG, (b) after the PPLN and (c) after the two BBOs recorded over one month. It is clear how the phase-matching affects the smooth incoming spectrum from (a). When the OPCPA saturates the spectrum presents more intense narrowband features, resulting in the narrowing of the spectrum. Figure adapted from [100]

The main features are well reproducible within the experimental error, demonstrating the good stability of the OPCPA. The spectra have been recorded after thermalization, which takes around 30 minutes. When compared to Figure 4.3c, the simulated spectrum in Figure 4.1b well predicts the OPCPA output.

4.1.3 EOS OPCPA field detection

So far we have looked only at the spectrum of the pulses without investigating their temporal evolution. To characterize the electric field of the amplified pulses an EOS setup is used. In this case the amplified pulses act as test pulses. The sampling pulse is instead provided by the transmitted WL after intrapulse DFG. The EOS configuration implemented here is different compared to the one shown in Figure 1.5. Test and sampling pulse are indeed combined in a type-II BBO since their polarizations are perpendicular after intrapulse DFG. The EOS readout directly shows the electric field (blue line in Figure 4.4). The measured pulse duration is 15 fs (FWHM of the pulse envelope) which means that the pulses are compressed down to two cycles. The high degree of compression is achieved by setting the AOPDF dispersion based on the information retrieved from the EOS traces. Specifically, first, the spectral phase obtained from the EOS readout is subtracted from a flat phase. The phase obtained is then added to the phase already applied by the AOPDF and, finally, the compressed pulse is recorded again via EOS. By applying this loop it is possible to compress the pulse efficiently without the use of extra material.

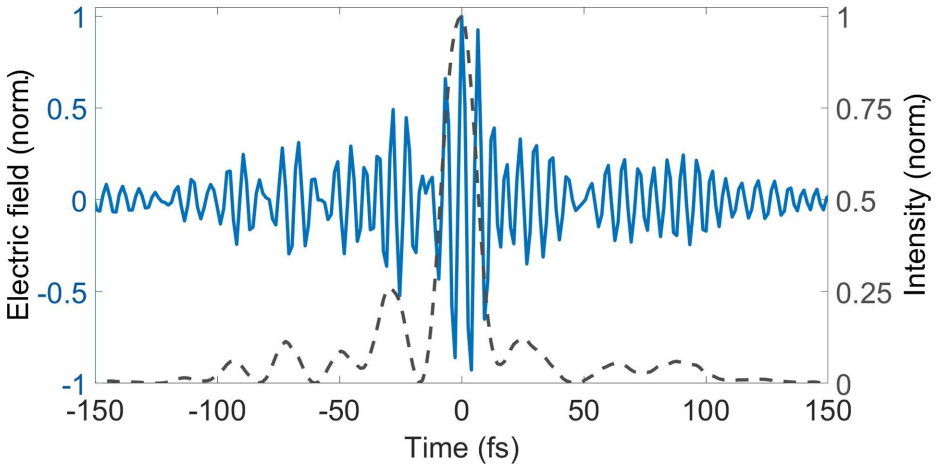

Figure 4.4: EOS reconstruction of the OPCPA pulses. In blue the EOS readout displays the electric field after the second amplification stage. Because the full power of the pulses would damage the EOS crystal, those have been attenuated before reaching the EOS setup. The grey dashed line shows the squared pulse envelope. The intensity is well confined within the most intense 2 cycles as can be seen from the good contrast between the most intense and the side peaks. Figure adapted from [100]

Because the pulses after the OPCPA are two cycles long, it is crucial to measure their CEP stability. This quantity tells how reproducible is the pulse asymmetry over time. A way to measure the relative CEP is by setting up an *f*-2*f* interferometer. If a pulse is broad enough its second harmonic (SH) can interfere with the higher frequencies of the fundamental. By introducing a temporal delay between these two components, it is possible to detect fringes in a spectrometer due to their interference. While the position of the fringes is related to the CEP of the pulses, their shift is due to CEP fluctuations. An *f*-2*f* interferometer was set up after the OPCPA to access this quantity. Before the interferometer, the pulses are first broadened in a HCF (see section 4.2) to obtain a spectrum broader than two octaves. After the HCF, a thick BBO provides both the SH and the time delay between the two spectrally overlapping components. The SH and the fundamental are then focused on a spectrometer. The results (Fig. 4.5) display a CEP stability of 64.7 mrad over one-hour continuous measurement. This value is two times lower compared to the previous OPCPA configuration [119]. To confirm that the recorded fringes are CEP dependent, we recorded a second scan where the CEP is flipped by the AOPDF from 0 to π every 800 shots. The measurements have been performed using a 100 μm thick type-I BBO.

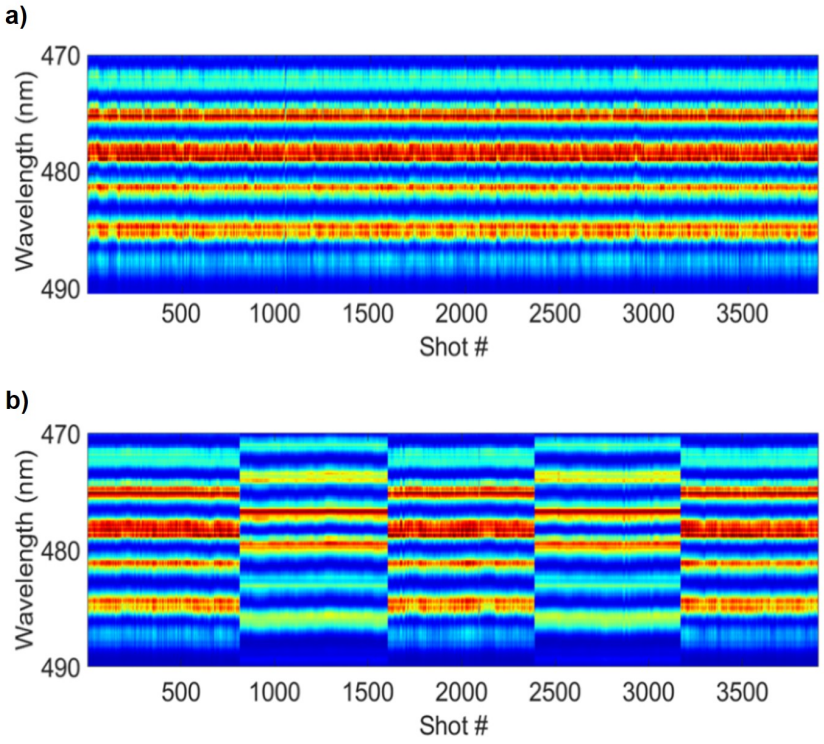

Figure 4.5: CEP stability measurements of the OPCPA pulses. (a) shows the continuous CEP measurement while (b) the one where the CEP is flipped from 0 to π. The good stability of the pulses allows to easily identify when the CEP switches from one value to another. Figure adapted from [100]

4.2 Broadening of intense IR pulses in a HCF

In the previous section, we described the amplification and characterization of the pulses out of the 2.1 μm OPCPA. The EOS setup used to measure the traces in Fig. 4.4 is based on [13], which represents the first demonstration of EOS performed in the near IR. Before this measurement, EOS was exclusively applied to the THz domain. Our goal is now to push these limits beyond the infrared, up to the visible, by synthesizing even shorter pulses which can, in turn, be used for numerous applications involving ultrafast dynamics in solids [122] and atoms [123].

To obtain ultrashort pulses, the first requirement is to generate a broad coherent spectrum. One octave, in particular, is needed to get down to the single-cycle regime. The spectral broadening of the pulses out of the OPCPA is an ideal starting point to reach even broader and therefore shorter pulses. Spectral broadening can be performed in several ways. Bulk materials, like SiO_2 [124] or CaF_2 [125], are easy to implement but are limited by the damage threshold of the medium, which in turn limits the achievable broadening and the output power. Low peak power can be a drawback if the goal is to study highly nonlinear processes. In this case, an intermediate amplification would be required. HCFs represent a valid alternative to bulk materials [126]. These glass fibers allow for the broadening of the spectrum of an incoming short pulse by exploiting the self-phase modulation (SPM) happening in the gas filling a fiber (see Figure 4.6a).

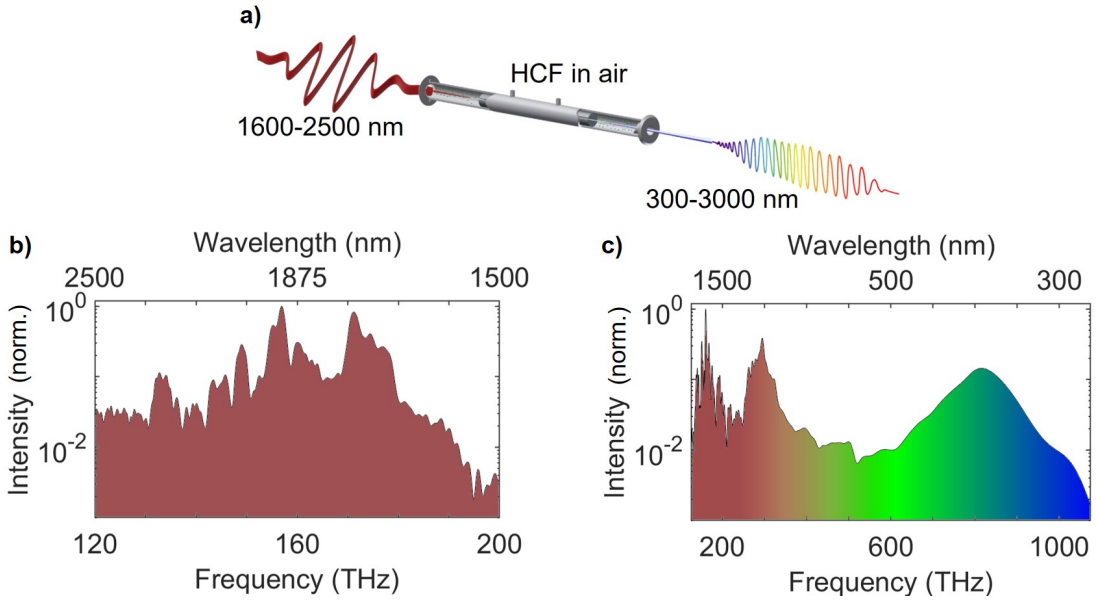

Figure 4.6: Pulse broadening in HCF. (a) shows a schematic of the broadening via SPM and the spectral limits of the incoming and outgoing OPCPA pulses. (b) shows the spectrum impinging on the fiber in log-scale. (c) displays the spectrum right after the HCF. This is then fed to the waveform synthesizer described in the next session. Figure adapted from [127] and [101]

An advantage of HCFs is that the mode after the broadening is Gaussian, indeed only the TE_{01} mode is allowed to propagate in it. Furthermore, because the broadening happens in a gas, the upper intensity limit is given by the ionization threshold which is several orders of magnitude higher compared to the one of most of the crystals. The pulses after the OPCPA are here coupled to a glass HCF 30 cm long with an inner core diameter of 250 μm. The gas used for the broadening is air at ambient pressure. The spectrum before and after the HCF is shown in Figure 4.6b and c, respectively. The last spans from 100 THz to 1000 THz, therefore, encompassing three octaves.

The laser, being confined in a small volume, can interact nonlinearly with the gas over the whole fiber length where the pulse is broadened via SPM. In a first approximation, this nonlinear process is the only one taking place in the HCF. Based on the peak intensity and focusing conditions of the incoming pulses, though, this is not the case. Looking at the spectrum of Figure 4.6c, indeed, if only SPM were present the spectrum should be symmetric around the central frequency. Because of the intensity-dependent refractive index, the peak of the pulse is delayed and therefore moved towards the trailing part of the pulse. The asymmetric temporal profile results in an asymmetric spectrum that is blue-shifted because of the steep trailing edge, thus, explaining the asymmetric profile of the spectrum in Figure 4.6c.

To get a complete picture of this spectrum, careful characterization is needed. The ultrabroad spectrum indeed cannot be detected by just one spectrometer, requiring the use of two spectrometers. The setup reported in Figure 4.7 shows that both a spectrometer and a power meter are employed. The use of a rooftop prism allows for the coupling in the spectrometer to be fixed while tuning the detected spectral range by rotating the prism. The spectrum in Figure 4.6c was obtained by recording the power of each spectral portion and weighting the spectrum by the power meter readout.

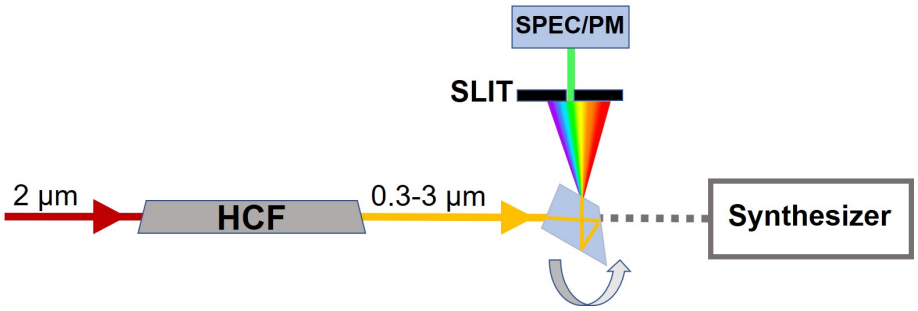

Figure 4.7: Setup for pulse broadening characterization. The picture shows a schematic of the setup used to characterize the pulses out of the HCF. A slit is used to select a small portion of the spectrum after the pulses are dispersed by a rooftop prism. By correlating the readout from the two spectrometers with the power meter readout is possible to obtain a power-weighted spectrum. Spectrometers used: MayaPro2000, Ocean Optics from 250 to 1000 and NIRQuest-512, Ocean optics from 1000 to 2700 nm. Figure adapted from [101]

The choice of air as broadening gas is motivated by the need to compress the full spectrum. Broadening in air at ambient pressure does not require the use of windows to contain the gas thus avoiding extra transmissive optics. An exit window could indeed spoil the spectral phase of the blue region of the spectrum, which is particularly sensitive to propagation through glass, being close to its absorption edge. On the other hand, operating the system becomes more complicated since the pressure cannot be tuned to optimise the broadening. Furthermore, the nonlinear factor of air is lower compared to the one of noble gasses like krypton thus requiring thinner and longer fibers.

4.2.1 CEP dependent broadening

When powerful lasers interact with matter several nonlinear effects can take place at the same time and their interplay can influence the final outcome. Different nonlinear orders can interfere with each other giving rise to interesting phenomena that can reveal the complexity of the interaction. In our case, we found out that the broadened spectrum out of the HCF is affected by CEP changes of the 2.1 μm incoming beam. The region of the output spectrum around 400 nm is recorded at different values of the pump CEP and is plotted in Figure 4.8a. A closer look at the slope of the spectral features reveals that the period over which two spectra are the same is 2π. This can be explained by taking into account the interference between two different CEP dependent effects. A period of 2π means that the two effects are one nonlinear order apart. In [128] has been observed a CEP dependent broadening with a period of π when IR ultrashort pulses were focused on a bulk SiO_2 sample. They describe the effect for the CEP dependence to be tunnelling ionization. Following the same procedure as in [128] we can write down the main contributions to the broadening as below:

$$\begin{aligned}\partial_Z \tilde{E}(r,z,\omega) = &\Big(\frac{i}{2k(\omega)}\nabla_\perp^2 + ik(\omega)\Big)\tilde{E}(r,z,\omega) + \frac{i\omega n_0 n_2}{n(\omega)c}\hat{F}[I(r,z,t)E(r,z,t)] \\ &- \frac{ie^2}{2m\epsilon_0 n(\omega)\omega c}\hat{F}[n_e(r,z,t)E(r,z,t)]\end{aligned} \tag{4.3}$$

where the first term accounts for diffraction, the second for dispersion, the third for SPM ($\hat{F}$ indicates the Fourier transform) and the fourth for tunnelling ionization (n_e indicates the electron density). In the equation above only the last two terms are CEP dependent but with a period of π, so their interference would not explain the trend reported here. To further characterise the spectra observed, the intensity dependence has been recorded twice, once setting the CEP to 0 and a second time to π. The difference between the two sets of measurements is shown in Figure 4.8b. The 2D map reveals that the dynamics is wavelength dependent, adding an extra layer of complexity to the understanding of the interaction. At the same time, the plot shows a switch between two regimes for low and high intensity that is discussed below. To simplify the visualization only two spectra are displayed in Figure 4.8c. Looking at the two plots in Figure 4.8c it emerges that at CEP $= \pi$ (orange curve) the spectrum has two peaks unlike the one at CEP $= 0$ (blue curve)

that has only one. These features are not intensity-dependent in the sense that the spectra preserve their shape even when the intensity is changed. A quick comparison between 4.8b and 4.8c proves that at lower intensities the spectra at CEP = 0 are more intense compared to the ones at CEP = π while at higher intensities the opposite happens. A direct way to visualise the processes involved in the broadening is to plot the peak intensity around 400 nm as a function of pump power. Fig. 4.8d shows that this quantity scales with the third power of the pump intensity up to 1.4 W where saturation is achieved. The presence of saturation indicates that a non-perturbative regime is achieved at this pump power.

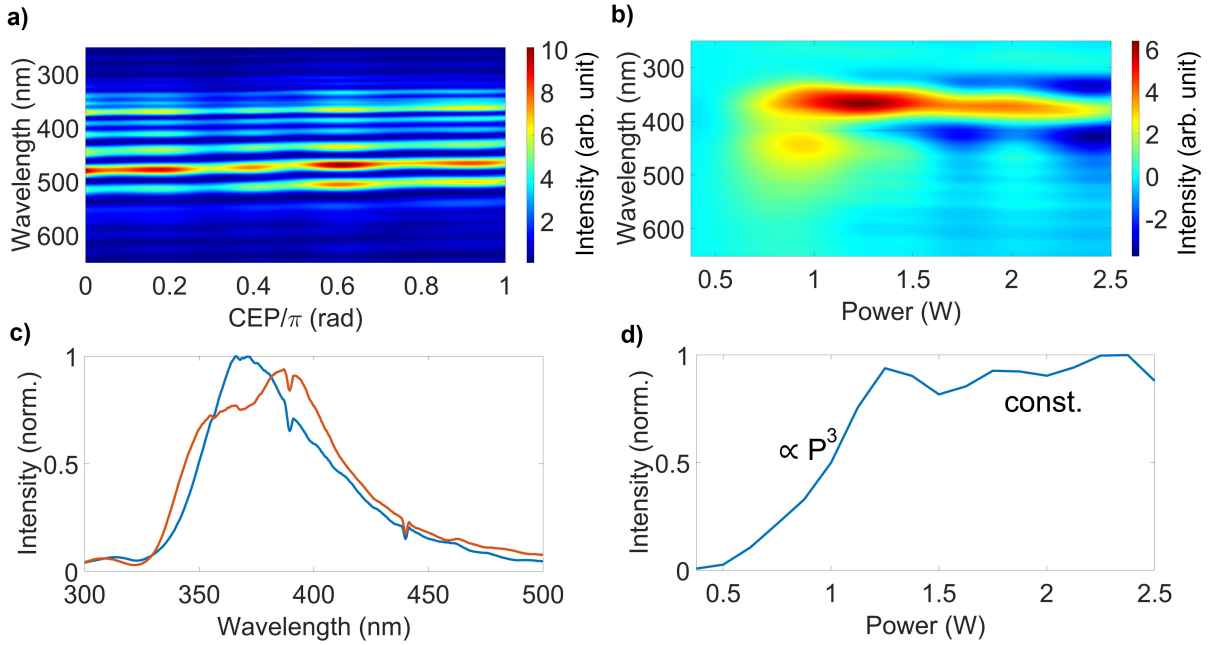

Figure 4.8: CEP dependent broadening. (a) shows spectra recorded at different CEPs. The spectral components have a period of 2π. The scan is performed from 0 to π. (b) shows the difference between the spectra at CEP = 0 and CEP = π as a function of intensity. In (c) are reported two spectra recorded at CEP 0 (blue line) and π (orange line). (d) Intensity dependence of the blue spectrum in (c). Both the CEP of the IR pulse and its intensity are controlled by the AOPDF.

The scaling at lower intensities suggests that third harmonic generation (THG) contributes to the broadening. THG would also explain the peak at 400 nm in the spectrum. If only SPM was present we would indeed expect a smoother spectrum around those frequencies. Having a TH around 375 nm implies that the fundamental is around 1100 nm. The last overlaps with the corresponding feature of the output spectrum (Fig. 4.6c).

To break the symmetry a second order effect is required, like second harmonic generation (SHG). This cannot be generated along the fiber (being gas a centrosymmetric medium) but rather in the OPCPA. The interference of SH and THG can explain the CEP

dependence observed in the spectra. SHG has indeed a period of 2π while THG of 3π, their interference results in a net dependence of π. A direct consequence and advantage of the interference mechanism just discussed is that it provides a way to measure the absolute CEP over 2π [129].

The full understanding of this effect is still under investigation. A more thorough study would require the use of different gasses with higher n_2. This would have the effect of increasing the contrast between different nonlinear components.

4.3 Synthesized infrared-visible light fields

4.3.1 Coherent waveform synthesis

Laser pulses are the shortest optical shutters we have at our disposal to investigate ultrafast events. Being able to shape the temporal structure of such pulses implies controlling the way light interacts with matter on ultrashort time scales. Shaping techniques offer a way to enable this control over few-cycle pulses. Waveform synthesizers, in particular, are gaining a foothold in the attosecond community [130, 122, 131]. They allow to choose the absolute phase, the shape of single-cycle pulses and to tune their asymmetry.

In the theoretical chapter 1, we have described different ways to manipulate the spectral phase and, in general, the temporal evolution of broadband pulses. Shaping techniques like the ones shown in section 1.1 do not work efficiently with ultrabroad spectra. Their application would indeed require phase masks and gratings able to operate over multiple spectral octaves. Waveform synthesizers overcome this problem by spectrally splitting a broad spectrum into more narrowband pulses, which are then compressed and finally recombined into shorter pulses [132, 123, 22, 133, 134]. The name synthesizer comes from the possibility to generate different electric field shapes based on the relative arrival time and the CEPs of the pulses out of each channel.

There are mainly two designs to achieve coherent synthesis: sequential and parallel. The first operates by using phase and amplitude masks that act just on small spectral portions. By employing several masks in series it is possible to tune the shape of the outgoing pulse. This technique has the advantage of not requiring temporal synchronization but requires ultrabroad compensators to compress the synthesized pulses. The parallel scheme consists instead on spatially splitting different spectral portions and it is the one used in this thesis. This configuration operates, as the name suggests, in parallel on the channels where the pulses are individually compressed. This allows for the adjustment of the spectral phase using optics which works efficiently for the specific spectral region of each channel. Unlike the sequential scheme, here precise phase and temporal synchronization of the different channels is required. The parallel scheme can efficiently generate single and sub-cycle pulses both in the IR and visible.

Synthesized light transients were employed in previous works to study the electron dynamics of krypton when ionized by attosecond pulses [123]. Other applications demonstrated the applicability of tailored fields to HHG [135]. In this work synthesized IR-visible

transients are used to inject electron wavepackets in a quartz thin sample within a time window of less than a femtosecond. This demonstrates that the pulses can be synthesized reproducibly and that they can be applied to induce ultrafast dynamics on other types of samples.

The characterization of the synthesized pulses is not performed via attosecond streaking like in previous works but via EOS. The last is a cost-effective field-sensitive technique easier to implement compared to attosecond streaking because, unlike the last, does not require the setup to be in vacuum and an isolated attosecond pulse to work. Here, EOS is extended to resolve frequencies in the visible spectral range of light. Furthermore, an imaging setup is applied to resolve the spatio-temporal structure of synthesized fields.

4.3.2 Setup and EOS characterization of the IR and visible channels

As mentioned above, waveform synthesizers rely on splitting a multi-octave spectrum and synchronizing different spectral portions to generate short pulses. Here, the output of the HCF presented in the previous section is fed into a three-channel waveform synthesizer. Each channel encompasses one octave, allowing for the generation of three single-cycle channels: 300-600 nm (CH0), 600-1500 nm (CH1) and 1500-3000 nm (CH2). The setup of the synthesizer is shown in Figure 4.9. The two channels in the visible and IR, CH1 and CH2, are combined to synthesize 3.8 fs-long pulses. Spanning two spectral octaves their combination results in the syntheses of a sub-cycle pulse. The UV/visible portion of the spectrum, CH0, is instead used as a sampling pulse, having the shortest central wavelength and the shortest pulse duration when fully compressed.

Except for wedge pairs, no transmissive optics are used along each channel. The two beam splitters, the two beam combiners and the chirped mirrors are custom made and specifically designed to work on the spectral range where each channel operates [136]. For CH0 the chirped mirrors have been designed alternating layers of Hf_2O_2 and SiO_2 on a fused silica substrate. The thickness of the layers are calculated to obtain a flat spectral phase starting from the phase after the HCF and the accumulated dispersion through the air and the transmissive optics used before recombination. Nb_2O_5 and SiO_2 are instead the materials used for the CMs of CH1 and CH2 [121]. As already mentioned, for CH0 the wedge pair and air itself are highly dispersive, therefore, more bounces are needed (16) on the CMs and the least amount of transmissive optics is used. Four bounces are instead required to compress CH1 and two for CH2. All the CMs used here work in a double-angle configuration which means that a mirror pair is used at two different angles to compensate for the fast oscillations in the GDD due to the multilayer stack [137]. The beam splitters are obtained using the same structure of layers of the CMs. The materials used for the wedges are BaF_2, SiO_2 and ZnSe for CH0, CH1 and CH2, respectively. The wedges are mounted on piezo stages such that their position can be remotely controlled.

The apertures are set such that the intensity on the EOS crystal (5 μm type-I BBO) is below its damage threshold and that the intensities of CH1 and CH2 are comparable.

The polarization of the beams is set to be parallel to the optical table and is cleaned before EOS detection by two Si wafers positioned at Brewster angle. The beam divergence is also taken care of by spherical mirrors that recollimate each channel separately. The small footprint of the setup (80x60 cm^2) reduces mechanical instabilities. The beam path of each channel is indeed just 1.5 m long. Furthermore, an active beam pointing stabilizer positioned before the HCF fixes the coupling into the HCF, thus improving the performance of the synthesizer.

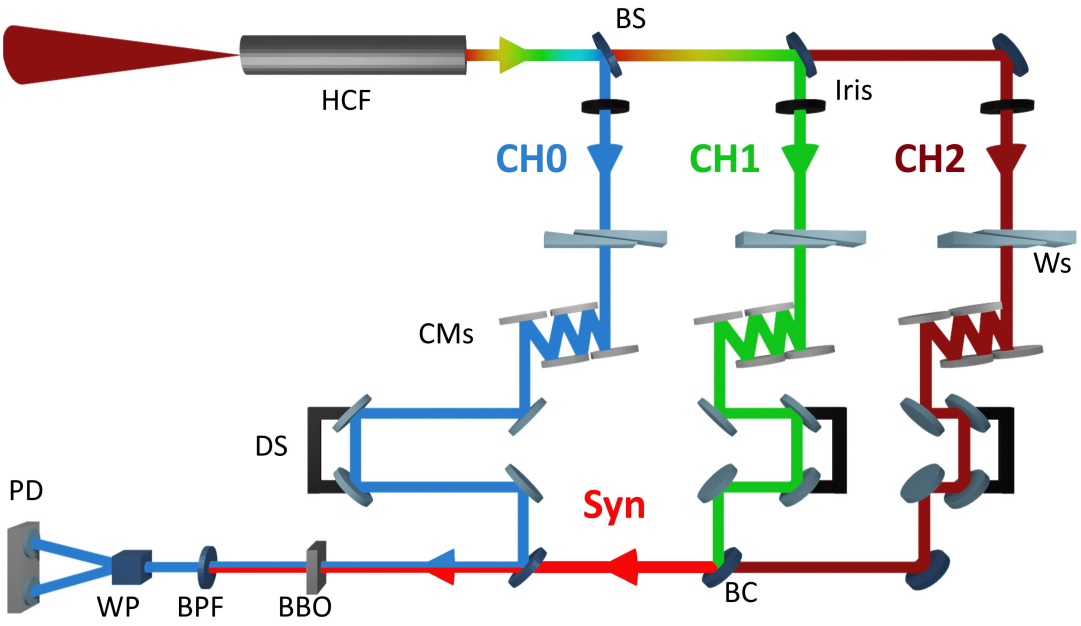

Figure 4.9: Synthesizer setup. The 2.1 μm beam out of the OPCPA is coupled in an HCF (top left). The broad spectrum is split into three channels using dichroic beam splitters (BS). The relative intensity of each channel is controlled via apertures. The channels are compressed by wedge pairs (Ws) and chirped mirrors (CMs). Delay stages (DS) control the relative arrival time and beam combiners (BC) spatially overlap the three beams and send them collinearly to the EOS crystal. The channel which spans from 300 to 600 nm, CH0, provides the sampling pulse of our EOS setup. The other two channels, CH1 (600-1500 nm) and CH2 (1500-3000 nm) are combined into a two-octave synthesized pulse (Syn), the EOS test pulse. To resolve the synthesized fields we employ a 5 μm thick type-I BBO as EOS crystal, a band-pass filter (BPF) around 320 nm, a glass Wollaston prism (WP) and a coupled photodiode (PD). The material used for the two PDs is GaP which is more suitable to detect frequencies around 320 nm compared to conventional Si detectors. Figure adapted from [100]

4.3.3 CH1 and CH2 field-resolved characterization

The setup shown above allows for the characterization of CH1 and CH2, both combined and separated, via EOS using CH0 as sampling pulse. The recorded EOS traces are shown in Figure 4.10a and 4.10b for CH2 and CH1. From the traces it is possible to calculate their pulse duration. These are 10.8±0.6 fs (at 2.2 μm, CH2)and 4.8±0.3 fs (at 1.1 μm, CH1). The pulses are therefore compressed down to almost one optical cycle. Each trace shows the average over five consecutive scans.

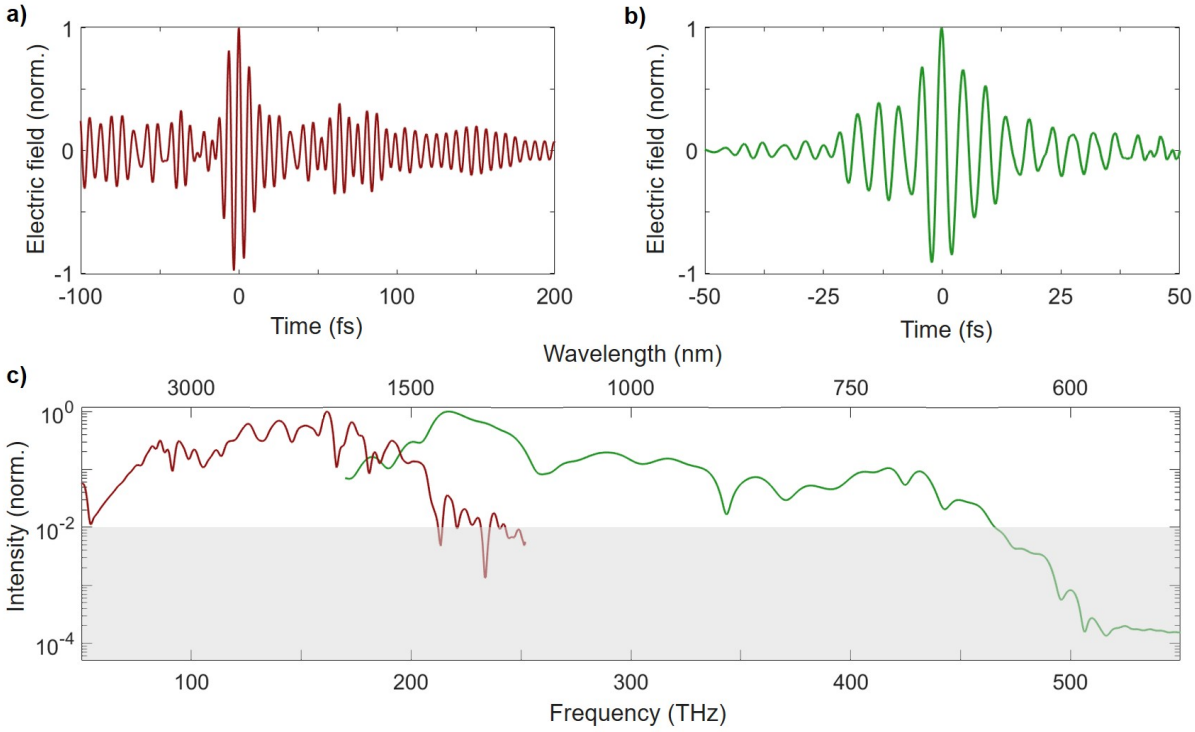

Figure 4.10: EOS measurements of CH1 and CH2. (a) shows a field-resolved measurement of CH2, (b) of CH1. In (c) the logarithm of the FFT squared of the EOS traces is shown together with a grey area which represents the region where SNR is less than 1. (c) shows that frequencies up to 450 THz (665 nm), therefore in the visible spectrum, can be field resolved via EOS. Figure adapted from [100]

Because EOS needs a compressed sampling pulse but not necessarily a compressed test pulse to work, it is possible to act on the test pulse compression without affecting the detection. This is not the case for attosecond streaking where the generation of the gating pulses is affected by the test pulse shape. In Figure 4.10c the fast Fourier transform (FFT) of the two traces is plotted. The grey area indicates the region where the SNR is below 1. The two channels have an overlapping region due to the not perfect transmission/reflection

of the optics used along the channels. Unfortunately, each set of CMs does not fully compress the wings of the spectra, making the pulses slightly more narrow-band than expected. It is indeed particularly challenging to produce CMs which reflectance is uniform over more than one octave. The spectrum shown in Figure 4.10c proves two crucial points of this work: first that EOS can work over a broad spectral range and second that frequencies up to the visible (450 THz) can be field resolved.

It is the first time, to author knowledge, that EOS has been applied to this spectral range [121, 101]. This result could not be achieved if CH0 was not compressed enough to sample 665 nm. These wavelengths have a period of 2.2 fs which implies that our sampling pulse should be as short as 1.1 fs. As demonstrated below, the pulse duration of CH0 is actually 2.8 fs. It is thanks to the right choice of spectral filters that the EOS SNR can be increased as demonstrated in [26]. In our case, the SNR is further increased by the use of a lock-in amplifier. By setting the AOPDF to flip the CEP from 0 to π every each pulse is possible to lock the detection at half the repetition rate (from 3 kHz to 1.5 kHz), thus filtering out most of the noise and gaining an extra factor of two in SNR. This type of noise reduction works only because EOS detection is sensitive just to the CEP of the test pulse and not to the one of the sampling pulse.

4.3.4 Synthesized pulses

After their characterization, CH1 and CH2 can be combined into a unique beam to form synthesized pulses. The temporal overlap can be fine-tuned with the use of delay stages (see the setup in Fig. 4.9), which provide a precision of 0.6 fs. To obtain a flat spectral phase and a short pulse duration the intensity of CH1 and CH2 is set to be the same on the EOS crystal by controlling it using apertures. The figure below shows how the pulses can be combined and their relative temporal delay (Δt) controlled in a way that allows for the synthesis of ultrashort transients when Δt equals zero. Looking at the traces from (a) to (e) of Figure 4.11 it emerges how the stability of the system is crucial to reproducibly have synthesized pulses. Even small fluctuations can indeed ruin the coherence of such broadband pulses.

The AOPDF provides another degree of freedom, the CEP, which can be directly accessed with EOS. In the case of the synthesized pulses, because of their short pulse duration, the definition of carrier and envelope becomes loose and it is better to rather talk about global phase (φ_g) [138]. Thanks to the AOPDF is possible to set a different φ_g and switch from cosine to sine pulses as shown in Figure 4.12. Both traces are obtained setting Δt =0. This result demonstrates that the control on the synthesized fields can be imparted down to the lowest order of the temporal phase. From the traces is possible to calculate the pulse duration which is 3.8$\pm$0.2 fs (FWHM of the field squared). To show that the pulse power is mostly confined within few cycles of the synthesized pulse the intensity profile of the trace in Figure 4.12a is calculated and it is shown in Figure 4.13a. The temporal and spectral phase can also be retrieved from the EOS trace and are reported in Figure 4.13 (grey line).

The FFT of the intensity profile (Fig. 4.13b) shows how EOS efficiently provides the readout of two spectral octaves in a single trace. The peak power of the synthesized pulses (400 MW) is high enough for the applications performed in this work and therefore do not require any intermediate amplification unlike in [139, 140, 141, 142].

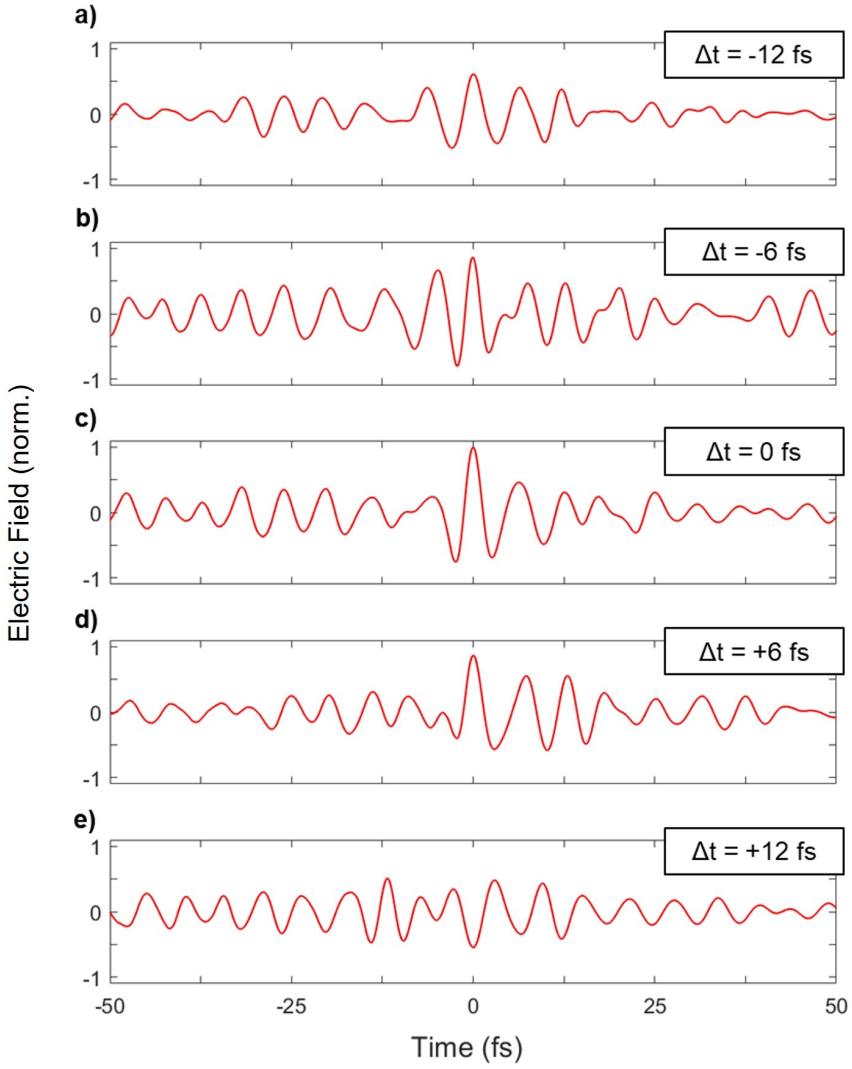

Figure 4.11: Synthesized fields at different time delays. (a)-(e) shows the combination of CH1 and CH2 detected via EOS within a time window of 100 fs. The delay between CH1 and CH2 (Δt) is changed from (a) to (e) with a step-size of 6 fs. It emerges how the shortest pulse can be achieved when Δt=0, (c). The pulse duration in (c) is 3.8 fs, which means that the pulse lasts just 0.7 optical cycles. The traces are normalized by the peak in (c).

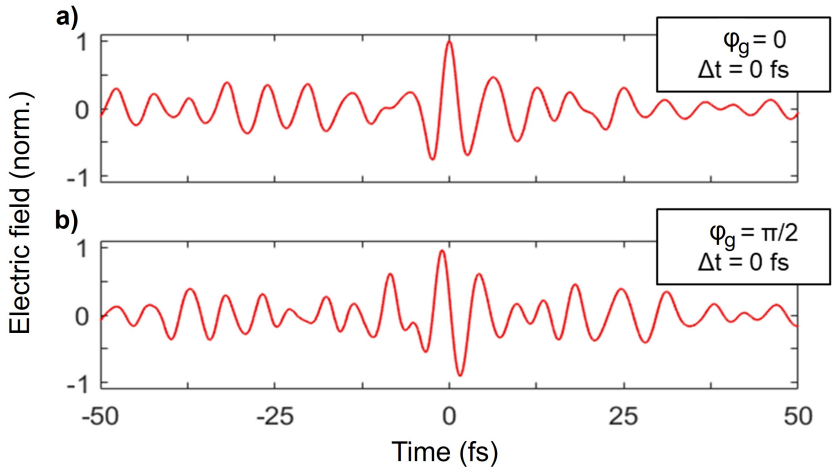

Figure 4.12: Synthesized fields with different global phases. (a) shows the same trace of Figure 4.11c but here is compared to a second trace, (b), where the global phase, φ_g, is changed from 0 to $\pi/2$ using the AOPDF. This demonstrates how the symmetry of the synthesized pulses can be actively and reproducibly controlled remotely.

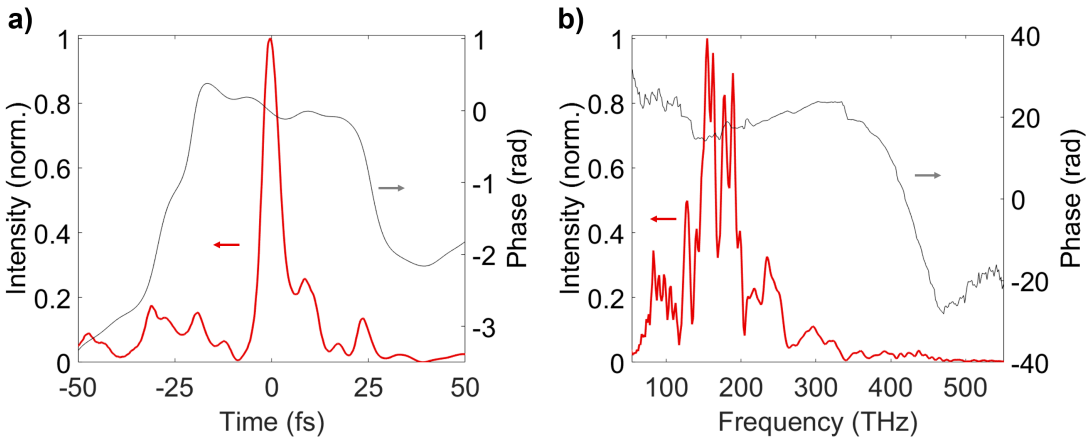

Figure 4.13: Intensity and spectrum of the synthesized pulses. In (a) the squared envelope of the trace in Figure 4.12a is plotted (red line). The pulse energy is confined within a few fs. The almost flat temporal phase (grey line) is another proof that the pulse is well compressed. (b) shows the spectrum (FFT of the intensity profile in (a)) and the spectral phase. The spectrum spans over two octaves, demonstrating that EOS can be used to sample at the same time IR and visible frequencies. The spectral phase shows that the bluest frequencies, around 400 THz, are more dispersed. This happens because of two reasons: the first is that the CMs struggle to compress frequencies that are at the edge of their working range, the second is that these frequencies are the most difficult to sample with EOS since they are strongly affected by the compression of CH0.

Before applying the synthesized pulses to a sample, the pulses must be reproducible over several scans, or at least their fluctuations negligible within the time required to carry out an experiment. This would allow us to assume that the EOS measured field is the same as the one that impinges on a sample when the pulses are not measured via EOS.

To characterise the stability of the synthesizer we measured the pulses over a time window of two hours. The traces after every hour are shown in Figure 4.14a. It results that after thermalization, which occurs within the first 30 minutes, the pulses are well reproducible. This result is obtained without using any active stabilization in the synthesizer and the instabilities can be attributed to the OPCPA.

Keeping in mind that each EOS trace of the synthesized pulse contains the information of both CH1 and CH2, it is possible, by applying a spectral filter, to characterize their relative stability. The result is shown in Figure 4.14b. We can see that after two hours the channels have drifted by 1 fs. This source of instability could be fixed by taking a leakage from the last beam combiner, looking at the interference of the two channels in a spectrometer and actively correct the stage position. The experiments performed so far did not require hours-long stability, therefore, this stabilisation is not in place.

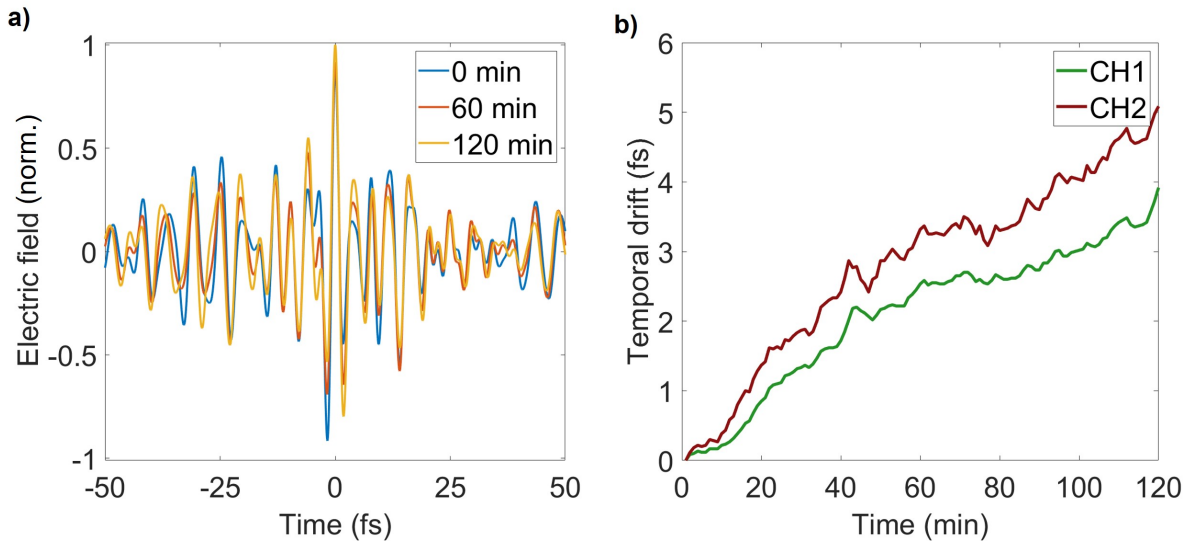

Figure 4.14: Long term stability measurements of the synthesized fields. (a) shows measurements of the synthesized fields recorded every hour. The pulses have been continuously measured, here, just three traces are shown to simplify the data visualization. Each trace is an average of five traces recorded in a row. (b) shows the drift of CH1 and CH2. The absolute value of the temporal drift is relative to CH0. This value increases because of the not perfectly reproducible stage positioning system of CH0. To avoid fluctuations indeed it is CH0 that is scanned over the synthesized trace and not the other way around. Figure adapted from [101]

4.3.5 Spatio-temporal characterization of light transients

Another property of the synthesized pulses that is worth investigating is their spatio-temporal profile. If different wavelengths are focused on different positions the pulses are not locally short but only on average. The EOS configuration presented so far does not provide any information about the spatial evolution of electric fields. The time domain traces obtained are indeed averaged over the transversal mode of the test pulse. By replacing in the EOS setup the photodiodes with a 2D array of photodiodes, in other terms a CCD camera, it is possible to access the spatial domain without losing the temporal information (see Figure 4.15). This technique is called imaging-EOS (for further details see [143] and [144]). Imaging-EOS provides in a single measurement a 2D map of the wave vectors of the test pulse. By scanning the temporal domain is possible to access their temporal evolution, therefore providing a full (2+1)D picture of the test pulse. There are several differences between EOS in the time-domain and imaging-EOS. In the imaging case, for example, we cannot rely on the use of lock-in amplification, thus resulting in longer acquisition times. On the other hand, unlike EOS in the time domain, imaging-EOS gives access to the wavefront of the test pulse and the near-field of samples positioned on the surface of the EOS crystal with sub-wavelength resolution. In our case, we are sampling frequencies in the IR and visible with a resolution given by the sampling pulse which is in the UV. Imaging-EOS also differs from its temporal counterpart in the test and sampling beam size required to get the optimal signal. EOS in the time domain works more efficiently when the sampling pulse is slightly smaller than the test pulse. This assures that SFG is maximised and not affected by the intensity variations of the test pulse along its spatial profile. For imaging-EOS the opposite is valid. Here, the sampling pulse has to be wider than the test pulse to fully sample it. The results obtained implementing imaging-EOS after the synthesizer are shown in Figure 4.16.

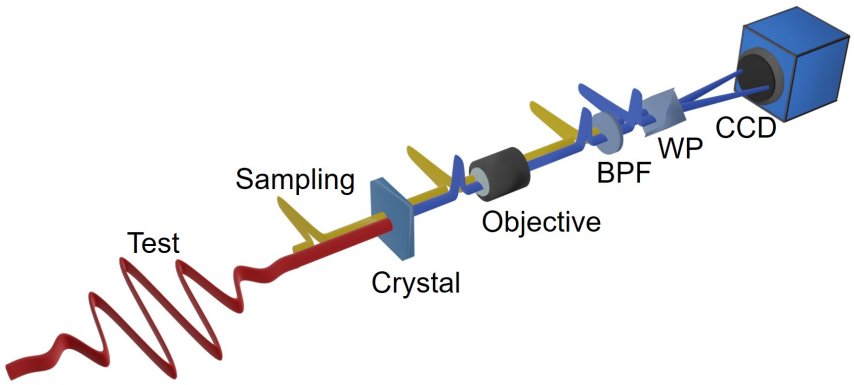

Figure 4.15: Imaging-EOS setup. The setup follows the same idea of conventional EOS except for two elements: an objective and a CCD camera. The objective is used to image the two orthogonally-polarized beams on the CCD camera, which detects the field in the spatial domain instead of coupled photodiodes.

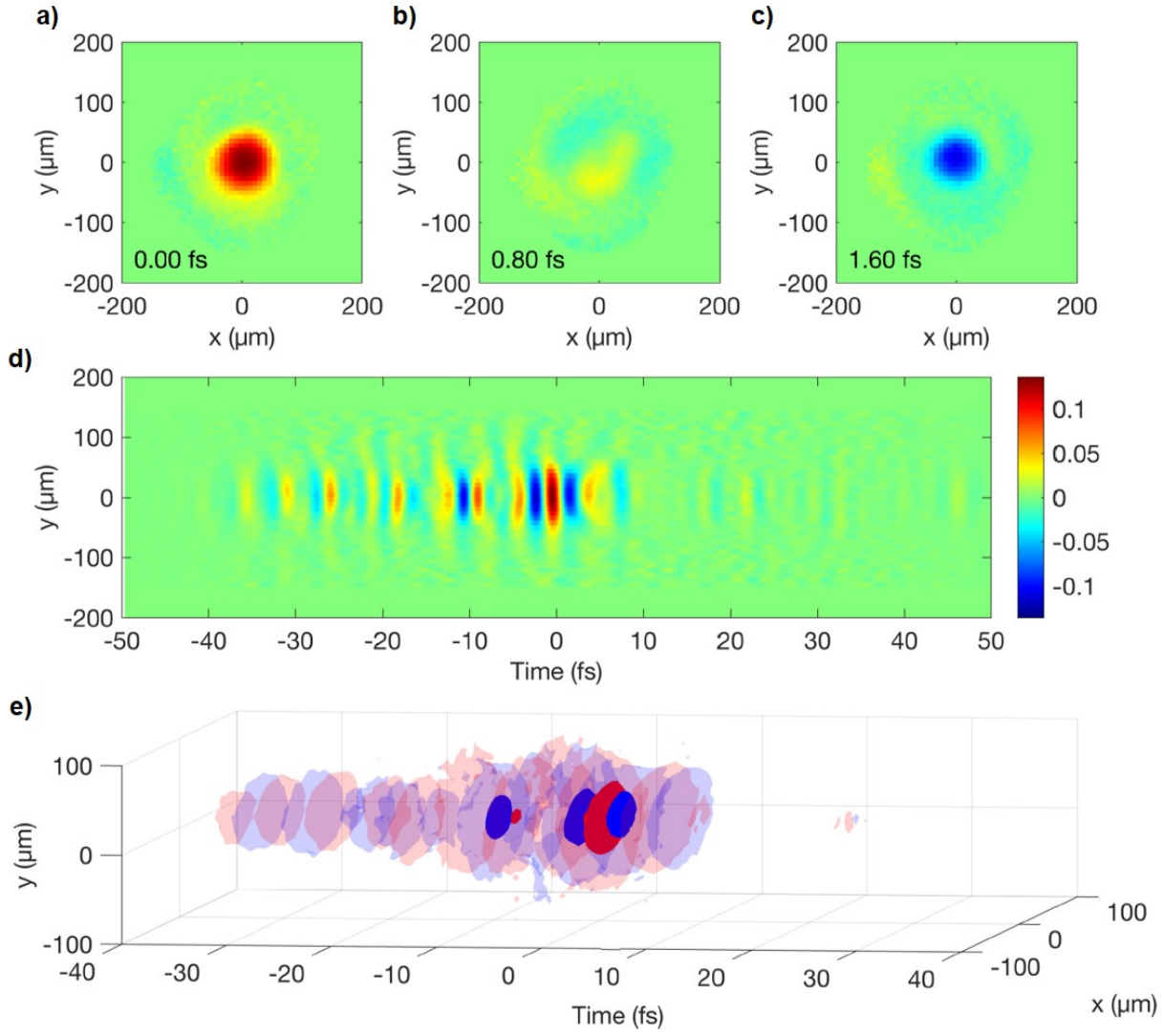

Figure 4.16: Synthesized field resolved via imaging-EOS. From (a) to (c) is shown the readout of the CCD at different time delays between CH0 and CH1+CH2. (d) displays the temporal evolution of the field. What is plotted, specifically, is the projection along the y-axis of the images recorded by the camera as a function of time. (e) shows all three dimensions combined. Image provided by Dr M. Mamaikin [145].

Figure 4.16 demonstrates that it is possible to extract all the necessary information to characterise the beam both spatially and temporally. (a)-(c) show the 2D images recorded at different delays. In particular, (a) is recorded at the positive peak of the synthesized field, (b) at the zero crossing and (c) at the negative peak. If we now integrate along the y-axis and we stuck all the images together, we obtain the 2D-plot in (d). Because of the good SNR, it is possible to directly see how the wavefront looks like. This has two advantages. First, it allows for the detection of astigmatism in the beam and, at the same

time, for the precise positioning of the EOS crystal at the test pulse focal plane. What the setup is indeed imaging is the field at the surface of the crystal. This means that if the crystal is not at the focus what we would observe, instead of the straight vertical lines in (d), would be curved fronts. As well as for standard EOS, this technique was limited to IR frequencies before this work. Here, field-resolved microscopy is extended up to the visible spectral range.

The conclusion that can be drawn from this measurement is that the synthesized pulses do not show any evident spatio-temporal distortion. This is confirmed by the roundness of the mode in (a)-(c) and by further analysis carried out in [145]. We can therefore state that the pulses recorded are short over the whole focal spot and not just at the center of the beam or on average.

4.3.6 Sub-fs injection of electron wavepackets in SiO_2

In the previous sections, the synthesized pulses were characterised both spatially and temporally, giving particular attention to the different shapes that can be obtained by changing either the arrival time or the CEP of the pulses. We are now ready to apply the pulses to induce ultrafast dynamics on solids. The experiment shown here does not require any change of the setup shown in Figure 4.9, except for replacing the EOS crystal with a thin quartz sample for nonlinear photoconductive sampling (NPS) detection. NPS, already described in chapter 1, can sample frequencies up to the PHz regime [40] and is used here to reconstruct pulses out of CH0. For this experiment, the NPS sample is made of a 1 mm-thick SiO_2 where two gold electrodes are attached at two opposite sides. These are connected to two pre-amplifiers which are in turn connected to a lock-in amplifier that reads the difference between the current on the two electrodes.

The goal of these measurements is to demonstrate that IR synthesized fields can be used to inject carriers in the conduction band of solids in such a confined fashion that even frequencies in the UV spectral range of light can be field resolved.

Because of the highly nonlinear injection of charges, only the most intense peaks of the injecting field contribute to the generation of the electron wavepacket. Different peaks can potentially inject different wavepackets at different times, resulting in their interference and in a more complex response function. It follows that NPS works more efficiently when the injecting field has a dominant half cycle. In other words, this means that the injecting pulse needs to be a cosine pulse compressed down to a single cycle. The synthesized pulse shown in Figure 4.12a fulfils both criteria. From this trace, it is possible to calculate the total injection and the injection rate in the sample. The results are shown in Figure 4.17 and demonstrate the high degree of confinement of injection which occurs within 0.5 fs. To achieve the same result in the laboratory, we first performed an EOS measurement of each channel, verified that the channels were well compressed and, finally, replaced the EOS crystal with the NPS sample. Now the optimization of the injection is performed by doing a dispersion scan (d-scan), which consists of recording the induced current on one of the electrodes as a function of wedge position. The readout allows for the retrieval of both compression and CEP of the injecting field. The first quantity is indeed proportional to

the width of the envelope and the absolute CEP by the phase of the readout. The results are shown in Figure 4.18. Once found the maximum, in this case, we are sure that the pulses are well compressed and have the same global phase. The readout also confirms that each channel, separately, can induce a current in the sample.

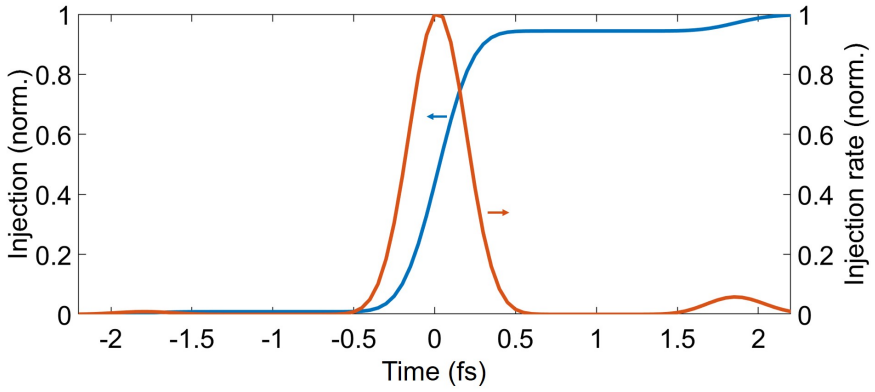

Figure 4.17: NPS calculated injection. The two plots show how the injection and its rate, blue and orange line, respectively, change as a function of time in the NPS sample due to the synthesized pulses. The trace in Figure 4.12a has been used to obtain the injection rate. The blue line is instead the cumulative rate of injection. From this plot, it emerges how the injection can be potentially limited to less than 0.5 fs. Figure provided by Dmitry Zimin [146] and adapted from [101])

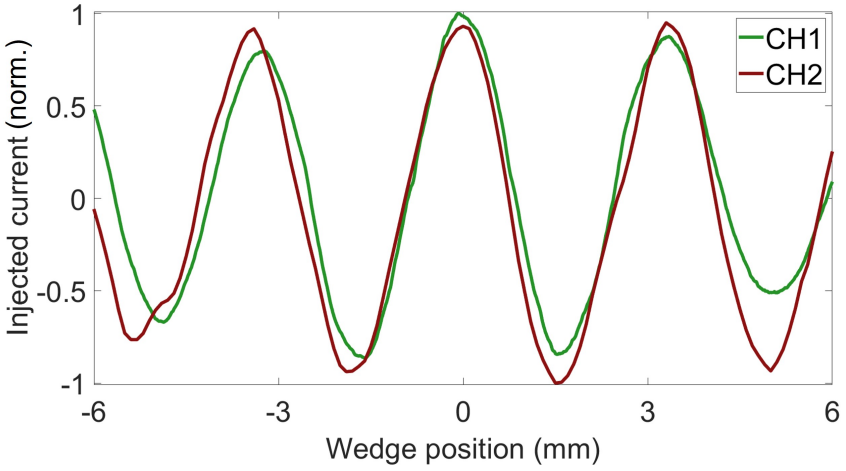

Figure 4.18: D-scan of CH1 and CH2. The green and red line show respectively a wedge scan performed for CH1 and CH2. The readout gives access to both the global phase and compression of the two channels. By positioning the wedges at the maximum signal of the field envelope, it is possible to obtain the shortest injection for each channel. Figure adapted from [101]

To perform field sensitive measurements with NPS it is necessary to set the laser polarization such that the field can steer the electrons towards the electrodes. The measurements presented above have been performed with these settings and the same configuration is now used to obtain the current injected by the synthesized pulses. The schematic (1) of Figure 4.19a illustrates what just mentioned. It is possible to obtain and optimise the total injected current by using the readout from just one electrode and scanning the relative arrival time of CH1 and CH2 (Δt). When Δt=0 the highest degree of injection is achieved as shown in Figure 4.19b.

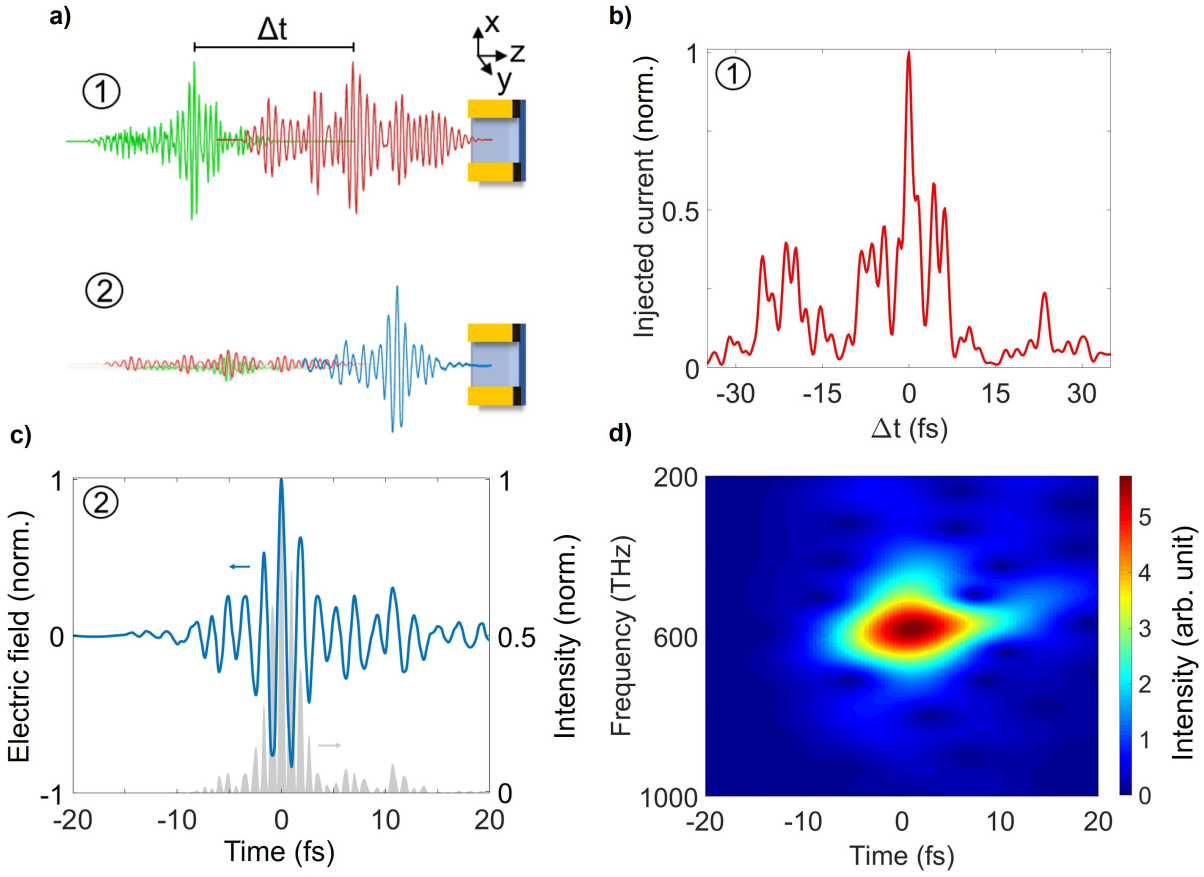

Figure 4.19: Ultrashort electron wavepacket injection and NPS characterization of CH0. (a) shows the two configurations used to obtain the results in (b) and (c). To inject the shortest possible wavepacket, the time delay (Δt) between CH1 and CH2 is changed until the highest current is achieved (b). (c) The injected carriers can be used to resolve the optical frequencies of the blue channel via NPS. In (d) is plotted the Gabor transform of the pulse in (c). Figure adapted from [101]

The idea is now to use the confined electron wavepacket generated by the synthesized pulses at Δt=0 to sample the electric field of CH0 via NPS. Keeping this in mind, we now want the synthesized pulses to only inject and CH0 to act purely as driving field. This can be achieved by setting the synthesized pulses polarization parallel, while the one of CH0 orthogonal to the electrodes, as illustrated in (2) of Figure 4.19a. Furthermore, to avoid injection coming from CH0, its intensity is reduced until no current is detected when the synthesised beam is blocked.

The NPS measurements of CH0 are shown in Figure 4.19c (blue line). The grey line shows the electric field squared. The 2D plot in Figure 4.19d is the Gabor transform of the field in 4.19c. This proves that CH0 does not present any strong high order dispersion. Its pulse duration is indeed 2.8 fs, close to its Fourier limit of 1.9 fs. From the Gabor transform it can be observed that frequencies around 900 THz can be field-resolved, proving that the injection occurs within 0.5 fs.

The information contained in the phase of CH0 can now be used to retrieve the EOS spectral response (Fig. 4.20). The details on how this quantity is calculated are described in the theoretical chapter in 1.3.2. The spectral response is crucial to obtain how the pulses look in free space, just before the EOS crystal. With this information we can therefore know the exact field that impinges on a sample and we can in turn use this information to correct the readout of the EOS. The EOS response function is applied to all the EOS pulses shown in this work.

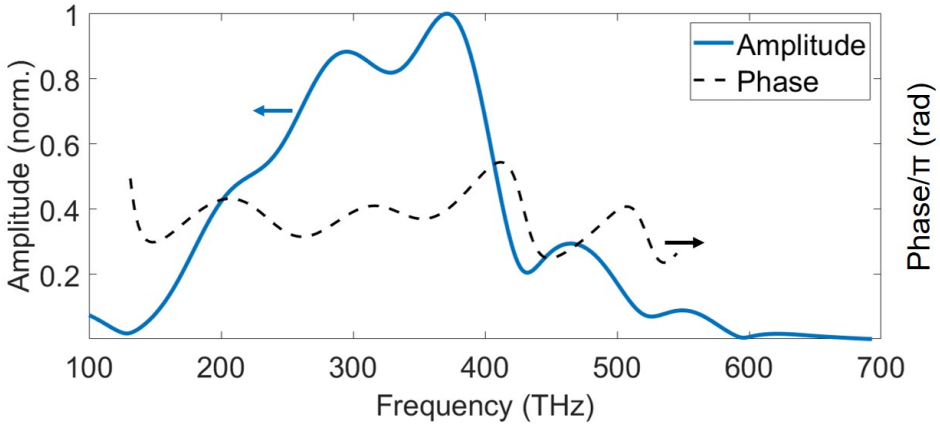

Figure 4.20: Response function of EOS. The amplitude (blue line) and the phase (dashed grey line) of the EOS spectral response can be obtained by combining the information of the field of CH0 obtained via NPS with the spectral response of the components used in the EOS setup. Figure adapted from [101]

4.4 Concluding remarks

This chapter started with introducing an OPCPA source and then moved to the description of a multi-channel synthesizer pumped by the OPCPA. The synthesizer was optimized for stable operation, and allowed the efficient and stable generation of 3.8 fs pulses. The table below summarises the main features of the three channels. In the system presented here each component and detection technique is strongly related to each other, resulting in a unique platform that can be used to carry few-fs experiments on thin samples. In this chapter, the application was focused on thin quartz. Nevertheless, the platform is not limited to the study of solids but can also be used to investigate liquid and gas jets. Though the synthesized pulses are made by the combination of CH1 and CH2 it would be possible to implement a configuration where all three channels form a unique pulse. The detection should rely on NPS rather than on EOS, given the spectral limits of the last. The injection would still be performed using the synthesized pulses but the driving would be instead provided by all the three channels combined.

The results presented here could not be achieved without a versatile and sensitive field-sensitive detection as EOS. The spectral limits of this technique have been extended here up to the visible (455 THz) overcoming the previous limits (250 THz) by a factor of two [13].

	Channel 0 (CH0)	**Channel 1 (CH1)**	**Channel 2 (CH2)**	**Synthesized (CH1+CH2)**
Bandwidth	300-600 nm	600-1500 nm	1500-3000 nm	600-3000 nm
Pulse duration	2.8 ± 0.1 fs	4.8 ± 0.3 fs	10.8 ± 0.6 fs	3.8 ± 0.2 fs
Fourier limit	1.9 fs	4.2 fs	7.2 fs	3.3 fs

Table 4.1: The table displays the measured pulse durations for the pulses in the first row and compares them with their Fourier limits.

Chapter 5

Conclusions

The work presented in this dissertation has been motivated by the unique phenomena that unfold when matter interacts with single-cycle pulses. Special attention has been given to effects where the shape and symmetry of electric fields, rather than their envelope, play a role. The samples under study have been argon, nitrogen and ammonia in the gas phase. In particular, this research has been focused on the dynamics ensuing from impulsive ionization. Combined with EOS detection, the platform presented here gives access to the direct emission of ions and highly excited electronic states. The study of electron dynamics and vibrations is carried out with tools different from more conventional ones like photoelectron spectroscopy and XUV radiation. This comes with advantages and disadvantages. For example, in the case of argon, the system presented here is limited to the detection of beatings between two states and does not allow for the unequivocal assignment of each one independently. On the other hand, this method offers a fast (15 minutes per scan) and sensitive detection (50 dB dynamic range) with a temporal resolution of a few femtoseconds, the latter greatly exceeding the resolution required to resolve the dynamics under study.

Most of the research carried out in field-resolved spectroscopy is performed at low intensities to linearly trigger effects that can be described with a perturbative approach. In this work the strength of the fields involved falls into the nonperturbative regime, making the understanding of the physics behind the observed radiation more complex to interpret but, at the same time, offering the possibility to generate and observe new effects compared to previous studies.

The results presented here for argon show that it is possible to detect radiation on the scale of a few tens of femtoseconds after an ionizing pump pulse. The induced radiation spans the spectral region from 30 to 80 THz, with the main observed features at 40, 60 and 75 THz. Previous works and simulations have been used to attribute the features to highly excited Rydberg states. The emission has been explained in terms of frustrated ionization [147]. A quick comparison with molecular nitrogen gives a hint of the potentiality of the technique that can be further investigated.

The same setup has also been employed to obtain preliminary results on ammonia molecules. These have been impulsively ionized and the emission from the cations success-

fully detected. This has been demonstrated to occur around 894 cm^{-1} which agrees with previous results presented in the literature. The factors that allowed the identification of these components have been the intensity scaling of the different features and the CEP of the pump pulses. The last dependency reveals that it is possible to influence the coherence of the cations in the focus by changing the symmetry of the pump pulses.

Both experiments would greatly benefit from a platform where a higher degree of control can be exerted on the pump pulses. A system that can achieve this control is presented in chapter 4, a three-channel waveform synthesizer.

To summarise the results presented here, a light transient in the vis-IR is synthesized from two channels and measured via EOS, using the vis-UV channel as a sampling pulse. The synthesized transient is sufficiently short to act as an injection pulse and to fully determine the electric field of the vis-UV channel through NPS. This procedure provides a full characterisation of all three channels and opens up possibilities for attosecond-resolution pump-probe measurements featuring control of the dynamics with tailored electric fields [148, 149, 150, 151]. We have demonstrated that EOS can successfully be applied to resolve fields in the visible spectrum of light [121], pushing the limits of EOS bandwidth by a factor of two compared to the previous record [13]. We have been able to systematically resolve optical frequencies from 700 to 2700 nm in a single trace. This allowed us to have active control over the shape of synthesized pulses as short as 3.8 fs at 1.7 μm. We also applied these light transients to inject attosecond electron wave-packets and access the PHz-frequency oscillations in a broadband optical field spanning from 300 to 600 nm. As a next step, we want to employ the fine-tunable synthesized pulses to study molecular dynamics, like the ones studied in chapter 3 on ammonia. The use of ultrabroad pulses for field-resolved spectroscopy has the advantage of confining the interaction to a limited time interval. On the other hand, it is not possible to select the states involved in the interaction because of the broadband spectrum of the pulses. The molecules, therefore, are not resonantly excited to an intermediate state how it happens for example for synchrotron radiation [152] and tunable laser sources [153]. The high intensity of the pulses though comes in our help. The sudden ionization indeed brings the molecule to a final state which does not dependent on the exact frequency components of the pump but rather on the molecular system itself. Nevertheless, the central wavelength of the pulse affects the way the molecule is ionized. Longer wavelengths favour tunnel ionization while shorter wavelengths multiphoton ionization. The first does not depend on higher electronically excited states but only on the shape of the potential barrier, while the last process is highly enhanced when an intermediate state is involved in the transition. The three channels of the synthesizer can be coupled in different combinations to obtain two-octave pulses with different central wavelengths. This could potentially lead to a platform where the coherent control of molecular dynamics can be achieved over several octaves with sub-cycle pulses.

Appendix A
List of Author's Publications

1. **E. Ridente**, M. Weidman*, M. Mamaikin, C. Jakubeit, F. Krausz, and N. Karpowicz*. (2020): "Hybrid phase-matching for optical parametric amplification of few-cycle infrared pulses", Optica 7(9):1093-1096

2. D. Haffa*, J. Bin*, M. Speicher*, K. Allinger, J. Hartmann, C. Kreuzer, **E. Ridente**, T.M. Ostermayr, and J. Schreiber. (2019): "Temporally Resolved Intensity Contouring (TRIC) for characterization of the absolute spatio-temporal intensity distribution of a relativistic, femtosecond laser pulse", Scientific Reports 9(1)

3. D. Haffa*, R. Yang*, J. Bin, S. Lehrack, F.E. Brack, H. Ding, F.S. Englbrecht, Y. Gao, J. Gebhard, M. Gilljohann, J. Goetzfried, J. Hartmann, S. Herr, P. Hilz, S.D. Kraft, C. Kreuzer, F. Kroll, F.H. Lindner, J. Metzkes, T.M. Ostermayr, **E. Ridente**, T.F. Roesch1, G. Schilli, H.-P. Schlenvoigt, M. Speicher, D. Taray, M. Wuerl1, K. Zeil, U. Schramm, S. Karsch, K. Parodi, P.R. Bolton, W. Assmann and J. Schreiber. (2019): "I-BEAT: Ultrasonic method for online measurement of the energy distribution of a single ion bunch", Scientific Reports 9(1)

4. **E. Ridente**, O. Razskazovskaya, M. Mamikin, N. Altwaijry, M.F. Kling, M. Weidman, F. Krausz, and N. Karpowicz*: "Electro-optic characterization of synthesized infrared-visible light fields", submitted to Nature Communication

5. M. Mamaikin, Y.-L. Li, **E. Ridente**, W.T. Chen, J.-S. Park, A.Y. Zhu, F. Capasso, M. Weidman, M. Schultze, F. Krausz, and N. Karpowicz*: "Electric-field-resolved near infrared microscopy", submitted to Nature Communication

6. M. Mamaikin, **E. Ridente**, Y.-L. Li, M. Weidman, F. Krausz, and N. Karpowicz. "Contrast enhancement in near-infrared electro-optic imaging", in preparation.

Appendix B
Data Archiving

The experimental raw data, evaluation files, data processing scripts, and original figures can be found on the Data Archive Server of the Laboratory for Attosecond Physics at the Max Planck Institute of Quantum Optics: `//AFS/ipp-garching.mpg.de/mpq/lap/publication_archive`. All the figures in this thesis are organised in separate folders following the order of the chapters.

Each dedicated folder contains figures in .png or .pptx format, raw data and Matlab scripts if needed. The auxiliary set of scripts required for data analysis is located in the individual folder. The table below gives an overview of the figures.

Figure 1.1	schematic plot (.png) and generating script (.m)
Figure 1.2	schematic plot (.pptx)
Figure 1.3	schematic plot (.pptx)
Figure 1.4	schematic plot (.pptx)
Figure 1.5	schematic plot (.pptx)
Figure 1.6	schematic plot (.pptx)
Figure 1.7	schematic plot (.pptx)
Figure 1.8	schematic plot (.pptx)
Figure 1.9	schematic plot (.pptx)
Figure 1.10	schematic plot (.pptx)
Figure 2.1	schematic plot (.png), generating script (.m), and raw data.
Figure 2.2	schematic plot (.png), generating script (.m), and raw data.
Figure 2.3	schematic plot (.png), generating script (.m), and raw data.
Figure 2.4	schematic plot (.png), generating script (.m), and raw data.
Figure 2.5	schematic plot (.png), generating script (.m), and raw data.
Figure 2.6	schematic plot (.ppxt)
Figure 2.7	schematic plot (.png), generating script (.m), and raw data.
Figure 2.8	schematic plot (.png), generating script (.m), and raw data.
Figure 2.9	schematic plot (.png), generating script (.m), and raw data.
Figure 2.10	schematic plot (.jpg)
Figure 2.11	schematic plot (.png), generating script (.m), and raw data.

Figure 2.12	schematic plot (.png), generating script (.m), and raw data.
Figure 3.1	schematic plot (.pptx), generating script (.m), and raw data.
Figure 3.2	schematic plot (.pptx), generating script (.m), and raw data.
Figure 3.3	schematic plot (.png), generating script (.m), and raw data.
Figure 3.4	schematic plot (.png), generating script (.m), and raw data.
Figure 3.5	schematic plot (.png), generating script (.m), and raw data.
Figure 3.6	schematic plot (.png), generating script (.m), and raw data.
Figure 4.1	schematic from [100]
Figure 4.2	schematic from [100]
Figure 4.3	schematic from [100]
Figure 4.4	schematic from [100]
Figure 4.5	schematic from [100]
Figure 4.6	schematic from [101]
Figure 4.7	schematic from [101]
Figure 4.8	schematic plot (.png), generating script (.m), and raw data.
Figure 4.9	schematic from [101]
Figure 4.10	schematic from [101]
Figure 4.11	schematic plot (.png), generating script (.m), and raw data.
Figure 4.12	schematic plot (.png), generating script (.m), and raw data.
Figure 4.13	schematic plot (.pdf), generating script (.m), and raw data.
Figure 4.14	schematic from [101]
Figure 4.15	schematic plot (.pdf), generating script (.m), and raw data.
Figure 4.16	schematic from [145]
Figure 4.17	schematic from [146]
Figure 4.18	schematic from [101]
Figure 4.19	schematic from [101]
Figure 4.20	schematic from [101]

Bibliography

[1] A. R. Beck, D. M. Neumark, and S. R. Leone. "Probing ultrafast dynamics with attosecond transient absorption". In: *Chemical Physics Letters* 624 (2015), pp. 119–130.

[2] Y. R. Lee, D. W. Kang, H. L. Kim, and C. H. Kwon. "One-photon mass-analyzed threshold ionization (MATI) spectroscopy of pyridine: Determination of accurate ionization energy and cationic structure". In: *The Journal of chemical physics* 141.17 (2014), p. 174303.

[3] T. Suzuki. "Time-resolved photoelectron spectroscopy of non-adiabatic electronic dynamics in gas and liquid phases". In: *International Reviews in Physical Chemistry* 31.2 (2012), pp. 265–318.

[4] E. J. Bieske and O. Dopfer. "High-resolution spectroscopy of cluster ions". In: *Chemical Reviews* 100.11 (2000), pp. 3963–3998.

[5] S.-Y. Ding, J. Yi, J.-F. Li, B. Ren, D.-Y. Wu, R. Panneerselvam, and Z.-Q. Tian. "Nanostructure-based plasmon-enhanced Raman spectroscopy for surface analysis of materials". In: *Nature Reviews Materials* 1.6 (2016), pp. 1–16.

[6] A. H. Zewail. "Femtochemistry". In: *Femtochemistry: Ultrafast Dynamics of the Chemical Bond: Volume I*. World Scientific, 1994, pp. 3–22.

[7] P. Brumer and M. Shapiro. "Coherence chemistry: controlling chemical reactions [with lasers]". In: *Accounts of Chemical Research* 22.12 (1989), pp. 407–413.

[8] M. Schultze, E. M. Bothschafter, A. Sommer, S. Holzner, W. Schweinberger, M. Fiess, M. Hofstetter, R. Kienberger, V. Apalkov, V. S. Yakovlev, et al. "Controlling dielectrics with the electric field of light". In: *Nature* 493.7430 (2013), pp. 75–78.

[9] F. Krausz and M. I. Stockman. "Attosecond metrology: from electron capture to future signal processing". In: *Nature Photonics* 8.3 (2014), pp. 205–213.

[10] H. Wang, M. Chini, S. Chen, C.-H. Zhang, F. He, Y. Cheng, Y. Wu, U. Thumm, and Z. Chang. "Attosecond time-resolved autoionization of argon". In: *Physical review letters* 105.14 (2010), p. 143002.

[11] Q. Wu and X.-C. Zhang. "Free-space electro-optic sampling of terahertz beams". In: *Applied Physics Letters* 67.24 (1995), pp. 3523–3525.

[12] A. Sell, R. Scheu, A. Leitenstorfer, and R. Huber. "Field-resolved detection of phase-locked infrared transients from a compact Er: fiber system tunable between 55 and 107 THz". In: *Applied Physics Letters* 93.25 (2008), p. 251107.

[13] S. Keiber, S. Sederberg, A. Schwarz, M. Trubetskov, V. Pervak, F. Krausz, and N. Karpowicz. "Electro-optic sampling of near-infrared waveforms". In: *Nature Photonics* 10.3 (2016), pp. 159–162.

[14] V. Pervak, I. Ahmad, M. K. Trubetskov, A. V. Tikhonravov, and F. Krausz. "Double-angle multilayer mirrors with smooth dispersion characteristics". In: *Opt. Express* 17.10 (May 2009), pp. 7943–7951.

[15] S. Divitt, W. Zhu, C. Zhang, H. J. Lezec, and A. Agrawal. "Ultrafast optical pulse shaping using dielectric metasurfaces". In: *Science* 364.6443 (2019), pp. 890–894.

[16] S. Yefet and A. Pe'er. "A Review of Cavity Design for Kerr Lens Mode-Locked Solid-State Lasers". In: *Applied Sciences* 3.4 (2013), pp. 694–724.

[17] V. Pervak, M. Trubetskov, and A. Tikhonravov. "Design consideration for high damage threshold UV-Vis-IR mirrors". In: *Laser-Induced Damage in Optical Materials: 2009*. Vol. 7504. International Society for Optics and Photonics. 2009, 75040A.

[18] V. Pervak, F. Krausz, and A. Apolonski. "Hafnium oxide thin films deposited by reactive middle-frequency dual-magnetron sputtering". In: *Thin Solid Films* 515.20-21 (2007), pp. 7984–7989.

[19] R. W. Boyd. *Nonlinear optics*. Academic press, 2020.

[20] I. Amat-Roldán, I. G. Cormack, P. Loza-Alvarez, E. J. Gualda, and D. Artigas. "Ultrashort pulse characterisation with SHG collinear-FROG". In: *Optics express* 12.6 (2004), pp. 1169–1178.

[21] M. Anderson, A. Monmayrant, S.-P. Gorza, P. Wasylczyk, and I. A. Walmsley. "SPIDER: A decade of measuring ultrashort pulses". In: *Laser Physics Letters* 5.4 (2008), p. 259.

[22] C. Manzoni, O. D. Mücke, G. Cirmi, S. Fang, J. Moses, S.-W. Huang, K.-H. Hong, G. Cerullo, and F. X. Kärtner. "Coherent pulse synthesis: towards sub-cycle optical waveforms". In: *Laser & Photonics Reviews* 9.2 (2015), pp. 129–171.

[23] K. Meyer, M. Pessot, G. Mourou, R. Grondin, and S. Chamoun. "Subpicosecond photoconductivity overshoot in gallium arsenide observed by electro-optic sampling". In: *Applied physics letters* 53.23 (1988), pp. 2254–2256.

[24] J. Shan, A. S. Weling, E. Knoesel, L. Bartels, M. Bonn, A. Nahata, G. A. Reider, and T. F. Heinz. "Single-shot measurement of terahertz electromagnetic pulses by use of electro-optic sampling". In: *Optics letters* 25.6 (2000), pp. 426–428.

[25] C. Kübler, R. Huber, S. Tübel, and A. Leitenstorfer. "Ultrabroadband detection of multi-terahertz field transients with GaSe electro-optic sensors: Approaching the near infrared". In: *Applied physics letters* 85.16 (2004), pp. 3360–3362.

[26] M. Porer, J.-M. Ménard, and R. Huber. "Shot noise reduced terahertz detection via spectrally postfiltered electro-optic sampling". In: *Optics letters* 39.8 (2014), pp. 2435–2438.

[27] C. Riek, D. Seletskiy, A. S. Moskalenko, J. Schmidt, P. Krauspe, S. Eckart, S. Eggert, G. Burkard, and A. Leitenstorfer. "Direct sampling of electric-field vacuum fluctuations". In: *Science* 350.6259 (2015), pp. 420–423.

[28] I. Pupeza, M. Huber, M. Trubetskov, W. Schweinberger, S. A. Hussain, C. Hofer, K. Fritsch, M. Poetzlberger, L. Vamos, E. Fill, et al. "Field-resolved infrared spectroscopy of biological systems". In: *Nature* 577.7788 (2020), pp. 52–59.

[29] A. Leitenstorfer, S. Hunsche, J. Shah, M. Nuss, and W. Knox. "Detectors and sources for ultrabroadband electro-optic sampling: Experiment and theory". In: *Applied physics letters* 74.11 (1999), pp. 1516–1518.

[30] M. Tani, M. Herrmann, and K. Sakai. "Generation and detection of terahertz pulsed radiation with photoconductive antennas and its application to imaging". In: *Measurement science and technology* 13.11 (2002), p. 1739.

[31] M. Ashida. "Ultra-broadband terahertz wave detection using photoconductive antenna". In: *Japanese Journal of Applied Physics* 47.10S (2008), p. 8221.

[32] Q. Wu and X.-C. Zhang. "Ultrafast electro-optic field sensors". In: *Applied physics letters* 68.12 (1996), pp. 1604–1606.

[33] R. Akbari and A. Major. "Optical, spectral and phase-matching properties of BIBO, BBO and LBO crystals for optical parametric oscillation in the visible and near-infrared wavelength ranges". In: *Laser Physics* 23.3 (2013), p. 035401.

[34] K. T. Kim, C. Zhang, A. D. Shiner, B. E. Schmidt, F. Légaré, D. Villeneuve, and P. Corkum. "Petahertz optical oscilloscope". In: *Nature Photonics* 7.12 (2013), pp. 958–962.

[35] A. S. Wyatt, T. Witting, A. Schiavi, D. Fabris, P. Matia-Hernando, I. A. Walmsley, J. P. Marangos, and J. W. Tisch. "Attosecond sampling of arbitrary optical waveforms". In: *Optica* 3.3 (2016), pp. 303–310.

[36] S. B. Park, K. Kim, W. Cho, S. I. Hwang, I. Ivanov, C. H. Nam, and K. T. Kim. "Direct sampling of a light wave in air". In: *Optica* 5.4 (2018), pp. 402–408.

[37] M. Garg, M. Zhan, T. T. Luu, H. Lakhotia, T. Klostermann, A. Guggenmos, and E. Goulielmakis. "Multi-petahertz electronic metrology". In: *Nature* 538.7625 (2016), pp. 359–363.

[38] A. Schiffrin, T. Paasch-Colberg, N. Karpowicz, V. Apalkov, D. Gerster, S. Mühlbrandt, M. Korbman, J. Reichert, M. Schultze, S. Holzner, et al. "Optical-field-induced current in dielectrics". In: *Nature* 493.7430 (2013), pp. 70–74.

[39] G. Vampa, T. Hammond, M. Taucer, X. Ding, X. Ropagnol, T. Ozaki, S. Delprat, M. Chaker, N. Thiré, B. Schmidt, et al. "Strong-field optoelectronics in solids". In: *Nature Photonics* 12.8 (2018), pp. 465–468.

[40] S. Sederberg, D. Zimin, S. Keiber, F. Siegrist, M. S. Wismer, V. S. Yakovlev, I. Floss, C. Lemell, J. Burgdörfer, M. Schultze, et al. "Attosecond optoelectronic field measurement in solids". In: *Nature communications* 11.1 (2020), pp. 1–8.

[41] P. B. Corkum. "Plasma perspective on strong field multiphoton ionization". In: *Physical review letters* 71.13 (1993), p. 1994.

[42] R. Santra and A. Gordon. "Three-Step Model for High-Harmonic Generation in Many-Electron Systems". In: *Phys. Rev. Lett.* 96 (7 Feb. 2006), p. 073906.

[43] T. Brabec and F. Krausz. "Intense few-cycle laser fields: Frontiers of nonlinear optics". In: *Reviews of Modern Physics* 72.2 (2000), p. 545.

[44] J. L. Krause, K. J. Schafer, and K. C. Kulander. "High-order harmonic generation from atoms and ions in the high intensity regime". In: *Physical Review Letters* 68.24 (1992), p. 3535.

[45] L. He, Z. Wang, Y. Li, Q. Zhang, P. Lan, and P. Lu. "Wavelength dependence of high-order-harmonic yield in inhomogeneous fields". In: *Physical Review A* 88.5 (2013), p. 053404.

[46] H. Vincenti and F. Quéré. "Attosecond lighthouses: how to use spatiotemporally coupled light fields to generate isolated attosecond pulses". In: *Physical review letters* 108.11 (2012), p. 113904.

[47] M. Hentschel, R. Kienberger, C. Spielmann, G. A. Reider, N. Milosevic, T. Brabec, P. Corkum, U. Heinzmann, M. Drescher, and F. Krausz. "Attosecond metrology". In: *Nature* 414.6863 (2001), pp. 509–513.

[48] S. Gilbertson, M. Chini, X. Feng, S. Khan, Y. Wu, and Z. Chang. "Monitoring and controlling the electron dynamics in helium with isolated attosecond pulses". In: *Physical review letters* 105.26 (2010), p. 263003.

[49] M. F. Kling and M. J. Vrakking. "Attosecond electron dynamics". In: *Annu. Rev. Phys. Chem.* 59 (2008), pp. 463–492.

[50] X.-M. Tong, Z. Zhao, and C.-D. Lin. "Theory of molecular tunneling ionization". In: *Physical Review A* 66.3 (2002), p. 033402.

[51] N. Šibalić and C. S. Adams. *Rydberg physics*. IOP Publishing, 2018.

[52] S. D. Hogan. "Rydberg-Stark deceleration of atoms and molecules". In: *EPJ Techniques and Instrumentation* 3 (2016), pp. 1–50.

[53] J. A. Sedlacek, A. Schwettmann, H. Kübler, R. Löw, T. Pfau, and J. P. Shaffer. "Microwave electrometry with Rydberg atoms in a vapour cell using bright atomic resonances". In: *Nature Physics* 8.11 (2012), pp. 819–824.

[54] C. G. Wade, N. Šibalić, N. R. de Melo, J. M. Kondo, C. S. Adams, and K. J. Weatherill. "Real-time near-field terahertz imaging with atomic optical fluorescence". In: *Nature Photonics* 11.1 (2017), pp. 40–43.

[55] J. D. Pritchard, D. Maxwell, A. Gauguet, K. J. Weatherill, M. Jones, and C. S. Adams. "Cooperative atom-light interaction in a blockaded Rydberg ensemble". In: *Physical review letters* 105.19 (2010), p. 193603.

[56] X. He, B. Li, A. Chen, and C. Zhang. "Model-potential calculation of lifetimes of Rydberg states of alkali atoms". In: *Journal of Physics B: Atomic, Molecular and Optical Physics* 23.4 (1990), p. 661.

[57] R. Heidemann, U. Raitzsch, V. Bendkowsky, B. Butscher, R. Löw, and T. Pfau. "Rydberg excitation of Bose-Einstein condensates". In: *Physical Review Letters* 100.3 (2008), p. 033601.

[58] T. R. Gentile, B. J. Hughey, D. Kleppner, and T. W. Ducas. "Microwave spectroscopy of calcium Rydberg states". In: *Physical Review A* 42.1 (1990), p. 440.

[59] C. T. Wittwer, M. G. Herrmann, A. A. Moss, and R. P. Rasmussen. "Continuous fluorescence monitoring of rapid cycle DNA amplification". In: *Biotechniques* 22.1 (1997), pp. 130–138.

[60] Y. Nishijima. "Fluorescence methods in polymer science". In: *Journal of Polymer Science Part C: Polymer Symposia*. Vol. 31. 1. Wiley Online Library. 1970, pp. 353–373.

[61] C. Xu, W. Zipfel, J. B. Shear, R. M. Williams, and W. W. Webb. "Multiphoton fluorescence excitation: new spectral windows for biological nonlinear microscopy". In: *Proceedings of the National Academy of Sciences* 93.20 (1996), pp. 10763–10768.

[62] Y.-X. Yan, E. B. Gamble Jr, and K. A. Nelson. "Impulsive stimulated scattering: General importance in femtosecond laser pulse interactions with matter, and spectroscopic applications". In: *The Journal of chemical physics* 83.11 (1985), pp. 5391–5399.

[63] L. Dhar, J. A. Rogers, and K. A. Nelson. "Time-resolved vibrational spectroscopy in the impulsive limit". In: *Chemical Reviews* 94.1 (1994), pp. 157–193.

[64] G. P. Wiederrecht, T. P. Dougherty, L. Dhar, K. A. Nelson, D. Leaird, and A. Weiner. "Explanation of anomalous polariton dynamics in LiTaO 3". In: *Physical Review B* 51.2 (1995), p. 916.

[65] S. Ruhman, A. Joly, B. Kohler, L. Williams, and K. Nelson. "Intramolecular and intermolecular dynamics in molecular liquids through femtosecond time-resolved impulsive stimulated scattering". In: *Revue de physique appliquée* 22.12 (1987), pp. 1717–1734.

[66] V. S. Batista and P. Brumer. "Semiclassical dynamics in the coherent control of nonadiabatic ICN photodissociation". In: *The Journal of Physical Chemistry A* 105.12 (2001), pp. 2591–2598.

[67] J. Herek, A. Materny, and A. Zewail. "Femtosecond control of an elementary unimolecular reaction from the transition-state region". In: *Chemical physics letters* 228.1-3 (1994), pp. 15–25.

[68] V. Lozovoy, O. Sarkisov, A. Vetchinkin, and S. Y. Umanskii. "Coherent control of the molecular iodine vibrational dynamics by chirped femtosecond light pulses: theoretical simulation of the pump-probe experiment". In: *Chemical physics* 243.1-2 (1999), pp. 97–114.

[69] E. W. Schlag. "ZEKE spectroscopy". In: (1998).

[70] C. E. Dessent, S. R. Haines, and K. Müller-Dethlefs. "A new detection scheme for synchronous, high resolution ZEKE and MATI spectroscopy demonstrated on the Phenol· Ar complex". In: *Chemical Physics Letters* 315.1-2 (1999), pp. 103–108.

[71] M. C. Cockett. "Photoelectron spectroscopy without photoelectrons: Twenty years of ZEKE spectroscopy". In: *Chemical Society Reviews* 34.11 (2005), pp. 935–948.

[72] M. Clerici, M. Peccianti, B. E. Schmidt, L. Caspani, M. Shalaby, M. Giguere, A. Lotti, A. Couairon, F. Légaré, T. Ozaki, et al. "Wavelength scaling of terahertz generation by gas ionization". In: *Physical Review Letters* 110.25 (2013), p. 253901.

[73] I. Babushkin, W. Kuehn, C. Köhler, S. Skupin, L. Bergé, K. Reimann, M. Woerner, J. Herrmann, and T. Elsaesser. "Ultrafast spatiotemporal dynamics of terahertz generation by ionizing two-color femtosecond pulses in gases". In: *Physical review letters* 105.5 (2010), p. 053903.

[74] N. Karpowicz, X. Lu, and X.-C. Zhang. "Terahertz gas photonics". In: *Journal of Modern Optics* 56.10 (2009), pp. 1137–1150.

[75] P. U. Jepsen, R. H. Jacobsen, and S. Keiding. "Generation and detection of terahertz pulses from biased semiconductor antennas". In: *JOSA B* 13.11 (1996), pp. 2424–2436.

[76] A. Nahata, A. S. Weling, and T. F. Heinz. "A wideband coherent terahertz spectroscopy system using optical rectification and electro-optic sampling". In: *Applied physics letters* 69.16 (1996), pp. 2321–2323.

[77] K.-Y. Kim, J. H. Glownia, A. J. Taylor, and G. Rodriguez. "High-power broadband terahertz generation via two-color photoionization in gases". In: *IEEE Journal of Quantum Electronics* 48.6 (2012), pp. 797–805.

[78] M. Kreß, T. Löffler, M. D. Thomson, R. Dörner, H. Gimpel, K. Zrost, T. Ergler, R. Moshammer, U. Morgner, J. Ullrich, et al. "Determination of the carrier-envelope phase of few-cycle laser pulses with terahertz-emission spectroscopy". In: *Nature physics* 2.5 (2006), pp. 327–331.

[79] A. Nahata and T. F. Heinz. "Detection of freely propagating terahertz radiation by use of optical second-harmonic generation". In: *Optics letters* 23.1 (1998), pp. 67–69.

[80] X. Lu, N. Karpowicz, and X.-C. Zhang. "Broadband terahertz detection with selected gases". In: *JOSA B* 26.9 (2009), A66–A73.

[81] C. Hofer, S. A. Hussain, W. Schweinberger, M. Huber, T. P. Butler, D. Gerz, N. Karpowicz, F. Krausz, and I. Pupeza. "Quantum-Efficiency and Bandwidth Optimized Electro-Optic Sampling". In: *The European Conference on Lasers and Electro-Optics*. Optical Society of America. 2019, cf_p_15.

[82] A. Diebold, F. Emaury, C. Schriber, M. Golling, C. J. Saraceno, T. Südmeyer, and U. Keller. "SESAM mode-locked Yb: CaGdAlO 4 thin disk laser with 62 fs pulse generation". In: *Optics letters* 38.19 (2013), pp. 3842–3845.

[83] T. Saule, S. Holzberger, O. De Vries, M. Plötner, J. Limpert, A. Tünnermann, and I. Pupeza. "Phase-stable, multi-μJ femtosecond pulses from a repetition-rate tunable Ti: Sa-oscillator-seeded Yb-fiber amplifier". In: *Applied Physics B* 123.1 (2017), pp. 1–7.

[84] T. Nubbemeyer, K. Gorling, A. Saenz, U. Eichmann, and W. Sandner. "Strong-field tunneling without ionization". In: *Physical review letters* 101.23 (2008), p. 233001.

[85] "Hitran database: https://hitran.org/".

[86] N. Zobov, S. Shirin, R. Ovsyannikov, O. Polyansky, S. Yurchenko, R. Barber, J. Tennyson, R. Hargreaves, and P. Bernath. "Analysis of high temperature ammonia spectra from 780 to 2100 cm- 1". In: *Journal of Molecular Spectroscopy* 269.1 (2011), pp. 104–108.

[87] N. L. Evans, H. Yu, G. M. Roberts, V. G. Stavros, and S. Ullrich. "Observation of ultrafast NH3 ($\tilde{A}$) state relaxation dynamics using a combination of time-resolved photoelectron spectroscopy and photoproduct detection". In: *Physical Chemistry Chemical Physics* 14.30 (2012), pp. 10401–10409.

[88] S. Yu, J. C. Pearson, B. J. Drouin, K. Sung, O. Pirali, M. Vervloet, M.-A. Martin-Drumel, C. P. Endres, T. Shiraishi, K. Kobayashi, et al. "Submillimeter-wave and far-infrared spectroscopy of high-J transitions of the ground and ν 2= 1 states of ammonia". In: *The Journal of chemical physics* 133.17 (2010), p. 174317.

[89] C. Léonard, N. C. Handy, S. Carter, and J. M. Bowman. "The vibrational levels of ammonia". In: *Spectrochimica Acta Part A: Molecular and Biomolecular Spectroscopy* 58.4 (2002), pp. 825–838.

[90] D. Edvardsson, P. Baltzer, L. Karlsson, B. Wannberg, D. Holland, D. Shaw, and E. Rennie. "A photoabsorption, photodissociation and photoelectron spectroscopy study of NH3 and ND3". In: *Journal of Physics B: Atomic, Molecular and Optical Physics* 32.11 (1999), p. 2583.

[91] C. Woywod, S. Scharfe, R. Krawczyk, W. Domcke, and H. Köppel. "Theoretical investigation of Jahn–Teller and pseudo-Jahn–Teller interactions in the ammonia cation". In: *The Journal of chemical physics* 118.13 (2003), pp. 5880–5893.

[92] J. Bacon and S. Pratt. "Photoelectron spectroscopy of ammonia: Mode-dependent vibrational autoionization". In: *The Journal of Chemical Physics* 113.17 (2000), pp. 7188–7196.

[93] G. Reiser, W. Habenicht, and K. Müller-Dethlefs. "Zero kinetic energy (ZEKE) photoelectron spectroscopy of ammonia by nonresonant two-photon ionization from the neutral ground state". In: *The Journal of chemical physics* 98.11 (1993), pp. 8462–8468.

[94] V. Stert, W. Radloff, T. Freudenberg, F. Noack, I. Hertel, C. Jouvet, C. Dedonder-Lardeux, and D. Solgadi. "Femtosecond time-resolved photoelectron spectra of ammonia molecules and clusters". In: *EPL (Europhysics Letters)* 40.5 (1997), p. 515.

[95] P. M. Kraus and H. J. Wörner. "Attosecond nuclear dynamics in the ammonia cation: Relation between high-harmonic and photoelectron spectroscopies". In: *Chem Phys Chem* 14.7 (2013), pp. 1445–1450.

[96] P. Sándor, V. Tagliamonti, A. Zhao, T. Rozgonyi, M. Ruckenbauer, P. Marquetand, and T. Weinacht. "Strong field molecular ionization in the impulsive limit: Freezing vibrations with short pulses". In: *Physical review letters* 116.6 (2016), p. 063002.

[97] H. Harde, J. Zhao, M. Wolff, R. Cheville, and D. Grischkowsky. "THz time-domain spectroscopy on ammonia". In: *The Journal of Physical Chemistry A* 105.25 (2001), pp. 6038–6047.

[98] J. Förster, E. Plésiat, A. Magana, and A. Saenz. "Imaging of the umbrella motion and tunneling in ammonia molecules by strong-field ionization". In: *Physical Review A* 94.4 (2016), p. 043405.

[99] J. Rabalais, L. Karlsson, L. Werme, T. Bergmark, and K. Siegbahn. "Analysis of vibrational structure and Jahn-Teller effects in the electron spectrum of ammonia". In: *The Journal of Chemical Physics* 58.8 (1973), pp. 3370–3372.

[100] E. Ridente, M. Weidman, M. Mamaikin, C. Jakubeit, F. Krausz, and N. Karpowicz. "Hybrid phase-matching for optical parametric amplification of few-cycle infrared pulses". In: *Optica* 7.9 (2020), pp. 1093–1096.

[101] E. Ridente, M. Mamaikin, N. Altwaijry, D. Zimin, M. F. Kling, V. Pervak, M. Weidman, F. Krausz, and N. Karpowicz. "Electro-optic characterization of synthesized infrared-visible light fields". In: *Nature Photonics (Submitted)* (2021).

[102] A. Kessel, V. E. Leshchenko, O. Jahn, M. Krüger, A. Münzer, A. Schwarz, V. Pervak, M. Trubetskov, S. A. Trushin, F. Krausz, Z. Major, and S. Karsch. "Relativistic few-cycle pulses with high contrast from picosecond-pumped OPCPA". In: *Optica* 5.4 (Apr. 2018), pp. 434–442.

[103] D. Rivas, A. Borot, D. Cardenas, G. Marcus, X. Gu, D. Herrmann, J. Xu, J. Tan, D. Kormin, G. Ma, et al. "Next generation driver for attosecond and laser-plasma physics". In: *Scientific reports* 7.1 (2017), pp. 1–8.

[104] R. Baumgartner and R. Byer. "Optical parametric amplification". In: *Quantum Electronics, IEEE Journal of* 15 (July 1979), pp. 432–444.

[105] B. Shan and Z. Chang. "Dramatic extension of the high-order harmonic cutoff by using a long-wavelength driving field". In: *Phys. Rev. A* 65 (1 Dec. 2001), p. 011804.

[106] T. C. Gunaratne, M. Milliken, J. R. Challa, and M. C. Simpson. "Tunable ultrafast infrared/visible laser to probe vibrational dynamics". In: *Appl. Opt.* 45.3 (Jan. 2006), pp. 558–564.

[107] G. Schweitzer, L. Xu, B. Craig, and F. C. DeSchryver. "A double OPA femtosecond laser system for transient absorption spectroscopy". In: *Optics Communications* 142.4 (1997), pp. 283–288. ISSN: 0030-4018.

[108] F. Silva, S. M. Teichmann, S. L. Cousin, M. Hemmer, and J. Biegert. "Spatiotemporal isolation of attosecond soft X-ray pulses in the water window". In: *Nature communications* 6.1 (2015), pp. 1–6.

[109] C. Zhang, G. Vampa, D. Villeneuve, and P. Corkum. "Attosecond lighthouse driven by sub-two-cycle, 1.8 μm laser pulses". In: *Journal of Physics B: Atomic, Molecular and Optical Physics* 48.6 (2015), p. 061001.

[110] L. von Grafenstein, M. Bock, D. Ueberschaer, K. Zawilski, P. Schunemann, U. Griebner, and T. Elsaesser. "5 μm few-cycle pulses with multi-gigawatt peak power at a 1 kHz repetition rate". In: *Opt. Lett.* 42.19 (Oct. 2017), pp. 3796–3799.

[111] Z. Heiner, V. Petrov, G. Steinmeyer, M. J. J. Vrakking, and M. Mero. "100-kHz, dual-beam OPA delivering high-quality, 5-cycle angular-dispersion-compensated mid-infrared idler pulses at 3.1 μm". In: *Opt. Express* 26.20 (Oct. 2018), pp. 25793–25804.

[112] V. Petrov, F. Seifert, and F. Noack. "Visible optical parametric generator producing nearly bandwidth-limited femtosecond light pulses at 1 -kHz repetition rate". In: *Appl. Opt.* 33.30 (Oct. 1994), pp. 6988–6991.

[113] T. Metzger, C. Y. Teisset, and F. Krausz. "High-repetition-rate picosecond pump laser based on an Yb:YAG disk amplifier for optical parametric amplification". In: *Advanced Solid-State Photonics*. Optical Society of America, 2008, TuA2.

[114] M. Mero, F. Noack, F. Bach, V. Petrov, and M. J. Vrakking. "High-average-power, 50-fs parametric amplifier front-end at 1.55 μm". In: *Optics express* 23.26 (2015), pp. 33157–33163.

[115] T. Fuji, N. Ishii, C. Y. Teisset, X. Gu, T. Metzger, A. Baltuska, N. Forget, D. Kaplan, A. Galvanauskas, and F. Krausz. "Parametric amplification of few-cycle carrier-envelope phase-stable pulses at 2.1 μm". In: *Optics letters* 31.8 (2006), pp. 1103–1105.

[116] N. Ishii, K. Kaneshima, K. Kitano, T. Kanai, S. Watanabe, and J. Itatani. "Sub-two-cycle, carrier-envelope phase-stable, intense optical pulses at 1.6 μm from a BiB3O6 optical parametric chirped-pulse amplifier". In: *Optics letters* 37.20 (2012), pp. 4182–4184.

[117] S. Wandel, G. Xu, Y. Yin, and I. Jovanovic. "Parametric generation of energetic short mid-infrared pulses for dielectric laser acceleration". In: *Journal of Physics B: Atomic, Molecular and Optical Physics* 47.23 (2014), p. 234016.

[118] H. Fattahi, A. Schwarz, S. Keiber, and N. Karpowicz. "Efficient, octave-spanning difference-frequency generation using few-cycle pulses in simple collinear geometry". In: *Optics letters* 38.20 (2013), pp. 4216–4219.

[119] Y. Deng, A. Schwarz, H. Fattahi, M. Ueffing, X. Gu, M. Ossiander, T. Metzger, V. Pervak, H. Ishizuki, T. Taira, et al. "Carrier-envelope-phase-stable, 1.2 mJ, 1.5 cycle laser pulses at 2.1 μm". In: *Optics letters* 37.23 (2012), pp. 4973–4975.

[120] C. Jakubeit. "High harmonic generation using a 2 μm OPCPA". PhD thesis. LMU, 2019.

[121] O. Razskazovskaya. "Infrared waveform synthesis for application in attosecond science". PhD thesis. Ludwig Maximilians Universität München, 2017.

[122] T. T. Luu, M. Garg, S. Y. Kruchinin, A. Moulet, M. T. Hassan, and E. Goulielmakis. "Extreme ultraviolet high-harmonic spectroscopy of solids". In: *Nature* 521.7553 (2015), pp. 498–502.

[123] A. Wirth, M. T. Hassan, I. Grguraš, J. Gagnon, A. Moulet, T. T. Luu, S. Pabst, R. Santra, Z. A. Alahmed, A. M. Azzeer, V. S. Yakovlev, V. Pervak, F. Krausz, and E. Goulielmakis. "Synthesized Light Transients". In: *Science* 334.6053 (2011), pp. 195–200.

[124] A. Saliminia, S. L. Chin, and R. Vallée. "Ultra-broad and coherent white light generation in silica glass by focused femtosecond pulses at 1.5 μm". In: *Opt. Express* 13.15 (July 2005), pp. 5731–5738.

[125] R. Huber, H. Satzger, W. Zinth, and J. Wachtveitl. "Noncollinear optical parametric amplifiers with output parameters improved by the application of a white light continuum generated in CaF2". In: *Optics communications* 194.4-6 (2001), pp. 443–448.

[126] M. Nisoli, S. De Silvestri, and O. Svelto. "Generation of high energy 10 fs pulses by a new pulse compression technique". In: *Applied Physics Letters* 68.20 (1996), pp. 2793–2795.

[127] M. Hassan. "Synthesis and control of attosecond light transients". PhD thesis. lmu, 2013.

[128] Y. Zhong, H. Diao, Z. Zeng, Y. Zheng, X. Ge, R. Li, and Z. Xu. "CEP-controlled supercontinuum generation during filamentation with mid-infrared laser pulse". In: *Optics express* 22.23 (2014), pp. 29170–29178.

[129] J. Darginavičius, D. Majus, V. Jukna, N. Garejev, G. Valiulis, A. Couairon, and A. Dubietis. "Ultrabroadband supercontinuum and third-harmonic generation in bulk solids with two optical-cycle carrier-envelope phase-stable pulses at 2 μm". In: *Optics express* 21.21 (2013), pp. 25210–25220.

[130] E. Goulielmakis, M. Schultze, M. Hofstetter, V. S. Yakovlev, J. Gagnon, M. Uiberacker, A. L. Aquila, E. Gullikson, D. T. Attwood, R. Kienberger, et al. "Single-cycle nonlinear optics". In: *Science* 320.5883 (2008), pp. 1614–1617.

[131] U. Morgner, R. Ell, G. Metzler, T. Schibli, F. Kärtner, J. Fujimoto, H. Haus, and E. Ippen. "Nonlinear optics with phase-controlled pulses in the sub-two-cycle regime". In: *Physical Review Letters* 86.24 (2001), p. 5462.

[132] A. Alismail, H. Wang, G. Barbiero, N. Altwaijry, S. A. Hussain, V. Pervak, W. Schweinberger, A. M. Azzeer, F. Krausz, and H. Fattahi. "Multi-octave, CEP-stable source for high-energy field synthesis". In: *Science advances* 6.7 (2020), eaax3408.

[133] M. T. Hassan, A. Wirth, I. Grguraš, A. Moulet, T. T. Luu, J. Gagnon, V. Pervak, and E. Goulielmakis. "Invited article: attosecond photonics: synthesis and control of light transients". In: *Review of scientific instruments* 83.11 (2012), p. 111301.

[134] G. Krauss, S. Lohss, T. Hanke, A. Sell, S. Eggert, R. Huber, and A. Leitenstorfer. "Synthesis of a single cycle of light with compact erbium-doped fibre technology". In: *Nature photonics* 4.1 (2010), pp. 33–36.

[135] Z. Zeng, Y. Zheng, Y. Cheng, R. Li, and Z. Xu. "Attosecond pulse generation driven by a synthesized laser field with two pulses of controlled related phase". In: *Journal of Physics B: Atomic, Molecular and Optical Physics* 45.7 (2012), p. 074004.

[136] O. Razskazovskaya, F. Krausz, and V. Pervak. "Multilayer coatings for femto-and attosecond technology". In: *Optica* 4.1 (2017), pp. 129–138.

[137] T. Amotchkina, M. K. Trubetskov, Y. Pervak, L. Veisz, and V. Pervak. "Stress compensation with antireflection coatings for ultrafast laser applications: from theory to practice". In: *Optics express* 22.24 (2014), pp. 30387–30393.

[138] M. T. Hassan, T. T. Luu, A. Moulet, O. Raskazovskaya, P. Zhokhov, M. Garg, N. Karpowicz, A. Zheltikov, V. Pervak, F. Krausz, et al. "Optical attosecond pulses and tracking the nonlinear response of bound electrons". In: *Nature* 530.7588 (2016), pp. 66–70.

[139] G. M. Rossi, R. E. Mainz, Y. Yang, F. Scheiba, M. A. Silva-Toledo, S.-H. Chia, P. D. Keathley, S. Fang, O. D. Mücke, C. Manzoni, et al. "Sub-cycle millijoule-level parametric waveform synthesizer for attosecond science". In: *Nature Photonics* 14.10 (2020), pp. 629–635.

[140] S. Fang, G. Cirmi, S.-H. Chia, O. D. Mücke, F. X. Kärtner, C. Manzoni, P. Farinello, and G. Cerullo. "Multi-mJ parametric synthesizer generating two-octave-wide optical waveforms". In: *Conference on Lasers and Electro-Optics/Pacific Rim*. Optical Society of America. 2013, WB3_1.

[141] Y.-C. Lin, Y. Nabekawa, and K. Midorikawa. "Optical parametric amplification of sub-cycle shortwave infrared pulses". In: *Nature communications* 11.1 (2020), pp. 1–14.

[142] B. Xue, Y. Tamaru, Y. Fu, H. Yuan, P. Lan, O. D. Mücke, A. Suda, K. Midorikawa, and E. J. Takahashi. "Fully stabilized multi-TW optical waveform synthesizer: Toward gigawatt isolated attosecond pulses". In: *Science Advances* 6.16 (2020), eaay2802.

[143] Q. Wu, T. Hewitt, and X.-C. Zhang. "Two-dimensional electro-optic imaging of THz beams". In: *Applied Physics Letters* 69.8 (1996), pp. 1026–1028.

[144] F. Blanchard, A. Doi, T. Tanaka, H. Hirori, H. Tanaka, Y. Kadoya, and K. Tanaka. "Real-time terahertz near-field microscope". In: *Optics express* 19.9 (2011), pp. 8277–8284.

[145] M. Mamaikin. "Time-Resolved Microscopy of Near-Infrared to Visible Waveforms". PhD thesis. München, Ludwig-Maximilians-Universität, 2020.

[146] D. A. Zimin. "PHz optoelectronics via attosecond control of optical properties in solids". PhD thesis. Ludwig Maximilian University of Munich, 2021.

[147] Y. Zhao, Y. Zhou, J. Liang, Z. Zeng, Q. Ke, Y. Liu, M. Li, and P. Lu. "Frustrated tunneling ionization in the elliptically polarized strong laser fields". In: *Optics express* 27.15 (2019), pp. 21689–21700.

[148] S.-W. Huang, G. Cirmi, J. Moses, K.-H. Hong, S. Bhardwaj, J. R. Birge, L.-J. Chen, I. V. Kabakova, E. Li, B. J. Eggleton, et al. "Optical waveform synthesizer and its application to high-harmonic generation". In: *Journal of Physics B: Atomic, Molecular and Optical Physics* 45.7 (2012), p. 074009.

[149] P. Siddons, C. S. Adams, and I. G. Hughes. "Optical control of Faraday rotation in hot Rb vapor". In: *Physical review A* 81.4 (2010), p. 043838.

[150] J. R. Schaibley, H. Yu, G. Clark, P. Rivera, J. S. Ross, K. L. Seyler, W. Yao, and X. Xu. "Valleytronics in 2D materials". In: *Nature Reviews Materials* 1.11 (2016), pp. 1–15.

[151] C. Heide, T. Boolakee, T. Higuchi, H. B. Weber, and P. Hommelhoff. "Interaction of carrier envelope phase-stable laser pulses with graphene: the transition from the weak-field to the strong-field regime". In: *New Journal of Physics* 21.4 (2019), p. 045003.

[152] R. P. Madden and K. Codling. "New autoionizing atomic energy levels in He, Ne, and Ar". In: *Physical Review Letters* 10.12 (1963), p. 516.

[153] J. M. Hollas. *Modern spectroscopy*. John Wiley & Sons, 2004.

Acknowledgements

I would like to gratefully acknowledge all the people who have contributed to this work.

I want to thank Prof. Ferenc Krausz who allowed me to work in his laboratories and for the fruitful scientific discussions.

Special thanks go to Nicholas Karpowicz. He has been a constant inspiration on both the scientific and human level. I want to say thank you as well to Matthiew Weidman for his support over my whole PhD studies and for guiding me in the lab since the very beginning. Without you all, this work would not have been possible.

My colleagues have been an essential part of my everyday life in and out of the laboratory. I am thankful for having worked in such a supportive, scientific and fun environment. I want to say thank you, in particular, to Mikhail Mamaikin for being a good friend and an irreplaceable colleague in these four years. A special thanks goes also to Najd for being a unique office and lab mate, Keyhan for sharing every day his home-made bread and for the deep long discussions scientific and not, Julia for fixing FP3 every time I broke it, Qasim for teaching me how to play table tennis, Dima for helping me to finish my PhD in one night and Amelie for translating the abstract of this dissertation.

I cannot thank enough my family for their unconditional support. Despite being far away I always felt at home every time I called you.

My deepest gratitude goes to Cristina Leonardo. Your love has been what kept me going even in the darkest moments. I could always rely on you for anything scientific and not. This work would not exist without you.